

**A Search for the Standard Model
Higgs Boson using the OPAL
Detector at LEP^{at}**

**Avayi Kwasi Ametewee
Department of Physics and Astronomy
University College London**

**A thesis submitted to the University of London in accordance with the
requirements for the degree of
Doctor of Philosophy.**

May 1995

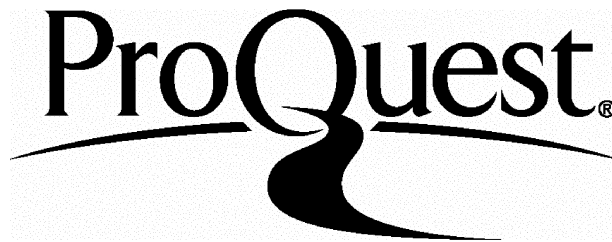
ProQuest Number: 10018540

All rights reserved

INFORMATION TO ALL USERS

The quality of this reproduction is dependent upon the quality of the copy submitted.

In the unlikely event that the author did not send a complete manuscript and there are missing pages, these will be noted. Also, if material had to be removed, a note will indicate the deletion.



ProQuest 10018540

Published by ProQuest LLC(2016). Copyright of the Dissertation is held by the Author.

All rights reserved.

This work is protected against unauthorized copying under Title 17, United States Code.
Microform Edition © ProQuest LLC.

ProQuest LLC
789 East Eisenhower Parkway
P.O. Box 1346
Ann Arbor, MI 48106-1346

ABSTRACT

In the Standard Model of fundamental particles, the existence of a doublet of boson fields is postulated in order for particle masses to be generated through spontaneous symmetry breaking. The Higgs boson (H^0) is the remnant of this doublet after spontaneous symmetry breaking has occurred.

A search for the Higgs boson has been performed with data from electron-positron collisions collected by the OPAL detector at LEP. The search was made for signals of the type $e^+ + e^- \rightarrow (e^+e^- \text{ or } \mu^+\mu^-) + H^0$, known as the leptonic channel; and $\nu\bar{\nu} + H^0$, known as the neutrino channel. This thesis reports on the results obtained, and describes the leptonic channel analyses in detail. The analyzed data was taken at the centre-of-mass energies between 88 and 95 GeV in the years 1990–1993 and represented a luminosity of 78pb^{-1} . When combined with previous OPAL results, the present study excludes the existence of a Standard Model Higgs boson with mass below 56.9 GeV at 95% confidence level. The results of this study were published in **Physics Letters B** in March 1994.

WRITER'S NOTE

Since joining the OPAL collaboration in December 1992, my first duty involved writing a small software package for the OPAL forward detector's drift chamber read-out system. This task was done under the close supervision of Dr. Bruce Kennedy (now of the Rutherford Appleton Laboratory, OXON.). This work forms the subject matter of **chapter three**.

Whilst at CERN, like most other OPAL members, I was sometimes assigned the duty of ensuring the smooth operation of the OPAL detector, and ensuring the safety of other on-duty personnel during data-taking periods.

My contribution to the advancement of scientific knowledge, was the utilisation of the results from data collected by the OPAL detector, to extend the Higgs lower mass limit from the previously quoted value of 52.6 GeV [26] to 56.9 GeV. The search for the Higgs boson through the leptonic channel— which forms the subject matter of **chapters five and six** – was undertaken by Dr. Peter Sherwood of the University College London, and myself. The search through the neutrino channel was undertaken by Professor Ehud Duchovni and Tomasz Wlodek of the Weizmann Institute of *Science* in Israel.

A.K. Ametewee,
London, May 1995.

My gratitudes

To Profs. David Miller and Michael Duff for being very inspirational leaders.

To Dr. David Tovee without whose guidance, I would never have gotten over the fear of computers.

To Dr. Bruce Kennedy who has helped immensely in some of the work presented in this thesis.

To Dr. Peter Sherwood for not only being my supervisor over the last fifteen months but also a great friend, without whose help this Ph.D thesis would not be possible.

To Profs. Duchovni, Mikenberg, and Igo-Kemenes; Tomasz Wlodek, Hans Bosch-Martin, Gustavo Wolf, Eilam Gross and Pedro Texiera-Dias for their constructive criticisms and suggestions.

To Robert Cranfield, Gordon Crone and Ian Vine for always helping to solve my computing problems.

To Brian Anderson, Derek Attree, Mike Creswell and Dominic Hayes who did not only get me out of my occasional pensive moods with their humour, but also helped on hardware matters.

To Dr. Peter Clark and Profs. Jones and Davies for being wonderful teachers during my first year as a research student.

To Gill West and Murna Dar for taking care of the paper-work for my trips to Switzerland and Norway.

To Dr. James Conboy for helping to store some of my postscript files.

To Andrew Charalambous for providing me with a very informative diagram of the OPAL detector.

To Mahmoud Al-Jaghoub, Gordon Barraclough, Philip Bignall, Paul Bright-Thomas, Corrina Catterall, Clive Lewis, Edward Mckignney, Antonis Papanetis, Anthony Rooke, Mark Sutton and Sabah 'Gory' Salih for being very good friends.

To Mary Shewry, Sue Cannon and Mette Stuwe for making my stay in Geneva a memorable one.

To all the new friends I made in Geneva, particularly James Clayton, Steve Clewer, Kate Dawe, Mindy 'Matthews', Stuart Clowes, Paul Philips, Roger Davies, Mark Pearce, Baljeet Nijjhar, Tara Shears and Robert Akers.

To Jason Ward and Warren Matthews for being such great friends who have done a lot to keep my sanity alive during my days at CERN.

To the 'Clan' – Francis, Selom, Kofi, Kafui, Freddy, Francesca, Francis Jnr. and Fidel for believing in me.

and finally,

To Daniel and Jennifer for all the good times we have had, and continue to have.

Dedicated to my parents,
Eric and Bernice.

Contents

1	THE STANDARD MODEL OF FUNDAMENTAL PARTICLES	23
1.1	An example of Spontaneous Symmetry Breaking	24
1.2	Generation of Mass Terms in the Standard Model	26
1.2.1	Generation of Masses for the Weak Bosons	26
1.2.2	Higgs Coupling to Bosons and Fermions	30
1.2.3	The Vacuum Expectation Value	31
1.3	Theoretical Bounds on the Higgs Mass	32
1.3.1	Upper Bounds	32
1.3.2	Lower Bounds	33
1.4	Higgs Production and Detection at LEP	34
1.5	Higgs Searches before LEP	36
1.6	Previous Higgs Searches at LEP	37
1.6.1	Searches for $M_H < 2M_\mu$ (~ 210 MeV)	37
1.6.2	Searches in Range $2M_\mu$ (~ 210 MeV) $< M_H < 2M_\tau$ (~ 3 GeV)	38
1.6.3	Searches in Range $2M_\tau$ (~ 3 GeV) $< M_H$	38
2	THE EXPERIMENTAL APPARATUS	41
2.1	The LEP Collider	41
2.1.1	The Particle Injection System	41

2.1.2	The Acceleration System	42
2.1.3	The General Layout of LEP	42
2.2	The OPAL Detector	42
2.2.1	The OPAL Coordinate System	44
2.2.2	The OPAL Magnet	44
2.2.3	Detectors of the Central Tracking System	46
2.2.4	The Time-of-Flight System	48
2.2.5	The Electromagnetic Calorimeter	48
2.2.6	The Hadron Calorimeter	49
2.2.7	The Muon Chamber	50
2.2.8	The Silicon-Tungsten Luminometer	51
2.2.9	The Forward Detector	51
2.3	The Trigger and Online System	51
2.3.1	The Event Trigger and its Logic	52
2.3.2	The Data Acquisition and Processing	54
2.4	The Slow Control System	54
3	LUMINOSITY MEASUREMENT WITH THE FORWARD DE- TECTOR	57
3.1	The OPAL Forward Detector	57
3.2	The Forward Detector Drift Chambers	57
3.3	Pulse Shape Analysis	64
4	Event Cross Section Calculation and Simulations	73
4.1	Cross Section of $e^+e^- \rightarrow H^0 f\bar{f}$	73
4.1.1	Lowest order cross section	74

<i>CONTENTS</i>	13
4.1.2 Higher Order Corrections	75
4.1.3 Corrections due to Bremsstrahlung	77
4.2 The Final Bjorken Cross Sections (Leptonic Channel)	79
4.3 Higgs Boson Decay Branching Ratios	79
4.3.1 QCD Corrections	81
4.4 Simulation of Higgs Events	84
4.4.1 The Generation Process	84
4.5 Simulation of Four Fermion Events	86
4.6 GOPAL – The OPAL Simulation Program	86
5 THE SEARCH ALGORITHM	89
5.1 The Event Trigger	89
5.2 The Event Filter	90
5.3 The Main Selection	93
5.3.1 Lepton Pair Identification	93
5.3.2 Common Cuts	95
5.3.3 Lepton Pair Isolation Cuts	98
5.4 Event Selection Efficiencies	106
5.5 The Lepton Identification Efficiencies and Systematic Errors	109
5.5.1 Selection of Lepton Tracks for the Study	110
5.5.2 The Lepton Identification Efficiencies	111
5.5.3 Determination of the Correction Factors (and Systematic Errors) and their Momentum Dependence	111
5.6 The Neutrino Channel Search	112
6 THE RESULTS OF THE SEARCH	121

6.1	The Leptonic Channel Search	121
6.1.1	Data Consistency Checks	121
6.1.2	The Leptonic Channel Results	126
6.1.3	The Surviving Event	126
6.1.4	Leptonic Channel Background and Total Systematic Error Estimation	130
6.2	Results For the Neutrino Channel	132
6.2.1	Neutrino Channel Background and Total Systematic Error Estimation	132
6.3	The Higgs Mass Limit	133
6.4	Conclusions and Outlook	134

List of Figures

1.1	$V(\Phi)$ vs $ \Phi $ for the cases when μ^2 is positive or zero, and negative.	27
1.2	The electron Yukawa interaction.	29
1.3	(1) Muon decay as described by the Fermi theory. (2) Muon decay as described by the Electroweak theory.	31
1.4	The possible contributions to W^+W^- scattering.	33
1.5	Lower bounds on Higgs mass as a function of M_t obtained by E. Gross et al.	35
1.6	Lower bound curves for different cut-off scales Λ obtained by Lindner, Sher and Zaglauer. The solid line is for $\Lambda = 10^{15}$ GeV.	35
1.7	(1) The $Z^0 \rightarrow H^0 \gamma$ process. (2) The Bjorken process.	36
2.1	A schematic representation of the LEP electron and positron production and injection system.	43
2.2	A labelled diagram of the OPAL detector.	45
2.3	An overview of the trigger generation by the θ - ϕ matrix. The track trigger (TT), the time-of-flight system (TOF), the electromagnetic calorimeter (EM), the hadron calorimeter (HA) and the muon detector (MU) send signals to the θ - ϕ matrix, the outputs of which are logically combined to form the final trigger decision. Crosses on the vertical line representing different particle types passing through the detector indicate the sensitivity at the trigger level.	53
2.4	The overall scheme of event triggering, readout, monitoring and data handling.	55

- 3.1 A labelled cross section of a quadrant of the forward detector in its 1993 configuration (turn page on its long side for better viewing). . . 58
- 3.2 A head-on view of one half of the forward detector showing only its coordinate system used for survey measurements and the four quadrants of drift chambers. The SARCs shown in the solid lines are mounted in front of the TC2s (dashed lines). 60
- 3.3 A cross section of a Large Angle Drift Chamber (TC2) showing its sense (field) wires as the small (large) black circles. The field-shaping copper strips are shown as the rectangles on the faces of the chamber partitions. 60
- 3.4 Pad amplifier circuit. The return side of the wire preamplifier circuit is grounded. 61
- 3.5 Sense wire and field wire circuit. The connections for the wire S2 are similar to those for S1. 62
- 3.6 A description of the digitization of a signal using comparators. . . . 63
- 3.7 The non-linear response function produced by the resistor **R2**. . . . 64
- 3.8 A snapshot of a typical pulse and its differentiated pulse after correction for the non-linear response. 65
- 3.9 A typical 3-line plot. The three distinct regions **1**, **2**, **3** correspond to tracks below the wires, between the wires, and above the wires respectively. 68
- 3.10 A 3-line plot with periodic clumps. 68
- 3.11 The effects of the spikes and dropouts on the drift time calculation. The arrow points to the real drift time whilst the diamond points to the drift times with the spikes or dropouts present. On each row are the pulse and its differentiated pulse. Starting from the top row, (a) The missing of the pulse by the 'Difference of Samples' algorithm caused by a spike on the rising edge. (b) The under-estimation of the drift time by a spike appearing on the pedestal. (c) The missing of a pulse caused by a dropout. (d) The over-estimation of the drift time by a spike appearing on the peak sample. 70

- 3.12 The top figure illustrates the simulation of pulses with spikes by moving the pulse from left to right along the drift time axis. The arrows indicate some positions (at multiples of 320 ns) where spikes will be superimposed on the rising edge of the pulses. The bottom histogram is the resulting drift time distribution. The peaking at 320 ns time intervals is evident. 71
- 3.13 A comparison between the drift time distributions for un-rectified (top histogram) and rectified (bottom histogram) pulses. 72
- 4.1 The Feynman diagram for the lowest order Bjorken process. 74
- 4.2 The higher order Bjorken processes evaluated in the IBA scheme. Figure (1) is the one loop Z^0 propagator self energy process. Figure (2) is the Z vertex process; the dominant contribution to this process is that due to $f = \text{top quark}$ 76
- 4.3 QED contributions to the Bjorken process. The intermediate Z boson and the final state particles are not labelled. The wavy lines are the photons. Figures (1), (2) and (3) are the virtual photon processes, (4) and (5) are the soft and hard photon radiation processes. 78
- 4.4 The Bjorken cross section (leptonic channel) vrs the centre of mass energy for Higgs of mass 50, 60 and 70 GeV. 80
- 4.5 The Bjorken cross section (leptonic channel) at center of mass energy of 91 GeV, \sqrt{s} the Higgs mass. 81
- 4.6 The Z^* mass ($M(l^+l^-)$) distribution for a selection of M_H values. . . 82
- 4.7 The average momentum of Z^* , for a range of Higgs masses. 83
- 4.8 Four fermion final states. Only the final state four-vectors and the Z propagators are labelled. The wavy lines denote photon propagators. Figure (1) is the annihilation process, (2) (3) (4) and (5) are the conversion processes, (6) and (7) are the bremsstrahlung processes and (8) is the multi-peripheral process. 87
- 4.9 A plot of Bjorken cross section (leptonic channel) – solid curve – and the four-fermion cross section – dotted curve – versus the hadronic mass at center of mass energy 91 GeV. A logarithmic scale is used for the cross section axis. The four fermion cross sections are for events of the type $l^+l^-q\bar{q}$ where l denotes electrons and muons. 88

- 5.1 A flow chart of the search for the Bjorken signal through the leptonic channel, indicating in the boxes, the types of events remaining after successive group of cuts have been applied. 91
- 5.2 A labelled reconstruction of an expected Higgs signal of mass 52 GeV in the leptonic channel. 92
- 5.3 dE/dx curves for muons, charged pions, charged kaons, protons, and electrons in the OPAL jet chamber. 94
- 5.4 A comparison between the lepton momentum and momentum sum spectra for some Higgs events. The entries in the histograms, correspond to a luminosity of 12500 (40000) pb^{-1} for the 52 (62) GeV Higgs signal. 96
- 5.5 A comparison between the lepton pair opening angles for some Higgs events. The entries in the histograms, correspond to a luminosity of 12500 (40000) pb^{-1} for the 52 (62) GeV Higgs signal. 97
- 5.6 Schematic diagram showing a special case of the Bjorken process where the angle between the direction of the H^0 decay products and the H^0 flight direction is almost 90° . The diagram illustrates the reasons for the P3030, E3030 and the P4515, E4515 isolation cuts (see section on lepton isolation cuts). 99
- 5.7 A comparison the isolation ratios for lepton tracks from samples of simulated multihadronic and Higgs ($M_H = 60$ GeV) events are shown. The number of Higgs (Multi-hadron) events analysed for these plots, corresponds to a luminosity of 12500 (78) pb^{-1} . The region of acceptance is indicated in the bottom left-hand corner of the plots. 100
- 5.8 An illustration of the GCE algorithm. C^n is the calorimetric energy deposited by a charged pion as a function of its momentum. Note that $E > E^1 + E^2 + \dots$ since hadrons do not usually deposit all their energy in the electromagnetic calorimeter. Note also that by ignoring all clusters having associated tracks, we would be losing information about neutral particles such as the overlapping photon. 102
- 5.9 A comparison of the GCE mass distributions for samples of simulated and real hadronic Z^0 decay events. 103
- 5.10 A comparison between the estimated hadronic masses and the true Higgs mass, for the electron and muon channels. 104
- 5.11 The GCE and recoil mass resolutions, and scale factors for the electron and muon channels. 105

- 5.12 The hadronic mass \sqrt{s} the lepton pair mass for four-fermion events (black circles) and a 52 GeV Higgs signal (open circles). The number of Higgs events and four-fermion events have been normalised to the same luminosity (78 pb^{-1}). 107
- 5.13 These plots show the efficiencies and efficiency differences in the five detector regions for beam energy electrons. The error bars are present but are too small to be visible. 'A'('B') denotes the end cap (overlap) regions, 'C' denotes the barrel region. 114
- 5.14 These plots show the efficiencies and efficiency differences in the five detector regions for beam energy muons. The error bars are present but are too small to be visible. 'A'('B') denotes the end cap (overlap) regions, 'C' denotes the barrel region. 115
- 5.15 These plots show the electron efficiencies and efficiency differences in the five detector regions for the three momentum bins. The non-existent error bars for the lower momentum electrons are due to 100% efficiencies. 116
- 5.16 These plots show the muon efficiencies and efficiency differences in the five detector regions for the three momentum bins. The non-existent error bars for the lower momentum muons are due to 100% efficiencies. 117
- 5.17 Plots of the correction factors (in %) for the three momentum bins. The factors are plotted at the momentum points corresponding to the mean of the momenta of the tracks used in the study, in the momentum bins. The horizontal error bars are a measure of the spread of momenta about these means. For the electron (muon) channel, an exponential (linear) fit was found to be the most suitable fit. 118
- 5.18 A computer reconstruction of a simulated Higgs signal in the neutrino channel. 120
- 6.1 Comparisons between the 1992 (stars) and the 1993 (histogram) distributions for the electron-candidate track and cluster parameters on which cuts were applied. The number of entries in the distributions have been normalised to one. 122
- 6.2 Comparisons between the 1992 (stars) and the 1993 (histogram) distributions for the electron and muon-candidate track parameters on which cuts were applied. The number of entries in the distributions have been normalised to one. 123

- 6.3 Comparisons between the 1992 (stars) and the 1993 (histogram) distributions for the muon-candidate track and event parameters on which cuts were applied. The number of entries in the distributions have been normalised to one. 124
- 6.4 Comparisons between the 1992 (stars) and the 1993 (histogram) distributions for the isolation ratios for the muon and electron candidates. The number of entries in the distributions have been normalised to one. 125
- 6.5 The isolation ratios for the lepton candidates in the 1992 and 1993 data. 128
- 6.6 The lepton pair mass **VS** the GCE mass for the events, from the 1992 and 1993 data, passing all cuts except the mass cuts. 129
- 6.7 The event passing all the muon channel cuts (event 15048, run 4353). 131
- 6.8 The new OPAL lower limit (arrow) on the Higgs mass of 56.9 GeV. . 134

List of Tables

1.1	Some properties of the fermions and bosons in the Standard Model (antiparticle partners not shown).	25
1.2	An analogy between the superconductor and the universe.	26
1.3	Production rates of the different decay channels of the Bjorken process.	39
4.1	Decay branching ratios (in %) of the Higgs to fermions.	84
5.1	Number of simulated Higgs events remaining after successive cuts in the muon channel.	106
5.2	Number of simulated Higgs events remaining after successive cuts in the electron channel.	108
5.3	Number of Monte Carlo $Z^0 \rightarrow \bar{q}q$ events remaining after successive cuts in the electron and muon channels. The number of processed events corresponds to a luminosity equal to that of the OPAL data (78 pb^{-1}).	108
5.4	Number of four-fermion events remaining after successive cuts in the electron and muon channels. The numbers in the ‘ Mass Cuts ’ column, are the number of events with hadronic mass greater than 50 GeV. The entries in the last column have been scaled to the luminosity of the OPAL data (78 pb^{-1}).	109
5.5	Number of electron and muon tracks chosen from the real and simulated (MC) data.	111
5.6	The MC efficiency minus the data efficiencies and their corresponding errors, in parentheses, are expressed in % for each of the detector regions for the three momentum ranges.	113

- 5.7 The number of hadron tracks (from taus) studied, and the number identified as electrons and muons in parentheses. 113
- 5.8 Summary of the correction factor F and systematic error on F (in parentheses), are expressed in % for the three momentum ranges. . . 113
- 6.1 Number of events after successive cuts in the muon channel for the data, for simulated hadronic Z^0 decay events, and for simulated Higgs ($M_H = 60$ GeV) events. The number of events have been scaled so that the real and simulated data samples have a luminosity of 78 pb^{-1} . The numbers between parentheses give efficiencies. 126
- 6.2 Number of events after successive cuts in the electron channel for the data, for simulated hadronic Z^0 decay events, and for simulated Higgs ($M_H = 60$ GeV) events. The number of events have been scaled so that the real and simulated data samples have a luminosity of 78 pb^{-1} . The numbers between parentheses give efficiencies. 127
- 6.3 Properties of the event that passed all the cuts. Momenta, masses and energies are expressed in GeV, angles in degrees, and distances in millimeters. 130
- 6.4 Number of events after successive cuts in the neutrino channel for the 1990 to 1993 data, for simulated Z^0 decay events, and for simulated Higgs ($M_H = 60$ GeV) events. The number of events have been scaled so that the luminosities of the real and simulated data samples are the same. The numbers between parentheses give efficiencies. 132
- 6.5 Efficiencies and expected events in the neutrino and charged lepton channels. The number of events have been reduced by one standard deviation of the systematic error. 133

Chapter 1

THE STANDARD MODEL OF FUNDAMENTAL PARTICLES

The family of fundamental particles is believed to consist of fermions and bosons. The theories that describe the interactions of the presently identified fundamental particles are collectively called the The Standard Model¹. In brief, the present picture is as follows:

- The interactions between particles are mediated by three types of bosons – the photon (γ) which transmits the electromagnetic force, the weak bosons (W^+ , W^- , Z^0) which transmit the weak force, and the gluons (g_i , $i=1\dots 8$) which transmit the strong force.
- There are two types of fermions – leptons and quarks.
- Charged leptons interact both electromagnetically and weakly whilst neutral leptons (neutrinos) interact only weakly.
- There are three generations of leptons - electron and the electron neutrino, muon and the muon neutrino, tau and the tau neutrino.
- There are three generations of quarks - the up and down, charm and strange, beauty and top quarks. Each quark exists in one of three possible colour states.
- All quarks are charged and interact electromagnetically, weakly and strongly.
- The weak and electromagnetic interactions of both quarks and leptons are described in a partially unified way by the Electroweak theory, whilst the strong interaction of quarks is described by Quantum Chromodynamics.

¹The gravitational interaction which is described by General Relativity, is not included in the Standard Model because General Relativity does not belong to the same class of theories as those of the Standard Model. See [1] for a comprehensive discussion of gravitational interactions.

- Every fermion and boson has an antiparticle partner having opposite charge.
- Matter consists of 12 leptons and 12 quarks (Table 1.1).

The theories of the Standard Model belong to a special class of theories called the Yang-Mills theories. In these theories, the Lagrangian is invariant with respect to local gauge symmetry transformations. It has been shown by t'Hooft [3] that Lagrangians of Yang-Mills theories are renormalizable, *i.e.* they make finite predictions of interaction probabilities and rates at all orders of perturbation theory. An important aspect of the Standard Model is the $SU_L(2) \times U_Y(1) \times SU_C(3)$ symmetry [4] that its Lagrangian obeys. Were this symmetry obeyed exactly in nature, all the particles listed in Table 1.1 would be massless, resulting in infinite ranges for all interactions. However, experimental evidence shows that not all particles are massless; the weak bosons are known to be massive since the weak interactions are of a very short range.

For the Standard Model ~~still to~~ describe the interactions of the particles observed in nature, the symmetry will have to be broken in a subtle way thus *accommodating* the particles' masses, as well as still preserving the Model's renormalizability. The subtle breaking of the symmetry is done spontaneously, this involves finding suitable Lagrangians in which the symmetry is broken only in the ground state. The Standard Model introduces a doublet of fields, the Higgs doublet, into the family of known particle fields to achieve this purpose. It is thought that these fields permeate the whole of the universe. After spontaneous symmetry breaking has occurred in the ground state, only one of the fields has a non-vanishing value. Particle masses are generated by their interactions with this residual Higgs field. A quantum of this residual field is called the Higgs boson.

1.1 An example of Spontaneous Symmetry Breaking

An example of the generation of a boson's mass by spontaneous symmetry breaking can be found in solid state physics [5]. The Meissner-Ochsenfeld effect, which is the attenuation of an applied magnetic field in a superconductor when its temperature T is lowered below a certain critical value T_c , is explained as the generation of an effective mass for the photons in the magnetic field.

This interpretation is made because the range of the magnetic field is exponentially attenuated in the superconductor with attenuation length λ . By the Heisenberg uncertainty principle, $\Delta x \Delta M \geq \hbar/c$ where $\Delta x = \lambda$ and ΔM is the *effective mass of a photon*.

The reason for the attenuation is that in the surface layer of the superconductor of thickness λ , currents are set up which produce an internal magnetic field which cancels the external one. These currents are initiated by electrons which spontaneously bind together to form pairs when the temperature falls below T_c ; the pairs then settle down into a highly correlated ground state, which is a non-zero electron-pair field extending over the whole of the superconductor. Carrying

[56]

Table 1.1: Some properties of the fermions and bosons in the Standard Model (antiparticle partners not shown).

Fermions	Charge (electron charge)	Mass (GeV)
electron, e	-1	0.0005
electron neutrino, ν_e	0	$< 4.5 \times 10^{-9}$
muon, μ	-1	0.1056
muon neutrino, ν_μ	0	$< 1.6 \times 10^{-4}$
tau, τ	-1	1.7841
tau neutrino, ν_τ	0	$< 2.9 \times 10^{-2}$
up quark, u	2/3	0.002 - 0.008
down quark, d	-1/3	0.005 - 0.015
charm quark, c	2/3	1.3 - 1.7
strange quark, s	-1/3	0.100 - 0.300
top quark, t	2/3	> 170
bottom quark, b	-1/3	4.7 - 5.3
Bosons	Charge (electron charge)	Mass (GeV)
Photon, γ	$\ll 2 \times 10^{-32}$	$\ll 3 \times 10^{-33}$
W^+	+1	80.22 ± 0.26
W^-	-1	80.22 ± 0.26
Z^0	0	91.17 ± 0.02
Gluons	0	0
Higgs	0	?

over the superconductor analogy to the weak interactions (Table 1.2), this ensemble of electron pairs corresponds to the Higgs field introduced into the Standard Model.

The average vacuum value of the Higgs field v , can be determined from experiment (Section 1.2.3). This average value is a fundamental parameter of the Electroweak theory since it sets the scale of mass for all particles whose masses are generated by the Higgs mechanism.

Table 1.2: An analogy between the superconductor and the universe.

The Superconductor	The Universe
Ground state of the superconductor	The vacuum
The electron-pair field	The Higgs field
Screening mechanism which provides effective mass for the photon	The Higgs mechanism provides masses for the weak bosons
Electromagnetic gauge symmetry is preserved since Maxwell's equations are still obeyed	Weak gauge symmetry is preserved

1.2 Generation of Mass Terms in the Standard Model

The introduction of mass terms into the Standard Model Lagrangian was due to Higgs P. [6]. In his formalism, the existence of a complex doublet $\Phi(x)$ of four scalar (spin = 0) fields with isospin $I = 1/2$ and hypercharge, $Y = 1$ is postulated.

1.2.1 Generation of Masses for the Weak Bosons

The four massless, basic electroweak gauge boson fields – W_μ^i ($i=1\dots 3$) and B_μ^o – are thought to interact with the fields of the doublet. In the process, three of the four Higgs fields become the third degrees of freedom of three of the gauge bosons. The Lagrangian associated with these interactions, which can be shown to obey the $SU_C(3) \times SU_L(2) \times U_Y(1)$ symmetry is given by [4]

$$L_\Phi = (D_\mu \Phi^\dagger)(D^\mu \Phi) - V(\Phi) \quad (1.1)$$

where $V(\Phi)$ is the potential energy of vacuum and

$$D_\mu = \partial_\mu - ig\vec{J} \cdot \vec{W}_\mu - ikB_\mu, \quad (1.2)$$

$$V(\Phi) = \mu^2 \Phi^\dagger \Phi + \lambda (\Phi^\dagger \Phi)^2 \quad (1.3)$$

$$\Phi = \begin{pmatrix} \phi^+ \\ \phi^0 \end{pmatrix} = \frac{1}{\sqrt{2}} \begin{pmatrix} \phi_1 + i\phi_2 \\ \phi_3 + i\phi_4 \end{pmatrix}. \quad (1.4)$$

μ^2 and λ are real and positive constants respectively. g and k are the coupling constants of the $SU_L(2)$ and $U_Y(1)$ symmetry groups respectively. \vec{J} represents a vector with the three Pauli spin matrices as its components and \vec{W}_μ represents

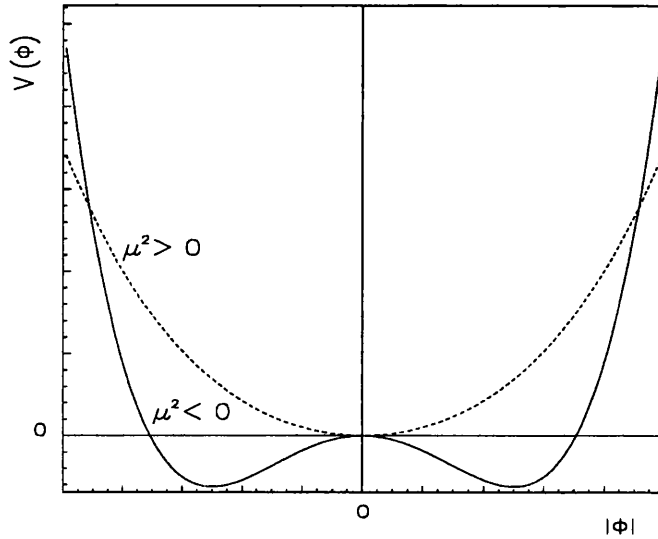


Figure 1.1: $V(\Phi)$ vs $|\Phi|$ for the cases when μ^2 is positive or zero, and negative.

a vector with W_μ^i ($i=1\dots 3$) as its components. Figure 1.1 shows the two possible structures of the potential energy $V(\Phi)$. In order to determine how spontaneous symmetry breaking may be brought about, we note that in the case where $\mu^2 \geq 0$, symmetry breaking is not possible because the ground state has a value of zero and so is unique. We are therefore only interested in the case where $\mu^2 < 0$. The potential $V(\Phi)$ then has its minimum value at any finite value of Φ where

$$\Phi^\dagger \Phi = \phi_1^2 + \phi_2^2 + \phi_3^2 + \phi_4^2 = -\frac{\mu^2}{2\lambda} = v^2. \quad (1.5)$$

If we choose

$$\phi_1 = \phi_2 = \phi_4 = 0, \quad (1.6)$$

then the constant vacuum field value is given by

$$\Phi_0 = \frac{1}{\sqrt{2}} \begin{pmatrix} 0 \\ v \end{pmatrix}. \quad (1.7)$$

The constant v , is the vacuum expectation value. This ground state has hypercharge $Y = 1$, third component of isospin $I_3 = -1/2$ and electric charge $Q = 0$. We made this choice of out of the large number of ground states available to us because this particular one is left invariant by $U_{em}(1)$ gauge transformations [4], with the result that the gauge boson A_μ (photon) associated with that symmetry group remains massless.

Since in field theory, particles are considered to be quantum fluctuations about a ground state *i.e.* *Physical particle = Ground state + A small fluctuation θ* , the

resulting doublet which represents the physical Higgs fields, can be parametrized in terms of four real fields $\theta_1, \theta_2, \theta_3$ and $H(x)$ using Equation 1.8. $\theta_1, \theta_2, \theta_3$ are small. [4]

$$\Phi_H(x) = \frac{1}{\sqrt{2}} \begin{pmatrix} \theta_1 + i\theta_2 \\ v + H(x) - i\theta_3 \end{pmatrix} \simeq \frac{1}{\sqrt{2}} \exp(i\vec{J}\cdot\vec{\theta}(x)/v) \begin{pmatrix} 0 \\ v + H(x) \end{pmatrix}. \quad (1.8)$$

Because massive particles have two orthogonal degrees of freedom, it is necessary to use the $SU(2)$ invariance of $\Phi_H(x)$ to gauge away the three $\theta(x)$ fields so that they become the longitudinal degrees of freedom of the would-be massive gauge bosons. This gauging which is termed the Higgs mechanism, is done by multiplying $\Phi_H(x)$ with the operator $\exp(-i\vec{J}\cdot\vec{\theta}(x)/v)$ to become

$$\Phi_H(x) = \frac{1}{\sqrt{2}} \begin{pmatrix} 0 \\ v + H(x) \end{pmatrix}. \quad (1.9)$$

A quantum of the $H(x)$ field is the Standard Model Higgs boson, normally denoted by H^0 .

Now, let us examine the Higgs Lagrangian, Equation (1.1), very closely and concentrate only on the kinetic and interaction energy terms. As a first step, we note that

$$D_\mu \begin{pmatrix} 0 \\ v + H(x) \end{pmatrix} = -i(v + H(x)) \begin{pmatrix} g(W_\mu^1 - iW_\mu^2) \\ gW_\mu^3 - kB_\mu \end{pmatrix}, \quad (1.10)$$

therefore,

$$\begin{aligned} D_\mu \Phi_H^\dagger D^\mu \Phi_H &= \frac{1}{4}(v + H(x))^2 (g^2 W^+ W^- + (gW_\mu^3 - kB_\mu)^2) \\ &= \frac{1}{4}(v + H(x))^2 (g^2 W^+ W^- + (g^2 + k^2) Z_\mu Z^\mu) \end{aligned} \quad (1.11)$$

since by definition

$$W_\mu^+ = \frac{W_\mu^1 - iW_\mu^2}{\sqrt{2}}, \quad (1.12)$$

$$W_\mu^- = \frac{W_\mu^1 + iW_\mu^2}{\sqrt{2}}, \quad (1.13)$$

$$Z_\mu = \frac{g}{\sqrt{2(g^2 + k^2)}} (gW_\mu^3 - kB_\mu). \quad (1.14)$$

In order to find the boson mass terms, we examine only the boson self interactions terms, *i.e.* the terms $KZ_\mu Z^\mu$ and $KW_\mu W^\mu$ where K is a coefficient in Equation (1.11). The coefficients of these terms are the masses squared of the bosons. The masses of the W and Z gauge bosons are found to be given by

$$M_W^2 = \frac{g^2 v^2}{4}, \quad (1.15)$$

$$M_Z^2 = \frac{1}{4}(g^2 + k^2)v^2. \quad (1.16)$$

Defining $\tan\theta_w = k/g$, we find that $\cos\theta_w = M_W/M_Z$. θ_w is another parameter of the Electroweak theory called the weak mixing angle.

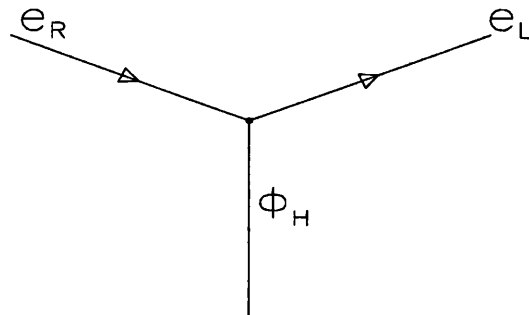


Figure 1.2: The electron Yukawa interaction.

Generation of Masses for Fermions and the Higgs

The appealing feature of the Higgs sector of the Standard Model is that the same Higgs doublet (Φ_H) used in the generation of the boson masses, is sufficient in generating masses for the leptons and quarks. The Higgs doublet does this by coupling the right-handed lepton/quark states to their left-handed states. These couplings are known as the Yukawa couplings by analogy with the original theory of nuclear forces carried by the Yukawa pion.

Consider as an example, the generation of the electron mass by its Yukawa coupling as shown in Figure 1.2. Since the relation between the third component of isospin I_3 , ^{weak} hypercharge Y and the electric charge Q is given by $Q = I_3 + Y/2$, the values of Y and I for the left-handed electron state (e_L) are given by -1 and $-1/2$ respectively. For the right-handed state (e_R), the respective values are -2 and 0 . The Higgs doublet with $Y = 1$ and $I_3 = -1/2$ has the required quantum numbers needed to couple e_R to e_L . The electron Yukawa Lagrangian L_e is given by

$$L_e = \frac{-G_e}{\sqrt{2}} (\bar{\Phi}_e \Phi_H e_R + \bar{e}_R \Phi_H^+ \Phi_e) = \frac{G_e}{\sqrt{2}} (v \bar{e} e - H \bar{e} e) \quad (1.17)$$

where

$$\Phi_e = \frac{1}{\sqrt{2}} \begin{pmatrix} \nu_{eL} \\ e_L \end{pmatrix}, \quad e = e_L + e_R \quad (1.18)$$

and G_e is the electron Yukawa coupling constant. The electron mass term is the

coefficient of the electron self interaction term and it is given by

$$M_e = \frac{G_e v}{\sqrt{2}}. \quad (1.19)$$

The Yukawa coupling constants are free parameters since they have to be chosen such that the experimentally measured fermion masses are recovered from fermion mass expressions of the type Equation (1.19). Note that the absence of a neutrino mass term in L_e , implies that the electron neutrino is massless.

The quark masses are generated in almost the same way. The difference here is that to generate a mass for the upper member of a quark doublet, we must use the $SU(2)$ gauge invariance to construct a new Higgs doublet from Φ_H . Consider as an example, the generation of masses for the up (u) and down (d) quark doublet; the gauge invariant Yukawa Lagrangian is given by

$$\begin{aligned} L_{ud} &= \frac{-1}{\sqrt{2}}(G_d \bar{\Phi}_{ud} \Phi_H d_R + G_u \bar{\Phi}_{ud} \Phi_{nH} u_R + G_d \bar{\Phi}_{ud} \Phi_H d_R + G_u \bar{\Phi}_{ud} \Phi_{nH} u_R) \\ &= \frac{G_d}{\sqrt{2}}(v \bar{d}d - H \bar{d}d) - \frac{G_u}{\sqrt{2}}(v \bar{u}u + H \bar{u}u) \end{aligned} \quad (1.20)$$

where

$$\Phi_{ud} = \frac{1}{\sqrt{2}} \begin{pmatrix} u_L \\ d_L \end{pmatrix} \quad (1.21)$$

and

$$\Phi_{nH} = -i\tau_2 \Phi_H^* = \frac{1}{\sqrt{2}} \begin{pmatrix} v + H(x) \\ 0 \end{pmatrix} \quad (1.22)$$

whilst G_u and G_d are the up and down quark Yukawa coupling constants respectively. The up and down quark mass terms as obtained from Equation (1.20) are given respectively by

$$M_u = \frac{G_u v}{\sqrt{2}}, \quad M_d = \frac{G_d v}{\sqrt{2}}. \quad (1.23)$$

The coefficient of the Higgs self interaction term in Equation (1.1) is the Higgs mass squared and is given by

$$M_H^2 = 2\lambda v^2. \quad (1.24)$$

Note that this mass is not predicted by the Standard Model since λ is a free parameter.

1.2.2 Higgs Coupling to Bosons and Fermions

To find the coupling constants of the Higgs to W^- , W^+ , Z^0 and to fermions, we refer again to Equation (1.11) and the appropriate Yukawa Lagrangians and read out

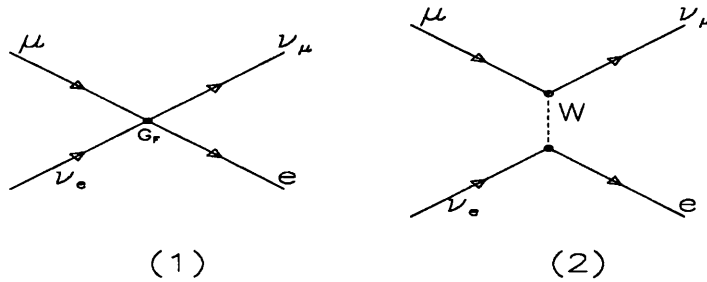


Figure 1.3: (1) Muon decay as described by the Fermi theory. (2) Muon decay as described by the Electroweak theory.

the coefficients of the terms HWW , HZZ and of the type $H\bar{f}f$ respectively. The coupling constants are given by

$$G_{HZZ} = \frac{gM_Z}{\cos\theta_w} = \frac{gM_Z^2}{M_W}, \quad (1.25)$$

$$G_{HWW} = gM_W, \quad (1.26)$$

$$G_{H\bar{f}f} = \frac{G_f}{\sqrt{2}} = \frac{M_f}{v}. \quad (1.27)$$

i.e. the couplings are proportional to the masses of the particles.

1.2.3 The Vacuum Expectation Value

The matrix element (whose square is the interaction probability) of a charged current interaction such as muon decay (Figure 1.3) is predicted by the Fermi theory² to be given by [57]

$$M_{Fermi} = \left(\frac{4G_F}{\sqrt{2}} \right) J^\mu J_\mu^\dagger. \quad (1.28)$$

²An early theory of weak interactions which considers them as point interactions and not mediated by gauge bosons. The point interaction is assigned a coupling constant of G_F . This theory was originally used to describe nuclear beta decay.

The Electroweak theory predicts the matrix element to be [57]

$$M \simeq \left(\frac{g^2}{2M_W^2} \right) J^\mu J_\mu^+ \quad (1.29)$$

where the $1/M_W^2$ term is the W boson propagator, $J^\mu = \bar{\nu}_\mu \gamma_\mu \mu$ and $J_\mu^+ = \bar{e} \gamma_\mu \nu_e$. Since in the low energy limits, the Fermi theory must be recovered from the Electroweak theory, we have $M_{Fermi} = M$, so that

$$\frac{4G_F}{\sqrt{2}} = \frac{g^2}{2M_W^2}. \quad (1.30)$$

Using the expression for the mass of the W boson in terms of v , Equation (1.15), and the experimentally measured value of G_F ($\sim 1.16 \times 10^{-5} \text{ GeV}^{-2}$), one finds that the vacuum expectation value is given by

$$v = 2^{-1/4} G_F^{-1/2} = 246 \text{ GeV}. \quad (1.31)$$

1.3 Theoretical Bounds on the Higgs Mass

1.3.1 Upper Bounds

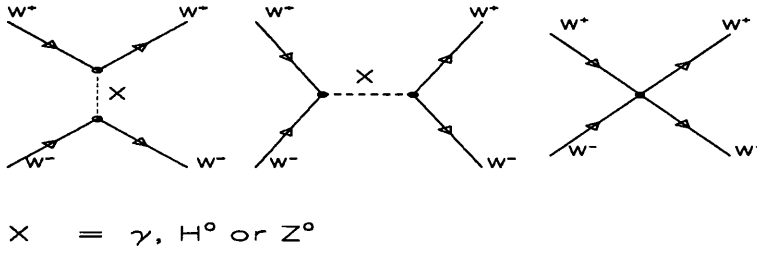
Renormalizability and Unitarity Bounds

Upper bounds on the Higgs mass generally result from renormalizability and unitarity arguments. In the former argument, one finds the mass at which the Higgs is so heavy that it ceases to couple to other particles due to its propagator term $1/M_H^2$ becoming too small, thus rendering the theory unrenormalizable. Veltman and Van der Bij [7] have established an upper limit of 3 TeV using this argument.

The unitarity arguments are based on the requirement that various processes should have finite rates. Lee, Quigg and Thacker [8] have considered the scattering of W bosons. The possible contributions to this process are shown in Figure 1.4. They imposed the condition that the scattering rate does not exceed the collision rate – the unitarity condition – and found an upper limit of 1.2 TeV on the Higgs mass.

Triviality Bounds

Triviality arguments result from the fact that the Higgs boson self-coupling constant λ increases with the energy scale Q . The dependence of λ on Q can be expressed

Figure 1.4: The possible contributions to W^+W^- scattering.

as [9]

$$\lambda(Q) = \frac{\lambda(v)}{1 - b\lambda(v) \log(Q^2/v)} \quad (1.32)$$

where $b = 3/4\pi^2$ and v is the vacuum expectation value.

If $\lambda(Q)$ is required to be finite at all values of Q , then $\lambda(v) = 0$. The Electroweak theory is then said to be trivial (non-interacting) – clearly not what we want it to be. We may put an upper bound on M_H by requiring that the theory remains interacting and perturbative (*i.e.* $0 < \lambda(Q) \leq 1$), up to some scale $Q = \Lambda$. If the Planck scale (10^{19} GeV) is chosen, we find that $M_H \leq 140$ GeV. In other words, if the Higgs sector is to be a good theory up to $Q \sim 10^{19}$ GeV, then M_H must be less than 140 GeV. Bounds obtained by the triviality arguments are not true bounds but depend on the cut-off scale Λ chosen.

1.3.2 Lower Bounds

It would appear that low Higgs masses are obtainable by choosing arbitrarily low λ values. This is not true since the terms contained in $V(\Phi)$ are only first order terms. By considering higher order one loop corrections, Coleman and Weinberg [10] claim that the effective Higgs potential becomes

$$V_{eff}(\Phi) = \mu^2 |\Phi|^2 + \lambda |\Phi|^4 + C |\Phi|^4 \ln \left(\frac{|\Phi|^2}{K^2} \right) \quad (1.33)$$

where K is some arbitrary energy scale and

$$C = \frac{(6M_W^4 + 3M_Z^4 + M_H^4 - 4\sum_f C_f M_f^4)}{16\pi^2 v^2} \simeq \frac{(6M_W^4 + 3M_Z^4 + M_H^4 - 12M_t^4)}{16\pi^2 v^2}. \quad (1.34)$$

The summation is over all leptons and quarks. $C_f = 1$ (3) for leptons (quarks) and M_t is the mass of the top quark.

Using the fact that the minimum of V_{eff} occurs at $|\Phi| = v$, and that $M_H^2 = \delta^2 V / \delta |\Phi|^2$ at $|\Phi| = v$ [9], μ^2 and K can be eliminated from Equation (1.33) to give

$$V_{eff}(\Phi) = \frac{M_H^2 v^2}{2} (2(2A - 1)B^2 - (2A - 1)B^4 + AB^4(2\ln B^2 - 1)) \quad (1.35)$$

where

$$A = \frac{Cv^2}{M_H^2}, \quad B = \frac{\sqrt{2}\Phi}{v}. \quad (1.36)$$

If A is sufficiently negative, V_{eff} is unbounded from below, above some value of B . In this unacceptable scenario, if the Higgs field (Φ) increases, it would gain more energy out of the vacuum and increase to higher values, and then all the energy in the universe could be absorbed! A summary of the M_H and M_t relation as required by vacuum stability such that the above scenario does not occur, is given in reference [12] from which Figure 1.5 was taken. More recent work by Lindner, Sher and Zaglauer [13] where they consider higher order two loop corrections to the potential $V(\Phi)$ for different choices of cut-off scale, produce the lower bound curves shown in Figure 1.6.

1.4 Higgs Production and Detection at LEP

At the present collision energies obtainable at LEP, a possible Higgs production process is via $Z^0 \rightarrow H^0 \gamma$ [9] as shown in Figure 1.7a. This process should have a clear signature because of the outgoing mono-energetic γ . However, its production rate is very low since the process is not first order. Another possible process, is via the Bjorken process [9], $Z^0 \rightarrow H^0 Z^*$ with $Z^* \rightarrow \bar{f}f$ (Figure 1.7b), its production rate is expected to be higher than that of $Z^0 \rightarrow H^0 \gamma$ because of the large HZZ coupling constant. The detection of the Higgs signal and the reconstruction of the Higgs mass are achieved by studying the outgoing fermions and the decay products of the Higgs.

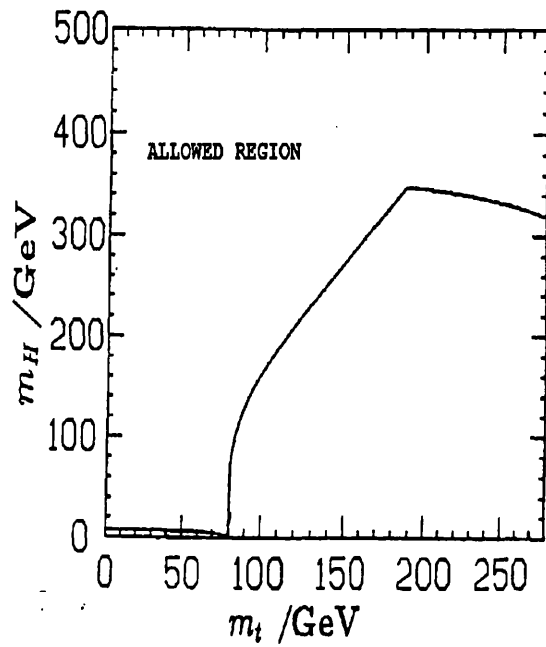


Figure 1.5: Lower bounds on Higgs mass as a function of M_t obtained by E. Gross et al.

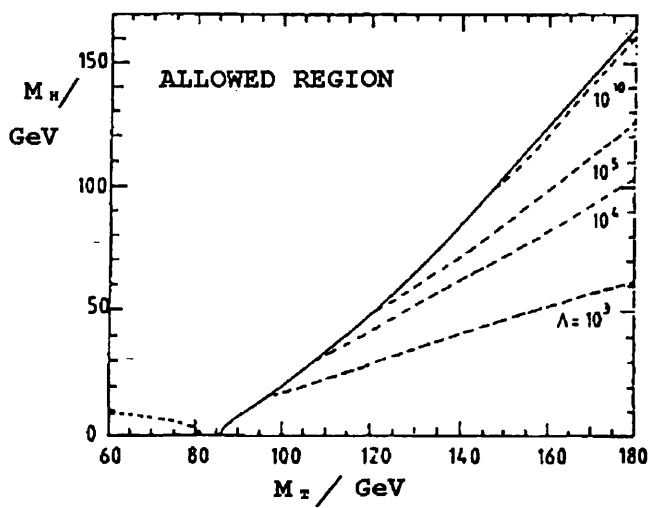


Figure 1.6: Lower bound curves for different cut-off scales Λ obtained by Lindner, Sher and Zaglauer. The solid line is for $\Lambda = 10^{15}$ GeV.

in the angular distribution of the scattered particles. They excluded the existence of a Higgs boson below 11 MeV.

The CUSB collaboration [16] have excluded the mass region below 61 MeV at 90% confidence level by combining limits on Υ decays of the type $\Upsilon \rightarrow \gamma + \text{scalar}$, with Crystal Ball [17] limits of J/Ψ decays of the type $J/\Psi \rightarrow \gamma + \text{scalar}$.

The SINDRUM collaboration [18] have searched for rare pion decays of the type $\pi^+ \rightarrow e^+ \nu_e e^+ e^-$ which are compatible with Higgs production since a Higgs in the mass range $2M_e \leq M_H \leq M_\pi$ will readily decay into an $e^+ e^-$ pair. They exclude the mass range $10 \leq M_H \leq 100$ MeV at 90% confidence level.

1.6 Previous Higgs Searches at LEP

1.6.1 Searches for $M_H < 2M_\mu$ (~ 210 MeV)

The exclusion of a Higgs boson of mass below $2M_\mu$ was performed by the ALEPH and OPAL collaborations by looking for signals which indicate the production of a Higgs boson via the Bjorken process, $Z^0 \rightarrow Z^* H^0$ where the Z^* and H^0 recoil against each other with an average momentum of about 8 GeV. Since the Higgs decays preferentially into the heaviest particles kinematically accessible, for $2M_e < M_H < 2M_\mu$, the dominant decay mode is $H^0 \rightarrow e^+ e^-$. For $M_H < 2M_e$ a major decay mode of the Higgs is $H^0 \rightarrow \gamma\gamma$. A light Higgs is also expected to be longlived or to decay mainly into neutrinos, thus not leaving any signals in the detector; it would only be observable through the decay products of the Z^* . In order to explore all the possible decay modes of the Higgs, the following decay channels were investigated:

$$Z^* \rightarrow e^+ e^- \text{ or } \mu^+ \mu^-, H^0 \rightarrow \text{undetected}$$

The experimental signature of this process is an acoplanar lepton pair with an isolated missing energy vector belonging to the undetected decay products of the Higgs. ALEPH excluded the mass region $M_H < 57$ MeV [19] whilst OPAL excluded the region below 40 MeV [20], both at 95% confidence level.

$$Z^* \rightarrow \nu \bar{\nu} \quad H^0 \rightarrow e^+ e^-, \gamma\gamma$$

The signature here is an isolated di-lepton (or two electromagnetic clusters confined to within an opening angle of 30°) with a large missing energy and momentum. OPAL excluded the mass range $30 \text{ MeV} < M_H < 2M_\mu$ at 95% confidence level [20]. ALEPH excluded the mass range $50 \text{ MeV} < M_H < 2M_\mu$ at 95% confidence level [21].

1.6.2 Searches in Range $2M_\mu$ (~ 210 MeV) $< M_H < 2M_\tau$ (~ 3 GeV)

The decay rates and modes of a Higgs boson with mass in the above mass region are subjects of controversy, but it is expected such a Higgs will decay promptly once it is produced. OPAL [22] has performed the most model-independent study in this region. To avoid any assumptions on the Higgs decay modes, they looked for the complementary channels

$$Z^* \longrightarrow e^+e^-, \mu^+\mu^-$$

$$H^0 \longrightarrow \text{Non electromagnetic decay.}$$

and

$$Z^* \longrightarrow \nu \bar{\nu},$$

$$H^0 \longrightarrow \text{An electromagnetic decay.}$$

Even though every possible Higgs decay would have passed the selection criteria, some assumptions still needed to be made in the calculation of the detection efficiencies and in the derivation of the mass limits. They excluded this mass region at 95% confidence level. Similar explorations by ALEPH [23], DELPHI [24] and L3 [25] also exclude this mass region.

1.6.3 Searches in Range $2M_\tau$ (~ 3 GeV) $< M_H$

In this mass region, the Higgs is expected to decay predominantly into $\tau^+\tau^-$ or $b\bar{b}$. The various production channels above the $b\bar{b}$ mass threshold and their relative rates are summarised in Table 1.3. At OPAL the main decay channels utilized are channels **a** **b** and **c**. Channel **e** has the largest rate but is not utilised because of very large QCD backgrounds. The other channels either suffer from low selection efficiencies or low production rates.

The signal in channel **a**, the ‘neutrino channel’, is an acolinear and acoplanar di-jet system recoiling against a missing energy vector. The signal in channels **b** and **c**, the ‘leptonic channel’, is a pair of energetic and isolated leptons recoiling against a di-jet system. As at the end of 1992, LEP’s four collaborations [26] [27] [28] [29] established the following limits:

- OPAL : $M_H > 52.6$ GeV at 95% confidence level.
- ALEPH : $M_H > 58.4$ GeV at 95% confidence level.
- L3 : $M_H > 52.0$ GeV at 95% confidence level.

- DELPHI : $M_H > 47.0$ GeV at 95% confidence level.

This thesis reports on the continuation of OPAL's search for the Higgs boson through the leptonic and neutrino channels, but with emphasis on the leptonic channel.

(using the mean branching ratios of Table 4.1)

Table 1.3: Production rates of the different decay channels of the Bjorken process.

Channel	$H^0 \rightarrow$	$Z^* \rightarrow$	Rate (%)
a	$q\bar{q}$	$\nu \bar{\nu}$	18.1
b	$q\bar{q}$	$e^+ e^-$	3.1
c	$q\bar{q}$	$\mu^+ \mu^-$	3.1
d	$q\bar{q}$	$\tau^+ \tau^-$	3.1
e	$q\bar{q}$	$q\bar{q}$	63.2
f	$\tau^+ \tau^-$	$\nu \bar{\nu}$	1.8
g	$\tau^+ \tau^-$	$e^+ e^-$	0.3
h	$\tau^+ \tau^-$	$\mu^+ \mu^-$	0.3
i	$\tau^+ \tau^-$	$\tau^+ \tau^-$	0.3
j	$\tau^+ \tau^-$	$q\bar{q}$	6.3

Chapter 2

THE EXPERIMENTAL APPARATUS

2.1 The LEP Collider

The LEP collider [30] (Figure 2.1) near Geneva, is almost 27 km in circumference and 100 m below the surface. It was designed to accelerate in opposite directions round the ring, bunches of electrons and positrons to energies of about 45 GeV each. It is envisaged that 90 GeV bunches will be collided by 1996.

The main motivation for the building of LEP was for the production of Z^0 bosons, since the counter rotating electrons and positrons can be brought into collision resulting in a centre of mass energy of 90 GeV. This useful energy can then readily be converted into matter in the form of a Z^0 , thus enabling a detailed study of it. The principal components of LEP are described in the following three subsections.

2.1.1 The Particle Injection System

The injection system was designed to produce about 1.6×10^{12} electrons and positrons every 12 minutes and inject them into the accelerator. Electrons are produced by emission from a heated filament and are accelerated to about 200 MeV in the LEP Injector Linac (LIL). Some of these electrons are used to produce positrons by directing them on to a target; bremsstrahlung photons are then produced by the rapid deceleration of these electrons as they approach the nuclei of the target. The photons subsequently convert into electron-positron pairs within the target. The positrons are magnetically extracted and together with the remaining electrons are accelerated to 600 MeV in the second stage of the LIL, and transferred into the Electron-Positron Accumulator (EPA) ring. Once a sufficient number of positrons

have accumulated, the electron and positron bunches are transferred in opposite directions into the Proton Synchrotron (PS) for acceleration up to 3.5 GeV, and then transferred into the Super Proton Synchrotron (SPS) for acceleration up to 20 GeV, and finally injected into the LEP ring for final acceleration to 45 GeV.

2.1.2 The Acceleration System

This system comprises of over a hundred radio frequency (RF) cavities powered by klystrons installed in the straight sections of the LEP ring. At present, copper RF cavities are being used at LEP. However, there are plans to use more efficient superconducting niobium cavities during the second phase of LEP where beam energies of the order 90 GeV are envisaged.

The synchrotron energy radiated per electron per revolution E is given by [31]

$$E = \frac{4\pi e^2 \beta^3 \gamma^4}{3\rho}, \quad (2.1)$$

where β is the velocity of the electron in natural units, γ is the ratio of the electron momentum to its mass, ρ is the radius of curvature of the orbit, and e is the electronic charge. The reason why LEP has such a large radius of 4.3 km, is for the minimisation of synchrotron radiation as can be seen from Equation (2.1).

2.1.3 The General Layout of LEP

Four bunches each of positrons and electrons are circulated in opposite directions through the ring, through eight interaction halls located at various points along the ring. Four of these halls have been instrumented with large detector complexes of which OPAL is one. The other three are ALEPH, L3 and DELPHI.

2.2 The OPAL Detector

This is a multipurpose apparatus¹ [32] designed for the efficient detection, accurate reconstruction and un-ambiguous classification of all the possible types of interactions occurring in electron-positron collisions, which became operational in 1989. The general layout of the detector is shown in Figure 2.2. It is made up of various sub-detectors and its main features are its

¹The detector was named as the 'Omni Purpose Apparatus for LEP', hence the acronym OPAL.

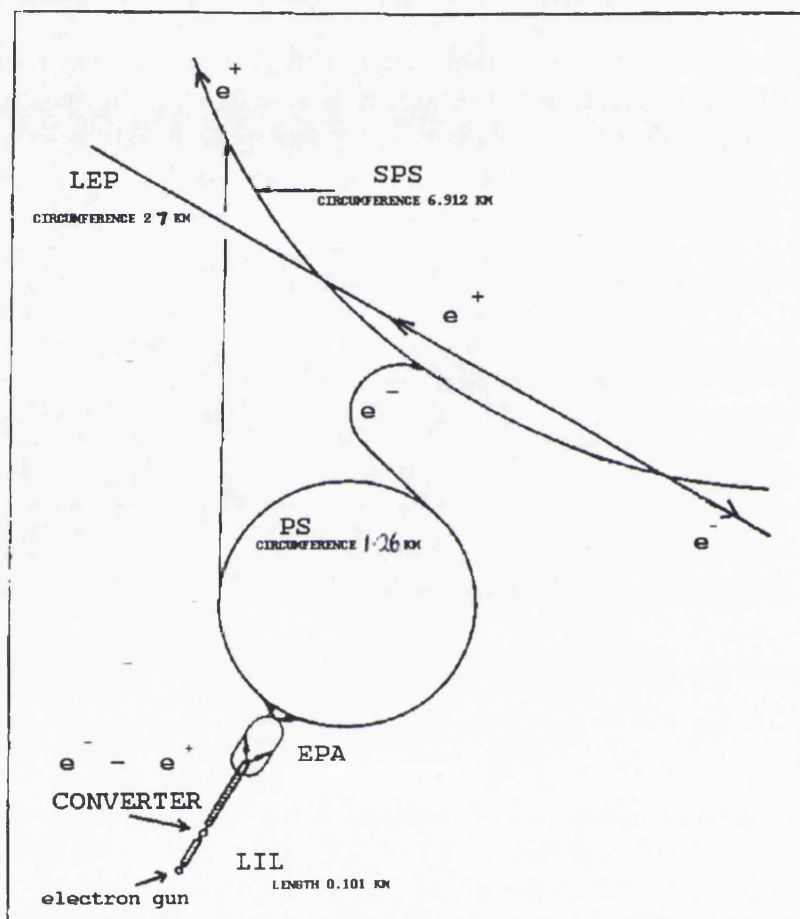


Figure 2.1: A schematic representation of the LEP electron and positron production and injection system.

- tracking of the trajectories of charged particles in the central region of the magnetic field with measurements of their directions and momentum, their identification, and the reconstruction of primary and secondary vertices at and near the interaction region using the **Central Tracking System**.
- capability to obtain timing information (*i.e.* the time a particle passes through particular positions in the detector) using the **Time-of-Flight System**.
- identification of photons and electrons, and measurement of their energy using the **Electromagnetic Calorimeters**.
- measurement of hadronic energy by total absorption using the instrumented magnet yoke as a **Hadron Calorimeter**.
- identification of muons by measurement of their position and direction within and behind the hadron absorber using the **Muon Chambers**.
- measurement of absolute machine luminosity using Bhabha events in the very forward direction with respect to the beam line, using the **Forward Detector** or the **Silicon-Tungsten Luminometer**.

2.2.1 The OPAL Coordinate System

The z -direction is along the beam direction (this is anti-clockwise when LEP is viewed from above), the x -direction points towards the centre of the LEP ring, and the y -direction is normal to the z - x plane. Since the z -direction is inclined by 1.39° with respect to the horizontal, it follows that the y -direction is similarly inclined with respect to the vertical. Quite often a mixture of cylindrical and spherical coordinates is used, where the z -direction is as usual, θ -direction is the polar angle with respect to the beam axis, and ϕ is the azimuth.

2.2.2 The OPAL Magnet

The magnet consists of a solenoidal coil and an iron return yoke. The yoke is made of soft steel plates and can be split into 5 main parts; a central part, two 'C'-shaped parts and two poletips. In the central cylindrical volume (used for tracking) the magnetic field is about 0.435 Tesla. Particle momenta and charge are determined by the curvature of their tracks in this field at around the interaction point.

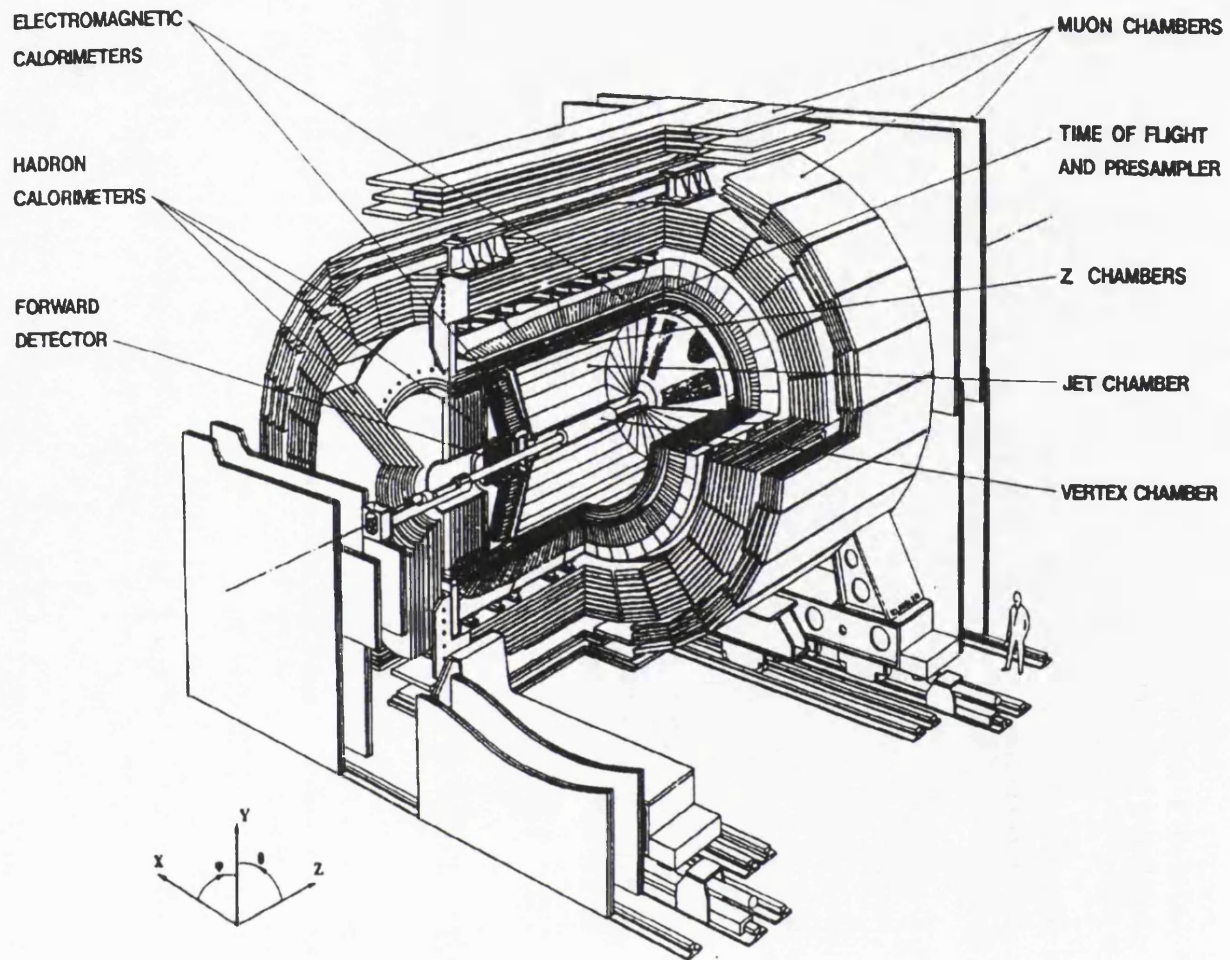


Figure 2.2: A labelled diagram of the OPAL detector.

2.2.3 Detectors of the Central Tracking System

The central tracking system consists of the silicon microvertex detector, the vertex detector, the jet chamber and surrounding Z -chambers situated inside a pressure vessel holding a pressure of 4 bar. The tracking system is inside the solenoid of the magnet. Before 1991, there was no silicon microvertex detector and the inner wall of the pressure vessel at 7.8 cm radius from the interaction point, formed the beam pipe. This beam pipe consists of 0.13 cm thick carbon fibre with a 100 micron aluminium inner lining. In 1991 a second beam pipe at a radius of 5.35 cm, consisting of 0.11 cm thick beryllium was added and the silicon microvertex detector inserted between the two beam pipes.

The Silicon Micro-Vertex Detector

This is a solid-state detector installed in 1991, two years after OPAL became operational. It is barrel-shaped and surrounds the inner beam pipe. The motivation for this detector was the need to measure and identify particles with typical decay lengths of below a centimetre (such as heavy hadrons and the tau lepton), and to search for new particles having similar decay lengths.

The basic unit of this detector is the ‘ladder’ which is rectangular shaped. Each ladder consists of three square pairs of back-to-back ϕ and z position miniature semiconductor detectors aligned length-wise in a row. Eleven ladders form the inner cylindrical detection layer and 14 ladders form the outer detection layer, both layers having radial positions of 61 mm and 75 mm respectively. The ladders are arranged such that the small gaps in the ϕ coverage do not line up thus ensuring a near 100% coverage. Single hit² resolution is about 5 μm .

The Vertex Detector

The vertex detector is a 1 m long, 470 mm diameter cylindrical drift chamber that surrounds the outer beam pipe. It consists of an inner layer of 36 axial cells with axial wires, and an outer layer of 36 stereo cells with wires strung at a stereo angle of 4°.

The axial cells provide a precise measurement of position in the r - ϕ plane with a resolution of about 50 μm . This detector aids in the measurement of secondary vertices. Good drift time resolution is obtained by having a 4 bar gas pressure and by limiting the maximum drift distance in order to reduce diffusion effects³.

²A pulse on the detector electrodes caused by the transversal of a single charged particle

³Electrons liberated by a traversing particle, diffuse in all directions before drifting towards the sense wires. This can lead to inaccuracies if threshold electronics are used to determine drift times.

A rough measurement of the z -coordinate of a hit along a signal wire is done by measuring the time difference between the signals from the two ends of the wire. This coarse measurement is used in the fast track trigger⁴ and for offline track finding. The combination of the stereo and axial cell information provides an accurate z -coordinate measurement for charged particles close to the interaction region.

The Jet Chamber

The jet chamber is a large proportional chamber designed to combine good space and double track resolution, which are essential for the determination of momentum, the efficient recording of jet-like events and the possibility of particle identification within a solid angle close to 4 steradians. The sensitive volume of the jet chamber is a cylinder with a length of about 4 m surrounding the beam pipe and the vertex detector. The outer diameter is 3.7 m and the inner, 0.5 m. The chamber is subdivided into 24 identical sectors each containing a plane with 159 sense wires. Cathode wire planes form the boundaries between adjacent sectors. All wires are strung parallel to the beam direction, whilst the wire planes are radial. The maximum drift distance varies from 3 cm at the innermost sense wire, to 25 cm at the outermost wire.

In the polar angular range between 43° and 137° , 159 points are measured along each track, and at least 20 points on a track are obtained over a solid angle of 98% of 4 steradians. For each point, three-dimensional coordinates (r, ϕ, z) are determined from the wire position, the drift time and from a charge division measurement. The charge division method requires the measurement of the integrated charges for each hit at both ends of the signal wire. The ratio of these charges determines the z -coordinate, and their sum is used to calculate the rate of energy loss dE/dx of the particle in the gas, which aids in particle identification. The average resolution of the dE/dx measurement is 3.5% for 159 samples. The momentum in the r - ϕ plane (p_t) is measured with a resolution given by [30]

$$\frac{\sigma(p_t)}{p_t} = (0.02^2 + (0.0015|p_t|^2)^{\frac{1}{2}})^{\frac{1}{2}}, \quad (2.2)$$

where p_t is in GeV/c.

The Z-Chambers

These chambers, as their name implies make precise measurements of the z -coordinates of charged particles as they leave the jet chamber and thus improve polar angle resolutions. They cover a polar angular acceptance from 44° to 136° and 94% of the azimuthal angle. They consist of 24 drift chambers, 4 m long, 50 cm wide and 59 mm thick.

⁴An electronic logic that identifies signals from a set of signal wires as due to the traversal of a particle.

Each chamber is divided across z into eight 50 cm by 50 cm cells so that the maximum drift distance is about 25 cm in the z -direction. Each cell has six anode wires strung along the ϕ direction.

2.2.4 The Time-of-Flight System

The time-of-flight (TOF) system covers the barrel region ($|\cos\theta| < 0.82$). It generates trigger signals and by measuring the time of flight from the interaction region, allows the identification of charged particles with momentum in the range 0.6 to 2.5 GeV. It also aids in the rejection of background particles such as cosmic rays. The TOF system consists of 160 scintillation counters forming a barrel of radius 2.36 m.

2.2.5 The Electromagnetic Calorimeter

The electromagnetic calorimeter is a total absorption calorimeter which detects and measures the energies and positions of electrons, positrons and photons ranging from tens of MeV to 100 GeV. It provides neutral-pion/photon discrimination and, in conjunction with the central tracking system, electron/hadron discrimination. It consists of three large overlapping assemblies of lead-glass blocks (the barrel and the two end caps). Most electromagnetic showers are initiated before the lead-glass itself because of material such as the magnet coil and the pressure vessel in front of the calorimeter. For this reason, presampling devices are installed in both the barrel and end-cap regions, immediately in front of the lead-glass to measure the position and to sample the energies of these pre-showers, thus improving energy resolution. The intrinsic resolution of the calorimeter is $5-6\% / \sqrt{E}$, where E is the energy (in GeV). This resolution is degraded by a factor of about two by the material in front of it. The effect of the material is more significant near the overlap of the barrel and the endcap calorimeters *i.e.* at polar angles defined by $0.72 < |\cos\theta| < 0.84$. The angular resolution of electromagnetic clusters is approximately 4 mrad both in θ and ϕ for energies above 10 GeV.

The Barrel Pre-Sampler

The barrel electromagnetic presampler consists of a cylinder of limited streamer mode wire chambers located between the time-of-flight system and the barrel lead-glass calorimeter. It consists of 16 chambers covering the surface of a cylinder of radius 2.388 m and length 6.623 m. Each chamber has two layers of limited streamer mode tubes with sense wires running axially.

The Barrel Lead Glass Calorimeter

This is a cylindrical array of 9440 lead glass blocks located at a radius of 2.455 m, outside the magnet coil, covering the full azimuthal angle and a polar angular region defined by $|\cos\theta| < 0.82$. The longitudinal axes of the lead glass blocks point towards the interaction region to minimize the probability of a particle traversing more than one block. However, the blocks are tilted slightly away from a perfect pointing geometry to prevent neutral particles from escaping through the gaps between the blocks. A traversing particle usually deposits energy in a cluster of bordering lead-glass blocks.

The Endcap Pre-Samplers

Each endcap presampler is an umbrella shaped arrangement of 32 wire chambers in 16 sectors located between the pressure bell of the central tracking system and the endcap electromagnetic calorimeter, covering the full azimuthal angle and a polar angular region defined by $0.83 < |\cos\theta| < 0.95$.

The Endcap Calorimeters

The endcap electromagnetic calorimeters consists of two dome-shaped arrays of 1132 lead glass blocks, located between the pressure bell of the central tracking system and the pole tip hadron calorimeters, covering the full azimuthal angle and polar angle range $0.81 < |\cos\theta| < 0.98$.

2.2.6 The Hadron Calorimeter

This measures the energy of hadrons as they emerge from the electromagnetic calorimeter and assists in the identification of muons. It consists of three sections; the barrel, the endcap, and the poletip. The iron of the magnet return yoke is segmented into layers with planes of wire chambers between each layer thus forming this cylindrical sampling calorimeter about 1 m thick.

The Barrel and Endcap Hadron Calorimeter

The barrel consists of 9 layers of wire chambers alternating with 8 iron slabs and spans radii from 3.39 to 4.39 m. The slabs are 100 mm thick with 25 mm gaps. The barrel is closed at each end by a doughnut-shaped endcap, which consists of 8 layers of chambers alternating with 7 slabs of iron. Since there is a high probability

of hadronic interactions being initiated in the material before the hadron calorimeter, the overall hadronic energy is determined by combining signals from both the electromagnetic and hadronic calorimeters.

The signals from the calorimeter are read out with narrow strips, and cathode pads in the layers which are grouped together to form ‘towers’. The signals from the towers are used for energy measurements whilst those from the strips are used for tracking and muon identification.

The Pole-Tip Hadron Calorimeters

The pole tip hadron calorimeters which consist of 10 layers of wire chambers each, complement the barrel and the endcap ones by extending the solid angle coverage from $0.91 \leq |\cos \theta| \leq 0.99$. The active elements of these detectors are thin (7 mm overall thickness) multiwire chambers operating in a high gain mode.

2.2.7 The Muon Chamber

The muon detector is also a system of wire chambers constructed as a barrel and two end caps, covering the iron yoke almost completely. While most muons penetrate to the muon detector and leave a single clean track, most hadrons are absorbed in the iron yoke. Nearly all the solid angle is covered by this detector. The amount of material that a particle has to traverse before reaching it, exceeds the equivalent of 1.4 m of iron. This is required in order to reduce the probability of a pion not interacting, thus faking a muon, to less than 0.001. There are two processes by which a hadron can fake a muon:

- Sneakthrough, which is the failure of a hadron to interact strongly in the hadron calorimeter.
- Punchthrough; here, the hadron interacts in the hadron calorimeter but secondary particles emerge and fake a muon. This phenomenon is important at high momenta.

The barrel part of the detector covers $|\cos \theta| < 0.68$ with four layers of drift chambers, and $|\cos \theta| < 0.72$ with one or more layers. The end cap part, covers the range $0.67 < |\cos \theta| < 0.98$.

Muon identification relies on extrapolating the track seen in the central tracking system through the iron absorber, allowing for energy loss and multiple scattering, and looking for a track in the muon detectors which matches in position and angle, in the yz and xy views.

2.2.8 The Silicon-Tungsten Luminometer

The silicon-tungsten luminometer was installed in 1991 and comprises two face-to-face cylindrical small angle electromagnetic calorimeters encircling the beam pipe. They are at 2.4 m on either side of the interaction point. Each calorimeter is made of a stack of 18 tungsten plates (for shower initiation), interleaved with 19 layers of silicon sampling miniature detectors and mounted as two interlocking 'C'-shaped modules around the beam pipe. The sensitive area of the luminometer covers the radii between 62 and 142 mm from the beam axis thus having a clean acceptance for particles in the range 25 to 59 mrad. In addition to luminosity measurement, the luminometer is used in tagging some two photon interactions.

2.2.9 The Forward Detector

The forward detector which also comprises two face-to-face detectors, is used mainly for the tagging of two photon interactions and for luminosity measurements. This detector has a relatively clean acceptance for particles between 47 and 120 mrad from the interaction point. Its main components are the drift chambers, the electromagnetic calorimeters, the proportional tube chambers, the far forward monitor and the gamma catcher.

Two planes of drift chambers are mounted in front of the calorimeter. Those in the rear plane are known as the Large Angle Drift Chambers (TC2s). Before 1991, the drift chambers in the front plane were TC1s. Since then, drift chambers of a different design (see chapter 3) have replaced the TC1s; they are known as the Small Angle Reference Chambers (SARCs). The calorimeters accurately measure the energy deposited by a traversing electron. They also measure shower position and give shower development information through their longitudinal segmentation. Each calorimeter is divided into two longitudinal sections, the presampler and the main sections. Situated between these two sections are the proportional tube chambers which measure the position in θ and ϕ of an electromagnetic shower near its maximum development. The far forward monitor consists of small lead-glass scintillator calorimeter modules, mounted on either side of the beam pipe 7.85 m along the z -direction from the interaction region; they detect electrons scattered in the range 5 to 10 mrad that are deflected outwards by the action of the LEP quadrupole magnets.

2.3 The Trigger and Online System

At LEP, the electron and positron bunch crossings occur with a frequency of 45 KHz. The data acquisition system cannot record information at such a rate.

The general trigger system is a flexible and programmable system which uses fast information (subdetector triggers) from the subdetectors to reject background interactions (such as from cosmic rays, beam-gas and beam-pipe interactions), and to select only interesting bunch crossings (*i.e.* ones with a possible electron-positron interaction), thus reducing the bunch crossing rate to an effective event rate of 1-5 Hz which can be handled by the data acquisition system.

2.3.1 The Event Trigger and its Logic

The trigger system is designed to provide a high recognition efficiency of the various physics reactions and good rejection of backgrounds arising from cosmic rays, from interaction of beam particles with the gas inside the beam pipe or wall of the beam pipe, and from electronic noise. Most of the physics reactions are triggered by several independent conditions imposed on the sub-detector signals.

The full solid angle covered by the OPAL detector is divided into 144 overlapping volumes or bins, 6 bins in θ and 24 bins in ϕ . The subdetectors deliver trigger signals matched as closely as possible to this binning. Besides the θ - ϕ signals, the subdetectors deliver stand-alone signals derived from total energy sums or track counting. The θ - ϕ signals are used for hit counting, for the definition of back-to-back hits and to build detector coincidences correlated in space. Programmable conditions are imposed on the θ - ϕ matrix outputs and on stand-alone signals to decide whether an event is accepted or rejected. An overview of the θ - ϕ matrix is given in Figure 2.3.

The Central Trigger Logic

The central trigger logic is installed in a dedicated Eurocrate, with a special 'trigger bus' in addition to the standard VME/VSB bus. Logical combinations of signals on the trigger bus (*i.e.* subdetector stand-alone signals and θ - ϕ matrix outputs) are formed by the 'pattern arrangement module' (PAM), which uses look-up memories to derive the trigger decision from the 120 possible outputs. The trigger decision is broadcast to the Local Trigger Units (LTU) in each subdetector readout crate by the Global Trigger Unit (GTU). If the trigger decision is negative, a reset pulse is distributed 6 μ s before the next bunch crossing. If the event is to be accepted and read out, the GTU generates a trigger pulse, and transfers a central event number and the 120 PAM input bits to the LTUs.

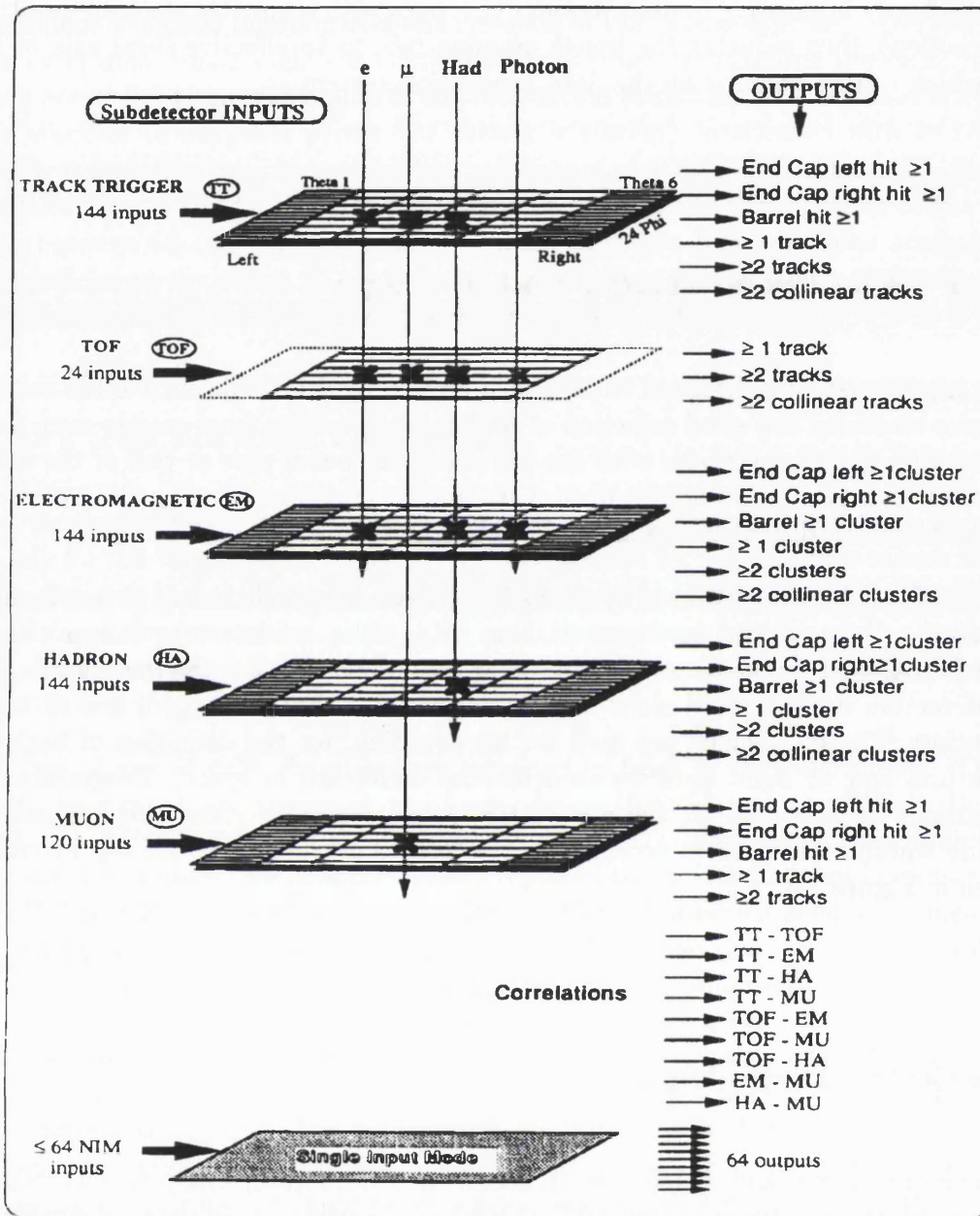


Figure 2.3: An overview of the trigger generation by the θ - ϕ matrix. The track trigger (TT), the time-of-flight system (TOF), the electromagnetic calorimeter (EM), the hadron calorimeter (HA) and the muon detector (MU) send signals to the θ - ϕ matrix, the outputs of which are logically combined to form the final trigger decision. Crosses on the vertical line representing different particle types passing through the detector indicate the sensitivity at the trigger level.

2.3.2 The Data Acquisition and Processing

The readout system has a distributed tree structured architecture. Microprocessors of the 68020/68030/68040 type, running the OS9 operating system are used in the VMEbus based system for data compression, data moving and monitoring. The VME crates are interconnected using a fast parallel link for (sub-)event routing. The sub-events containing the digitized information of the subdetectors are buffered into memories controlled by the subdetector processors and then collected and merged into a single data structure by an 'event builder' VME system. This system also acts as an event buffer for a microprocessor matrix, where ten 68030s perform a first analysis of the complete events. The undesired background are also rejected at this stage. From here, events are transferred from the underground experimental area via an optical link to the surface. Finally, the events are transferred to the main online computer, a VAX 8700 and stored on magnetic tapes. The data collection and processing is shown schematically in Figure 2.4.

2.4 The Slow Control System

The slow control system ensures the safe operation of the detector and also serves as a homogeneous interface to all the subdetectors, and to the general infrastructure of the experiment. The system consists of two parts, the first part supervises the common environment including safety aspects, and the second part is specific to each subdetector. The parameters of the common infrastructure such as voltages, gas flow, temperatures are continuously monitored by 7 VME stations. All values are compared to their nominal settings written to a file, and when problems arise, the system notifies the operator and takes automatic corrective actions if required. One station is also connected to the data acquisition system in order to include the control data in the physics event record.

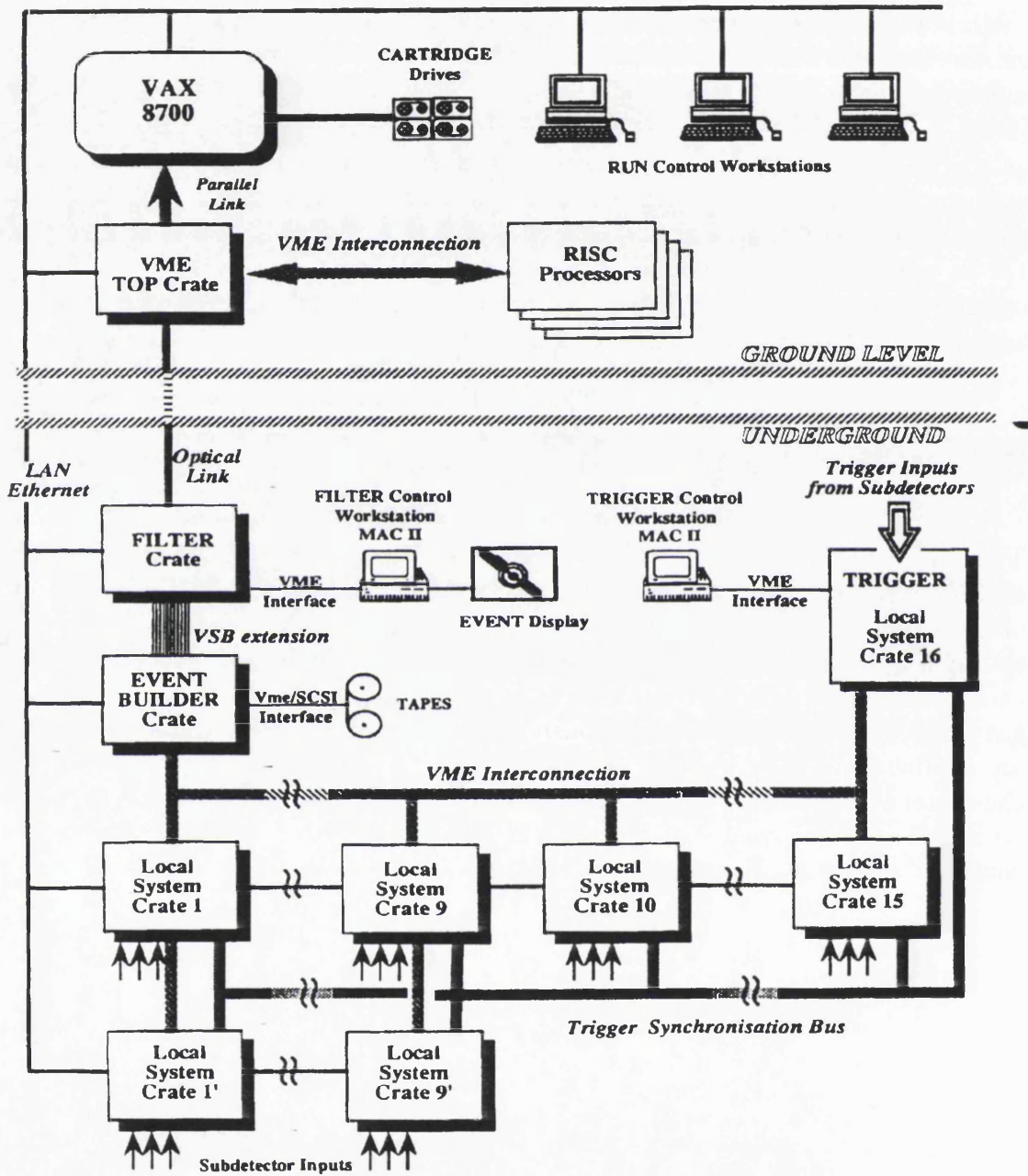


Figure 2.4: The overall scheme of event triggering, readout, monitoring and data handling.

Chapter 3

LUMINOSITY MEASUREMENT WITH THE FORWARD DETECTOR

In this chapter, the forward detector's drift chambers and the measurement of the LEP luminosity at OPAL, are described. A small software package written by the author to rectify a fault the drift chamber readout system had during their 1991/1992 operation is presented.

3.1 The OPAL Forward Detector

The OPAL forward detector (Section 2.2.9) is shown schematically in Figure 3.1. In forward detector survey measurements, it is useful to describe positions and distances in millimeters of radius. The radius is referred to the front face of its calorimeter (from the nominal interaction point), where 2 mm in radius corresponds to about 1 milliradian in θ . Another useful coordinate is the V direction, which is parallel to the radial direction at the centre of each quadrant, 45 degrees away in ϕ from the horizontal and vertical, and measured in millimetres at the front face of the calorimeter (Figure 3.2).

3.2 The Forward Detector Drift Chambers

The drift chambers [33] are used for tube chamber survey purposes. A typical Large Angle Drift Chamber (TC2) is lozenge-shaped with two gas compartments 11 mm deep. Each compartment contains two sense wires and a field shaping wire, all

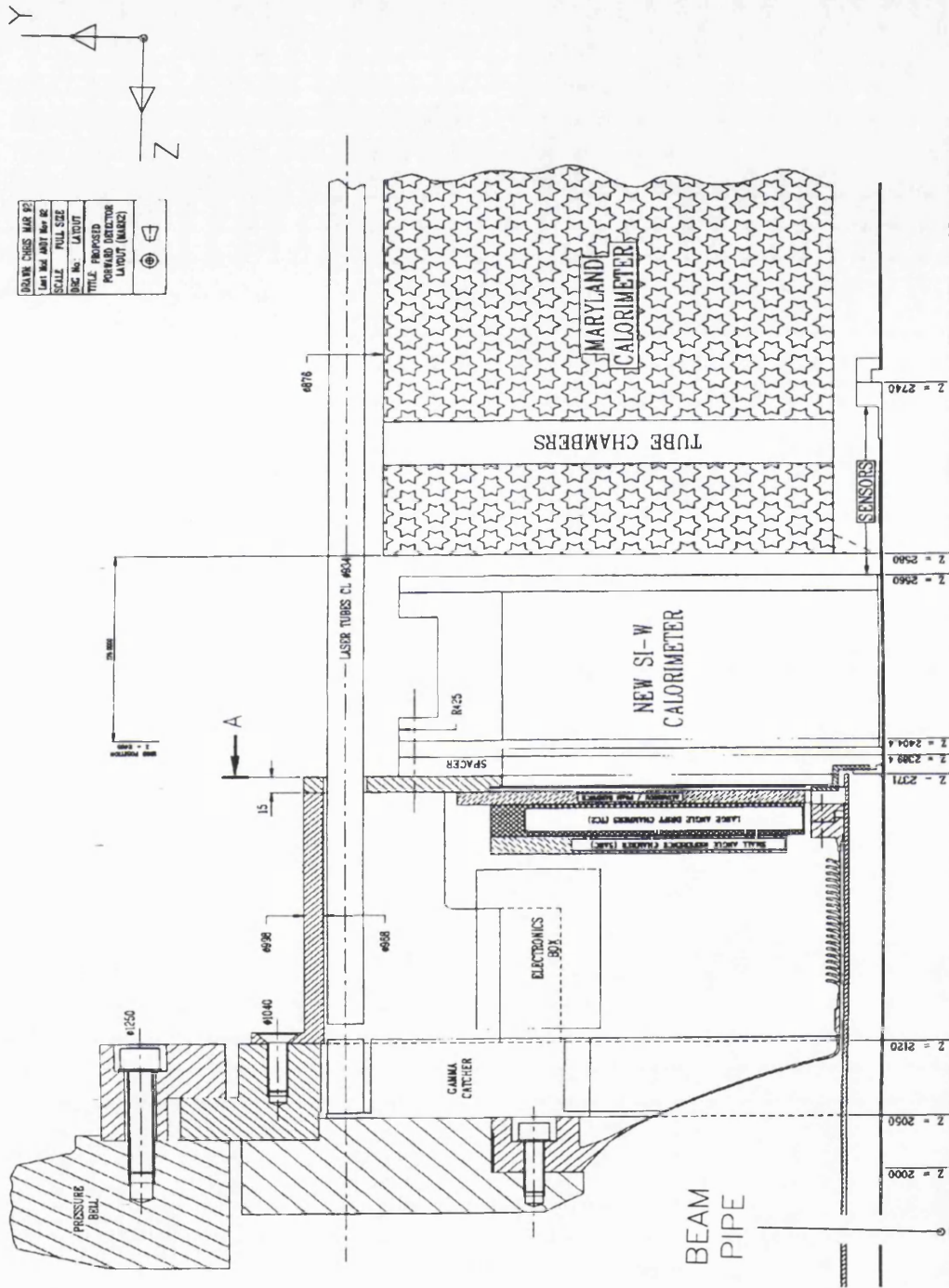


Figure 3.1: A labelled cross section of a quadrant of the forward detector in its 1993 configuration (turn page on its long side for better viewing).

stretched across the longest 400 mm diagonal (Figures 3.2 and 3.3). Glass reinforced epoxy frames form the outer walls of both compartments, with field-shaping copper strips on the faces of the chamber partitions. The perpendicular distance from the wire to a track is deduced from knowledge of the drift time and the drift velocity of the electrons produced by ionization. A stagger of 2 mm between the wires in the two compartments (Figure 3.3) is necessary in order to resolve the ambiguity between tracks above and below the sense wires. The induced pulses produced by the electron drift on both ends of a sense wire are read out separately to give a rough estimate by charge division of the coordinate along the wire of a track. More precise information on the coordinate is obtained from the induced pulses on sets of cathode pads on the inside faces of the chambers. The induced signals on the sense wires and on the pads are amplified using LM 733 differential amplifiers with the necessary shaping and gain networks (Figures 3.4 and 3.5). The amplified signals are digitized by the DL300 data acquisition system [35]. The Small Angled Reference Chambers (SARCs) are similar in design to the TC2s but with the following three major differences:

- Each SARC has only one gas compartment containing two sense wires.
- SARC sense wires are placed lower in the chamber, close to the inner edge of the forward detector acceptance.
- The SARCs are smaller in size.

There are a total of 4 SARCs and 4 TC2s (installed behind the SARCs) at each end of the forward detector (Figure 3.2).

DL300 : The Drift Chamber Data Acquisition System

This is a modular multi-channelled data acquisition system based on ultra fast integrated analogue to digital convertors (FADCs). The system was originally designed for the OPAL Jet Chamber by the University of Heidelberg and was manufactured by Dr. Struck [35].

This system measures the amplitude of a signal (produced by the drift electrons) by inputting it to each of a series of comparators, thus comparing it to a reference voltage which increases for each comparator. The reference voltages are picked off a resistor chain. The fixed reference voltages, V and the ground potential, which are applied at each end of the reference chain, determine the maximum and minimum signal size the FADC can measure (Figure 3.6). The signal voltage is digitized by determining the first comparator for which the signal voltage is greater than its reference voltage. The DL300 can sample pulses at frequencies up to 100 MHz and its basic elements are the

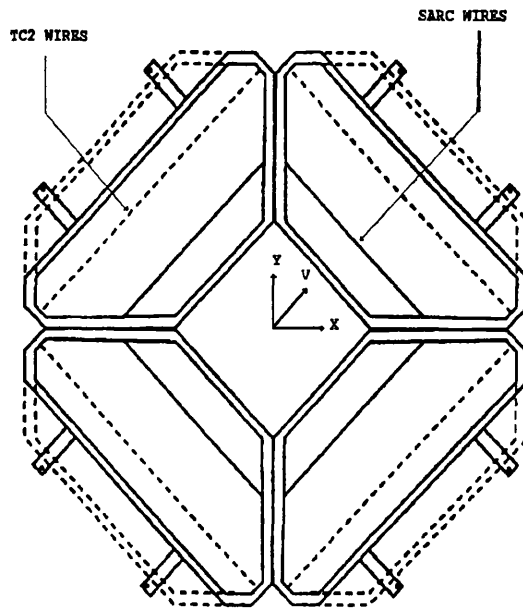


Figure 3.2: A head-on view of one half of the forward detector showing only its coordinate system used for survey measurements and the four quadrants of drift chambers. The SARCs shown in the solid lines are mounted in front of the TC2s (dashed lines).

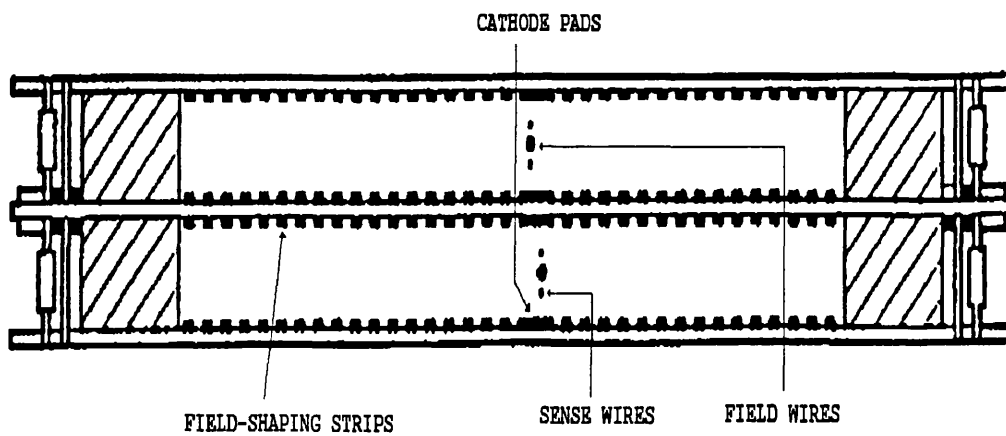


Figure 3.3: A cross section of a Large Angle Drift Chamber (TC2) showing its sense (field) wires as the small (large) black circles. The field-shaping copper strips are shown as the rectangles on the faces of the chamber partitions.

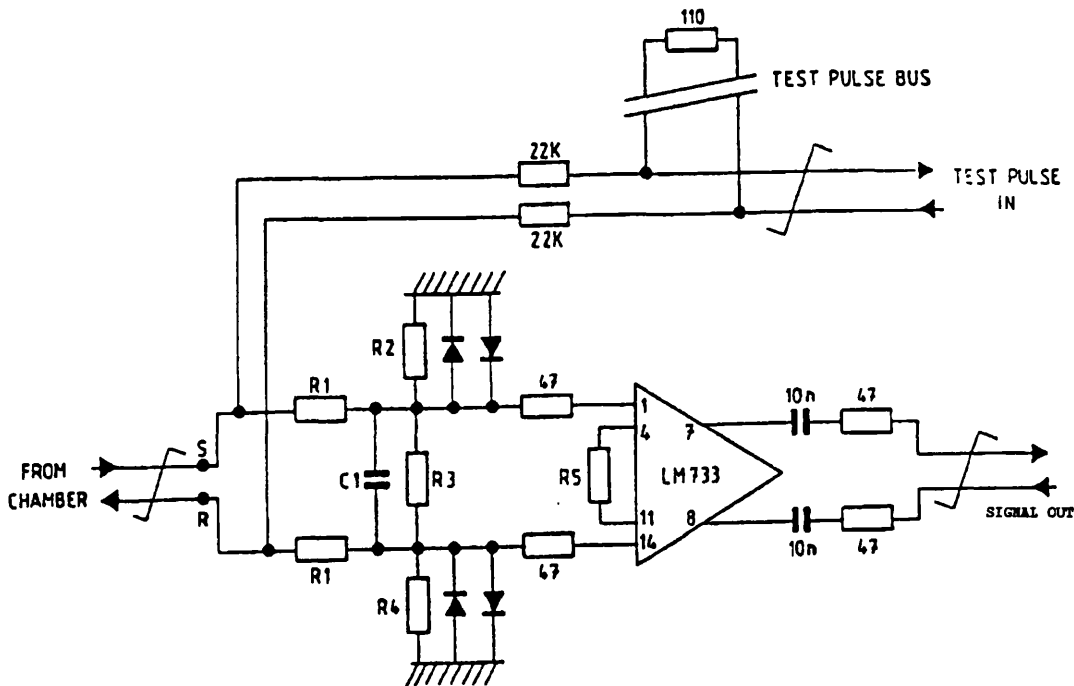


Figure 3.4: Pad amplifier circuit. The return side of the wire preamplifier circuit is grounded.

- data acquisition modules DL305, each containing four FADC chips and a 256 byte memory per channel (chip). Each byte consists of 6 bits, which means that a byte can only store a sample value not greater than 64. To ensure the storage of larger sample values, the response of the FADC is made non-linear such that small signals are digitized with an 8-bit resolution whilst the larger signals are digitized with a 4-bit resolution. This non-linear response is achieved by feeding part of the measured signal into the resistor chain via the resistor R2 (Figure 3.6). The relation between the digitized sample value S' and the true sample value S is given by [34]

$$S' = \frac{64S}{64 + 0.75S} \quad (3.1)$$

- controller module DL302 which is the scanner and hit detector. It controls the sampling and digitization and also identifies memory locations which contain data (scanning process) in the FADC modules.
- interface module DL301 which allows connection to a VME processor for full computer control of the whole system.
- monitor module DL309 which serves as a bus (a set of shared lines for exchanging digital information) monitor, memory module and a programmable digital-to-analog convertor for testing purposes.

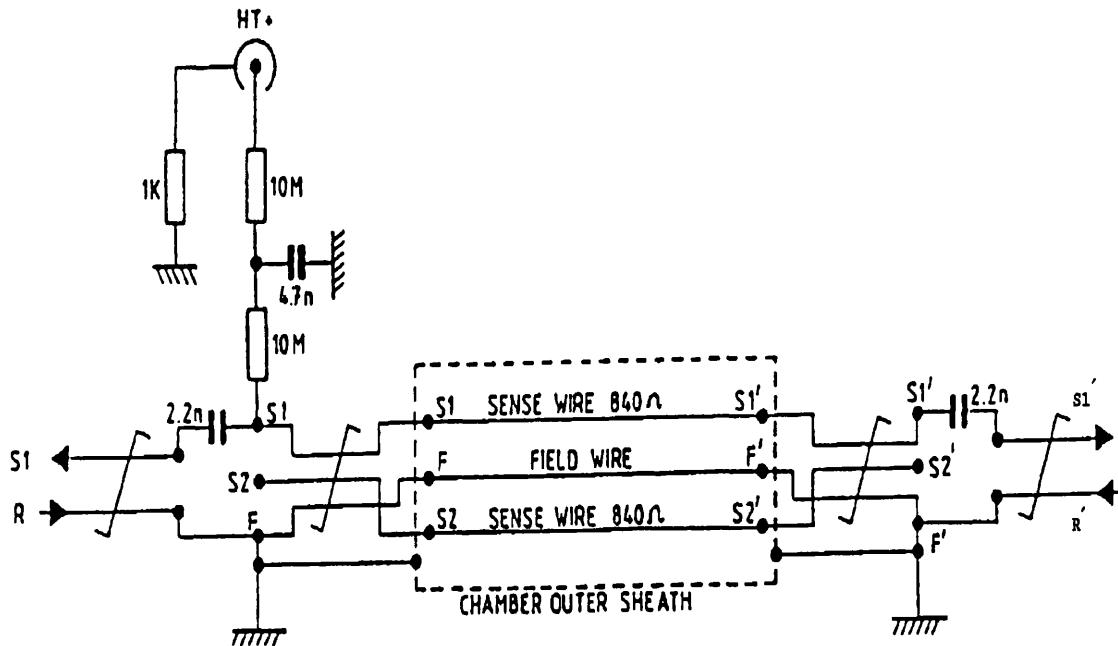


Figure 3.5: Sense wire and field wire circuit. The connections for the wire S2 are similar to those for S1.

The upper part of the DL300 backplane is the analog backplane, used to connect the FADC modules DL305 to the drift chamber outputs. The signals from two wires *i.e.* four channels, are digitized by one FADC module. Two sets of cathode pads from a chamber are assigned to a module.

Scanning: The First Step in the Readout Process

Scanning is the stage where valid data (hits) are preselected for further study at the pulse shape analysis stage. After the digitization has been completed, which occurs when the scanner reaches a pre-defined address in the FADC memories, the scanner then performs a search for a hit. A hit is defined as starting when two adjacent bytes in either the left or right channel of a wire are above a selected threshold, and ends when two adjacent bytes are below this threshold. All FADC modules within a defined range are selected sequentially via their module address and read out. When a hit is found, the hit detector stops the search and then sets a hit flag. This flag is an electronic signal which generates a Processor Request Signal (PRS) via the scanbus which then generates an interrupt to the VME processor. The stop address is used as a pointer to the hit. The scanner is re-started by the control software and continues the search for other hits, while the VME processor starts the readout via

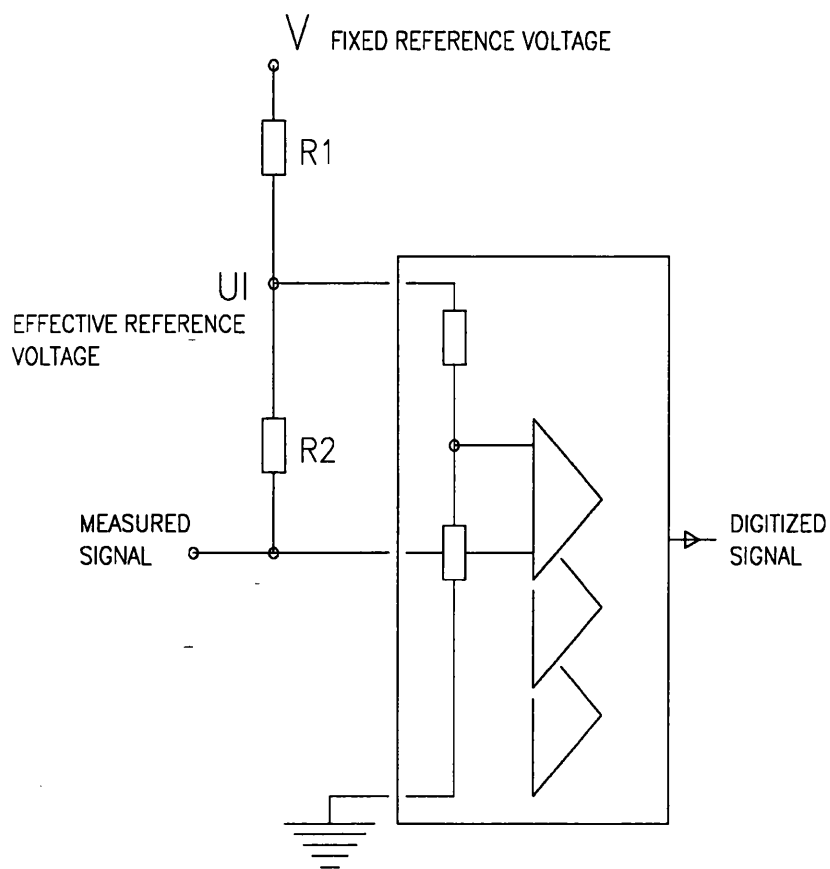


Figure 3.6: A description of the digitization of a signal using comparators.

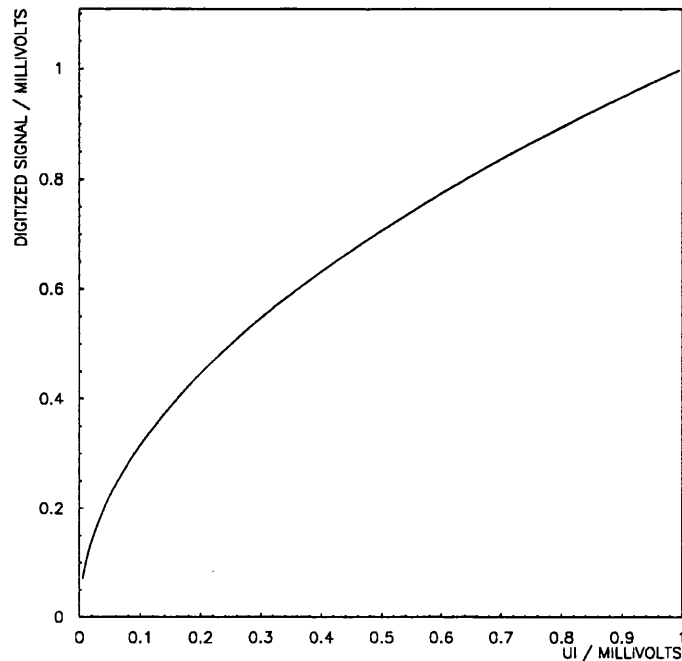


Figure 3.7: The non-linear response function produced by the resistor **R2**.

the interface.

3.3 Pulse Shape Analysis

The advantages of digitizing pulses before analysing them are as follows:

- A good energy determination of the traversing particle is possible.
- An accurate drift time determination is possible which is less sensitive to diffusion
- Excellent multihit resolutions are possible.

For single well separated pulses in the chamber, the pulse definition and time measurement present no problems. This is not the case for complex track patterns as they occurs in, say, jets. An algorithm was developed to reduce this difficulty. This method, known as the Difference of Samples [34], is based on the difference between neighbouring samples, $D = A_i - A_{i-1}$, where i takes values between 2 and the total number of samples to be read out N_S . A_i is the amplitude in the i th sample

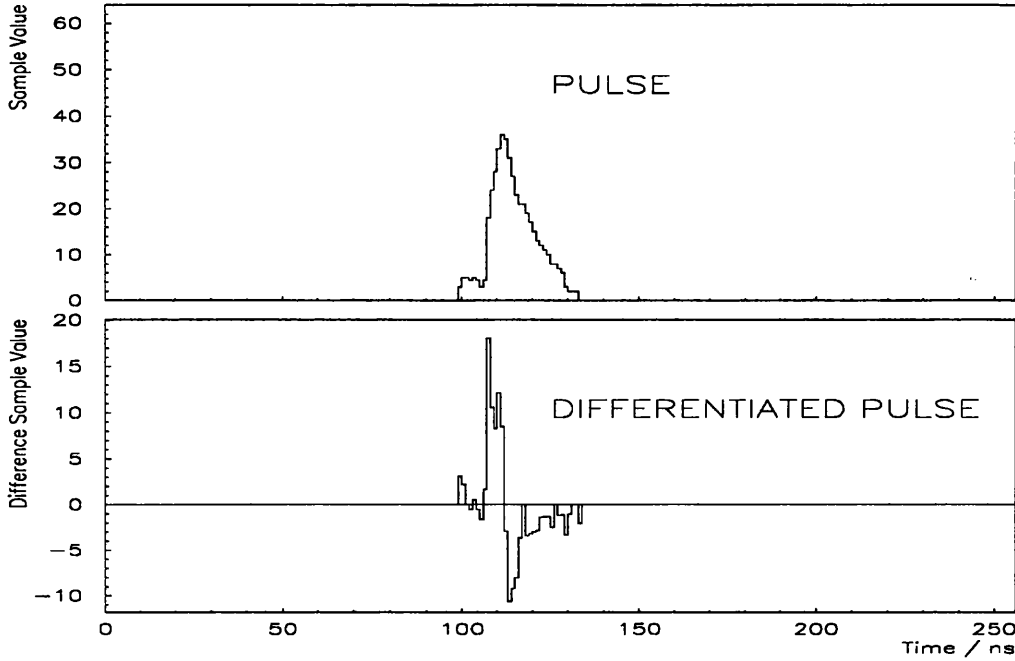


Figure 3.8: A snapshot of a typical pulse and its differentiated pulse after correction for the non-linear response.

after correction for the non-linear response function (equation (3.1)). A comparison of the differentiated pulse with the original one, shows that large components of the difference correspond to the rising edges of the pulses (Figure 3.8).

The start of pulses are defined as two consecutive differentiated samples above a certain threshold. The essential timing information is contained within a small region surrounding the peaks of the differentiated pulse (two samples on both sides of the peak). The drift time T_d is given by the following weighted mean [34]

$$T_d = \left(\frac{\sum_i w_i n_i h_i}{\sum_i w_i h_i} \right) 20 \text{ ns}, \quad (3.2)$$

where w_i with $i = -2 \dots 2$, are optimal weight factors which are given by 2.0, 1.5, 1.0, 0.7 and 0.5 respectively, h_i is the sample value and n_i is the sample position.

Luminosity Measurement at OPAL

It is essential that the luminosity of the colliding electrons and positrons at OPAL is determined to the greatest precision possible since it is a fundamental parameter

necessary in calculating the cross-section of any interaction and in predicting the number of expected Higgs events.

The luminosity determination at OPAL is achieved by counting the rate N of Bhabha interactions within a small angular acceptance. Bhabha scattering, the elastic scattering of colliding electrons and positrons, is well described by Quantum Electrodynamics so its cross section can be calculated with great accuracy. The differential cross section is given approximately by [59]

$$\frac{d\sigma}{d\Omega} = \frac{\alpha^2(\cos^2\theta + 3)^2}{16E_b^2(1 - \cos\theta)^2}, \quad (3.3)$$

where α is the fine structure constant, E_b is the beam energy, θ is the polar angle of the outgoing electron, and ϕ is its azimuth. The rate N is related to the luminosity L , the cross section σ within a defined angular acceptance and the efficiency ϵ of counting the events by

$$N = \sigma L \epsilon. \quad (3.4)$$

At small polar angles, the following approximate relation holds,

$$\sigma \propto \frac{1}{\theta_{min}^2} - \frac{1}{\theta_{max}^2}. \quad (3.5)$$

Bhabha electrons are preferentially scattered in the forward directions, and the cross section is very sensitive to errors in the definition of the angular acceptance. In the forward detector, the angular acceptances are defined by the tube chambers. In order to reduce any uncertainties in the definition of the angular acceptance, one needs to have a good knowledge of the effective positions of the tube chamber wires. A map of the defective tube chamber wires is also needed.

The drift chambers are used to survey the tube chamber positions because the positions of their sense wires are more precisely known than those of the tube chambers which are imbedded within the calorimeters and thus not easily accessible (Figure 5.1).

The Tube Chamber Survey

To determine the absolute positions of the tube chambers in θ through locally determining the radial distance of the tube chambers from the nominal beam position, single electron tracks were reconstructed in the drift chambers and compared with the corresponding tracks reconstructed by the tube chambers. Two methods were employed to determine the placement of the tube chamber wires in 1991. These were the 'Double V plot' and the '3-Line plot' analyses. Only the second method which was relevant to my work with the drift chambers will be discussed here.

The 3-Line plot analysis involved using data from 3-line plots (see below) to determine the drift chamber V coordinates of hits. The drift velocities u and the

start times t_0 as obtained from the plots are used to calculate the V coordinate for each hit on the drift chamber wires, using equations (3.6) and (3.7)

$$V^s = V_0^s + u^s(t^s - t_0^s) \quad (3.6)$$

$$V^t = V_0^t + u^t(t^t - t_0^t), \quad (3.7)$$

where V_0^s and V_0^t are the positions of the SARC and TC2 drift chamber sense wire in the V coordinate system, u^t (u^s), t^t (t^s), t_0^t (t_0^s) are the TC2 (SARC) drift velocity, drift time and start times respectively. The tracks are reconstructed by an extrapolation from the V coordinate to the interaction point. The average of the track's V coordinates on the front face of the tube chambers, as determined by the SARCs and TC2s, is compared to that determined by the tube chambers. Any differences between these two values is used in correcting the estimated position of the tube chamber wires.

The 3-Line Plots

These are graphical comparisons of the SARC and TC2 drift times for the same electron track. For a SARC and a TC2, eight such comparisons can be made because of the eight possible wire combinations. Figure 3.9 shows a typical 3-line plot for a SARC and a TC2 wire. The three distinct regions **1**, **2**, **3** correspond to tracks below the wires, between the wires, and above the wires respectively.

Straight lines are fitted to the points in the 3-line plots. The SARC drift time at the intersection of the lines through regions **1** and **2** gives the SARC start time t_0^s . The difference between the SARC drift times at the two intersections gives the SARC drift time corresponding to the known distance between the wires, thus the SARC drift velocity can be obtained. Similarly the TC2 start time t_0^t and the drift velocity in it u^t can be deduced.

The 'Spike and Dropout' Problem of 1991

In 1991, unexpected clumpings of track drift times into 320 ns periodic time bins were observed in the 3-Line plots from some of the drift chambers (Figure 3.10). These clumpings resulted in reduced accuracies on the determined u and t_0 values. The clumps were thought to be produced by spikes and dropouts. Spikes (dropouts) are unusually high (low) digital values entered in memory for a relatively low (high) analogue signal. These were seen in the snapshots of the pulses. About 95% more spikes than dropouts were observed. For this reason, the illustration of the problem and solution will be done using only spikes. The explanation for the spikes and dropouts involved delays in the propagation of some bits of the Random Access Memory (RAM) address for the signals from the digitizer.

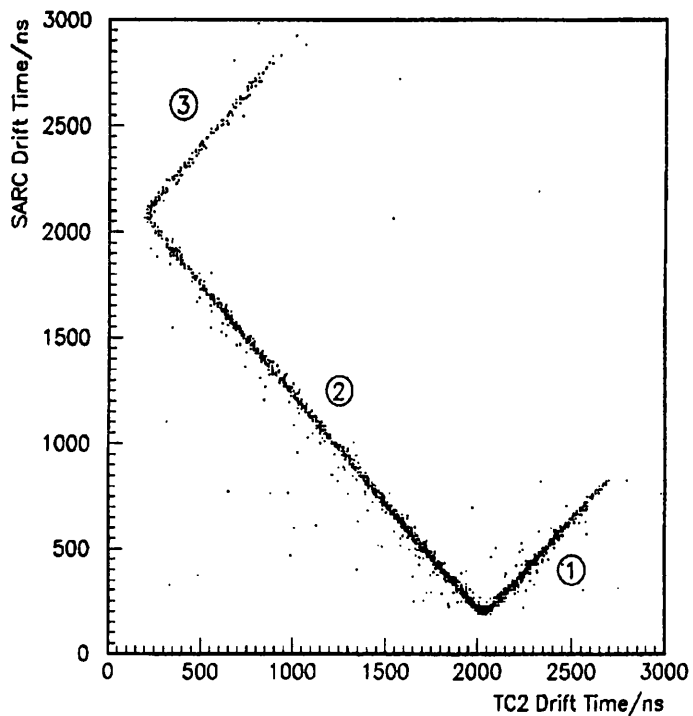


Figure 3.9: A typical 3-line plot. The three distinct regions 1, 2, 3 correspond to tracks below the wires, between the wires, and above the wires respectively.

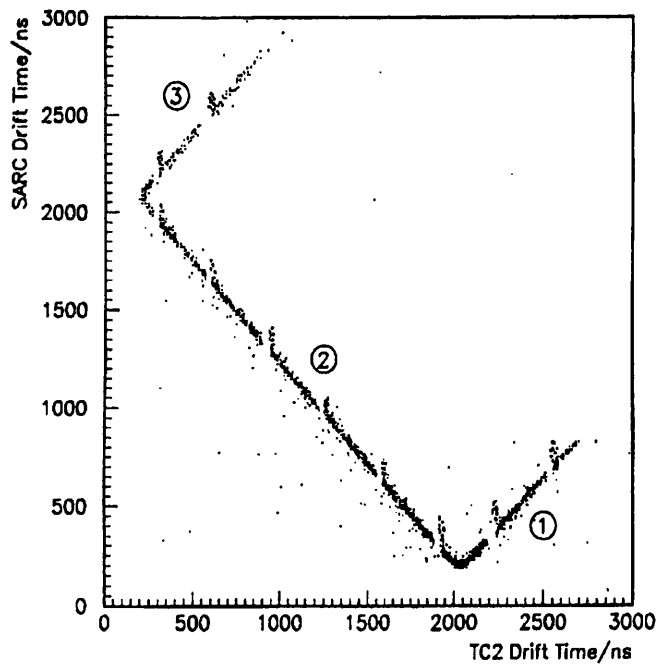


Figure 3.10: A 3-line plot with periodic clumps.

In investigating how the spikes and dropouts affect the drift time calculation, simple simulations were performed by superimposing spikes and dropouts on typical pulses, and then calculating the drift times (Figure 3.11) and by moving a single pulse along a drift time axis in steps of 20 ns and superimposing spikes on any sample position on the rising edge of the pulse which is a multiple of 320 ns (Figure 3.12). The results obtained from that exercise revealed the following:

- Spikes or dropouts appearing on the rising edge of some pulses can cause the pulse to be missed by the ‘Difference of Samples’ algorithm.
- Spikes occurring on the peak sample of a pulse can lead to the over-estimation of the drift time.
- If a spike appears on the pedestal, a drastic under-estimation of the drift time can occur.
- Spikes can cause periodic clumpings.

The actual magnitude of the effects caused by the spike and dropout, and whether these effects appear at all are dependent on the size and shape of the pulse.

A solution to the problem

There was a two-pronged attack at the problem, the first solution involved tuning away the spike production in the hardware¹. As a back-up, a pulse rectification algorithm [36] was written, whose function was to identify spikes and dropouts in drift chamber pulses, remove them and then replace them with a reasonable estimate of the underlying sample value. In view of the online application of the algorithm, the amount of arithmetic computation involved in the process was kept to the barest minimum whilst still maintaining high efficiency. The algorithm worked by

- Labelling as a spike (dropout), a sample which towers over (is dwarfed by) its two nearest neighbours by an optimized threshold of 6 counts.
- In cases where it labels a sample as a spike and recognizes the next sample as a dropout, it de-labels the first as a spike. This is to avoid distorting the pulse shape.
- The labelled spike (dropout) is replaced by the value obtained at the spike (dropout) position if a cubic interpolation is made through the four samples on either side of it.

¹Solving the problem in the hardware was done by Peter Sherwood of the University College London.

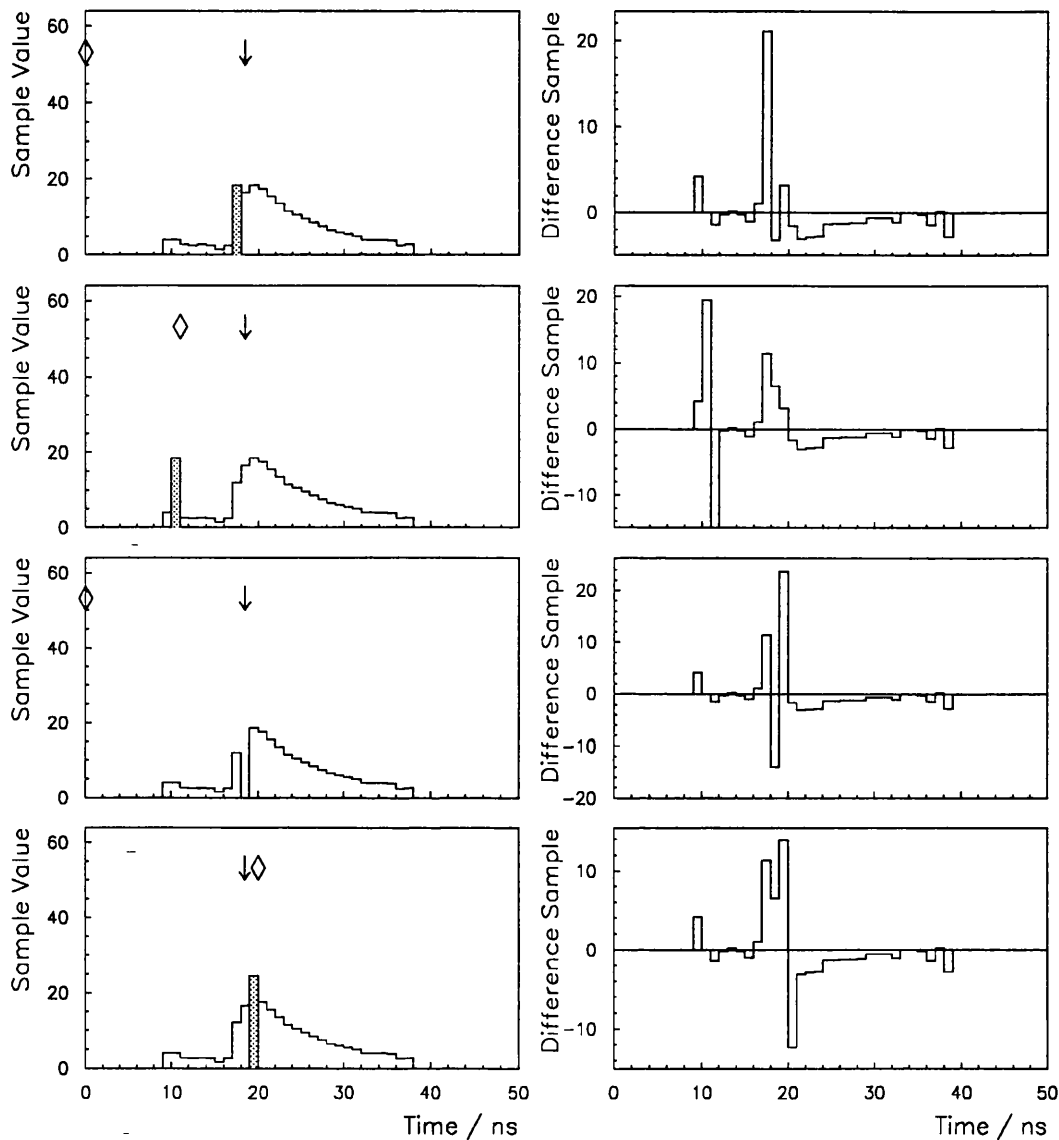


Figure 3.11: The effects of the spikes and dropouts on the drift time calculation. The arrow points to the real drift time whilst the diamond points to the drift times with the spikes or dropouts present. On each row are the pulse and its differentiated pulse. Starting from the top row, (a) The missing of the pulse by the ‘Difference of Samples’ algorithm caused by a spike on the rising edge. (b) The under-estimation of the drift time by a spike appearing on the pedestal. (c) The missing of a pulse caused by a dropout. (d) The over-estimation of the drift time by a spike appearing on the peak sample.

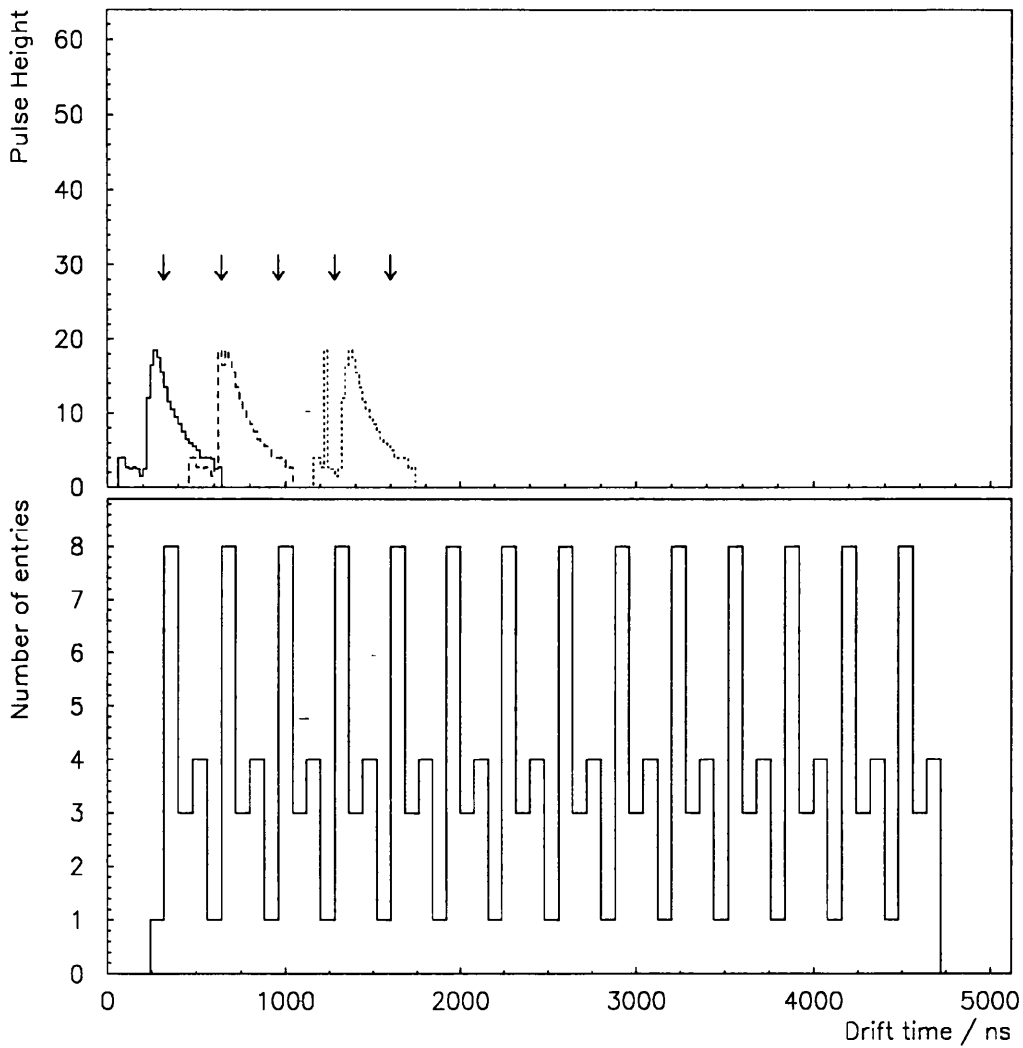


Figure 3.12: The top figure illustrates the simulation of pulses with spikes by moving the pulse from left to right along the drift time axis. The arrows indicate some positions (at multiples of 320 ns) where spikes will be superimposed on the rising edge of the pulses. The bottom histogram is the resulting drift time distribution. The peaking at 320 ns time intervals is evident.

At the time the above algorithm was written, the real data from 1991 was not enough to test the algorithm exhaustively. For this reason, the algorithm was tested on the single pulses of the type shown in Figure 3.12. Figure 3.13 shows a typical comparison of the drift time distributions for un-rectified and rectified artificial pulses. The clumping can be seen to be removed in the rectified data. After implementing the hardware and software solutions to the problem, the 1992 data 3-line plots [55] showed a substantial reduction in the clumping problem.

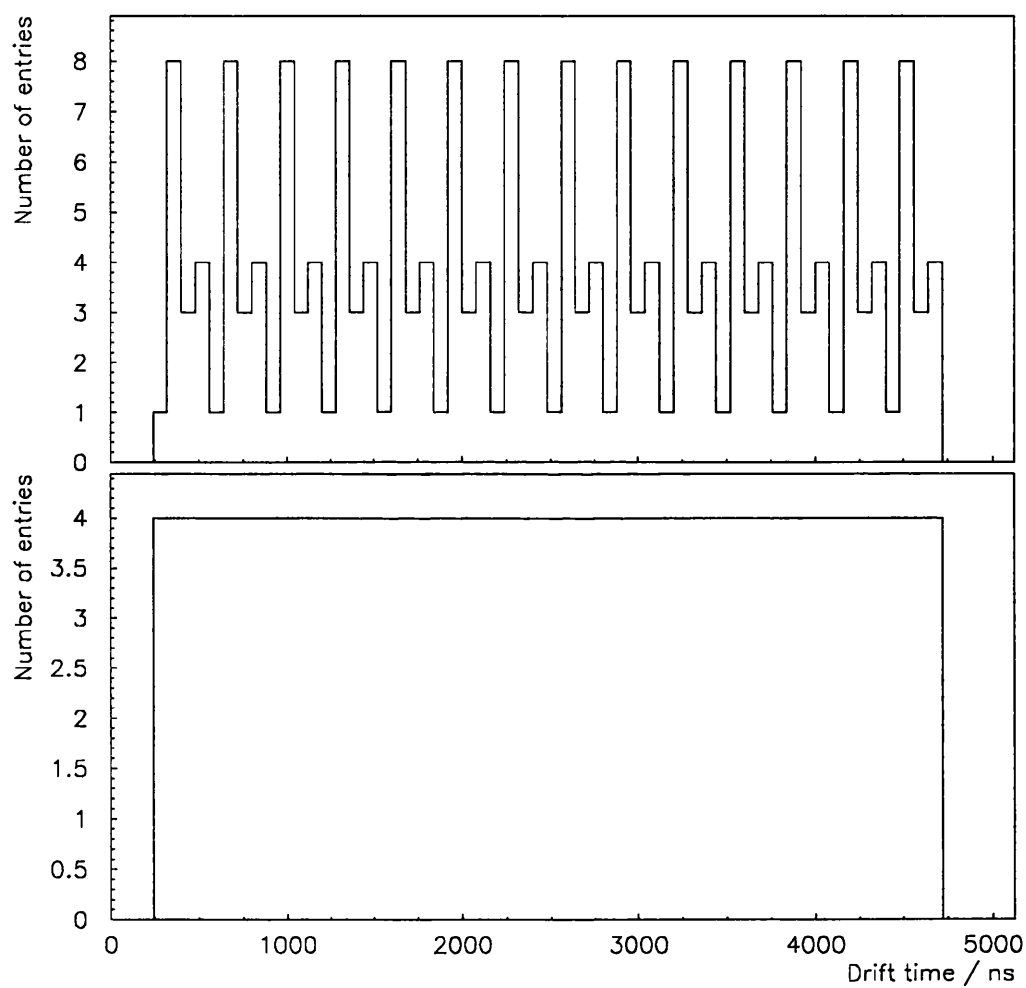


Figure 3.13: A comparison between the drift time distributions for un-rectified (top histogram) and rectified (bottom histogram) pulses.

Chapter 4

Event Cross Section Calculation and Simulations

In this chapter, the calculation of the Higgs production cross section via the Bjorken process is described since this cross section was used in predicting the number of expected Higgs events from a given data sample.

Monte Carlo simulations were vital in our search for the Higgs since they enabled theoretical predictions of event signals to be visualized by a detector simulation program. The programs used in the simulation of the Higgs events and the most important background events (four fermion events) are described.

4.1 Cross Section of $e^+e^- \rightarrow H^0 f \bar{f}$

The calculation of the cross section of the Bjorken process proceeded via the following steps:

- Calculation of the lowest order cross section.
- Calculation of a correction factor that accounts for the contributions from the significant higher order processes.
- Calculation of a radiator function which accounts for initial state photon radiation.
- Convolution of the lowest order cross section with the correction factor and the radiator function, to produce a final cross section.

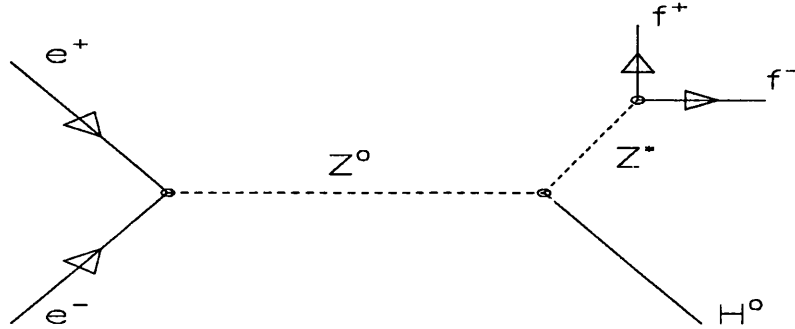


Figure 4.1: The Feynman diagram for the lowest order Bjorken process.

4.1.1 Lowest order cross section

The lowest order Bjorken process is shown in Figure 4.1 where the Z boson (Z^0) radiates a Higgs boson (H^0) to become an off-mass-shell Z boson (Z^*). The mass and momentum of Z^* , M_{Z^*} and P_{Z^*} , respectively, are variable within the kinematic limits set by M_H and M_Z .

The lowest order cross section $\sigma(M_H)$ is given by [37]

$$\frac{d\sigma(M_H)}{dM_{Z^*}^2} = \frac{\Gamma(Z^* \rightarrow f\bar{f})d\sigma(M_{Z^*}, M_H)}{D(M_{Z^*}^2)}, \quad (4.1)$$

where

$$\Gamma(Z^* \rightarrow f\bar{f}) = \frac{M_{Z^*}^2}{48\pi} \beta q^2 \left(\frac{1}{2}(3 - \beta^2)C_V^2 + \beta^2 C_A^2 \right), \quad (4.2)$$

$$q = \frac{e}{\sin \theta_W \cos \theta_W}, \quad (4.3)$$

$$\beta = \sqrt{1 - \frac{4M_f^2}{M_{Z^*}^2}}, \quad (4.4)$$

$$d\sigma(M_{Z^*}, M_H) = \frac{G_{HZZ}^2 C^* F (3M_{Z^*}^2 + F^2)}{24\pi^2 M_{Z^*}^2 \sqrt{s} D(s)}, \quad (4.5)$$

$$G_{HZZ} = \frac{eM_Z}{\sin\theta_W \cos\theta_W}, \quad (4.6)$$

$$D(M^2) = (M^2 - M_Z^2)^2 + \Gamma_Z^2 M_Z^2, \quad (4.7)$$

$$F^2 = \frac{s^2 + M_{Z^*}^4 + M_H^4 - 2(sM_{Z^*}^2 + M_{Z^*}^2 M_H^2 + M_H^2 s)}{4s}, \quad (4.8)$$

$$C^* = C_V^2 + C_A^2. \quad (4.9)$$

G_{HZZ} is the HZZ -vertex coupling constant, β is the velocity of the fermions in the rest frame of Z^* , C_A and C_V are the axial and vector coupling constants [4] of the Z^* to fermions, \sqrt{s} is the centre of mass energy of the colliding electron and positron, $\Gamma(Z^* \rightarrow f\bar{f})$ is the rate of decay of Z^* into the fermions, $D(M_{Z^*}^2)$ and $D(s)$ are the virtual and real Z boson propagator terms respectively. Equation (4.1) then becomes

$$\frac{d\sigma(M_H)}{dM_{Z^*}^2} = \frac{N_c G_{HZZ}^2 q^2 C^* F (3M_{Z^*}^2 + F^2)}{1152\pi^3 \sqrt{s} D(s) D(M_{Z^*}^2)} \beta \left(\frac{1}{2} (3 - \beta^2) C_V^2 + \beta^2 C_A^2 \right), \quad (4.10)$$

where N_c is the color factor, which takes the value of 1 (3) for leptons (quarks). The total cross section calculation is performed numerically and is given by

$$\sigma(M_H) = \int_{(2M_f)^2}^{(\sqrt{s}-M_H)^2} \left(\frac{d\sigma(M_H)}{dM_{Z^*}^2} \right) dM_{Z^*}^2. \quad (4.11)$$

4.1.2 Higher Order Corrections

The most significant higher order contributions are due to the Z^0 propagator self-energy, and vertex processes. The dominant vertex contribution is due to the heavy top quark because of its large coupling to the Higgs (Figure 4.2). The improved cross section $\bar{\sigma}(M_H)$ is evaluated using the Improved Born Approximation (IBA) scheme [9] where the contributions from the higher order processes are evaluated as a multiplicative factor. The improved cross section is given by

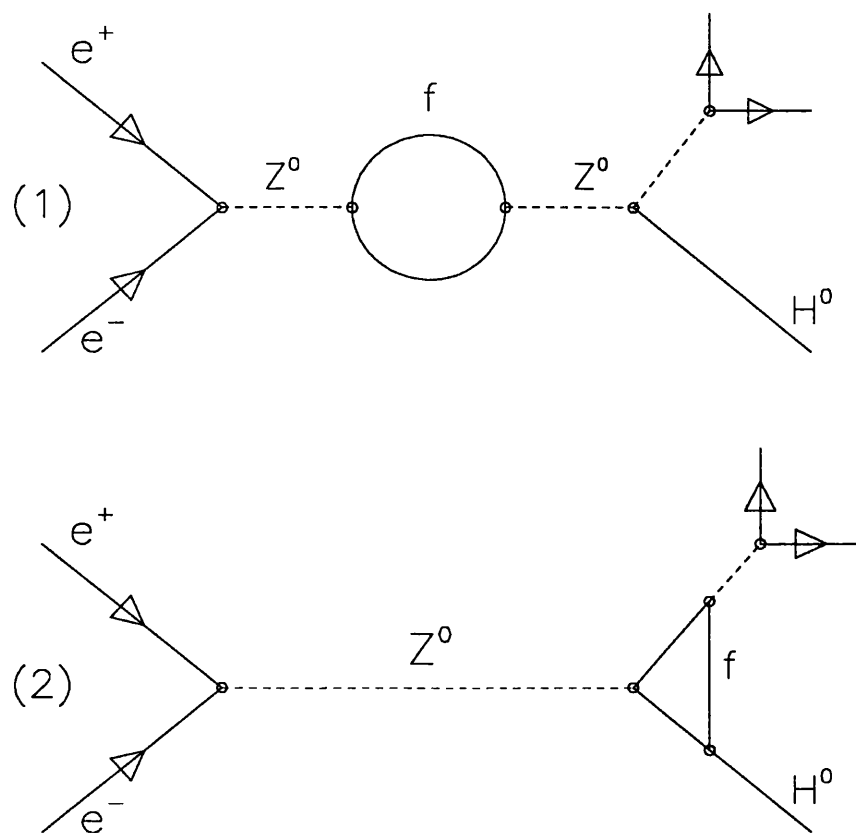


Figure 4.2: The higher order Bjorken processes evaluated in the IBA scheme. Figure (1) is the one loop Z^0 propagator self energy process. Figure (2) is the Z vertex process; the dominant contribution to this process is that due to $f = \text{top quark}$.

$$\bar{\sigma}(M_H) = \sigma(M_H)\left(1 + \frac{1}{3}\Delta\rho\right), \quad (4.12)$$

where

$$\Delta\rho = \frac{3G_F M_t^2}{8\pi^2\sqrt{2}}. \quad (4.13)$$

4.1.3 Corrections due to Bremsstrahlung

Initial State Radiation (ISR) corrections to the Bjorken process account for the contributions due to real and virtual photons (Figure 4.3). To correct $\bar{\sigma}(M_H)$ for the ISR effects, it is convoluted with the radiator function $G(x)$ over the full range of centre of mass energies $\sqrt{s'}$, accessible after bremsstrahlung has occurred. The convoluted cross section is given by [38]

$$\sigma_c(M_H) = \int_{x_0}^1 dx G(x) \bar{\sigma}(M_H, x\sqrt{s}), \quad (4.14)$$

where $x = \sqrt{s'}/s$ and $x_0 = 1 - \sqrt{M_H^2/s}$. $G(x)$ is given by [39]

$$G(x) = \beta(1-x)^{\beta-1}\delta^{V+S} + \delta^H(x), \quad (4.15)$$

where δ^{V+S} which is the contribution from virtual and soft photons, and $\delta^H(x)$ which is the contribution from hard photons, are polynomials in $L = \ln(s/M_e^2)$ and $\beta = (2\alpha/\pi)(L-1)$.

δ^{V+S} is given by [39]

$$\delta^{V+S} = 1 + \delta_1^{V+S} + \delta_2^{V+S}, \quad (4.16)$$

where

$$\delta_1^{V+S} = \frac{\alpha}{\pi} \left(\frac{3}{2}L + 2R(2) - 2 \right) \quad (4.17)$$

and

$$\begin{aligned} \delta_2^{V+S} = & \left(\frac{\alpha}{\pi}\right)^2 \left[\left(\frac{9}{8} - 2R(2)\right)^2 L^2 + \left(-\frac{45}{16} + \frac{11}{2}R(2) + 3R(3)\right) L \right] \\ & - \left(\frac{\alpha}{\pi}\right)^2 \left[\frac{6}{5}R(2)^2 + \frac{9}{2}R(3) + 6R(2)\ln 2 - \frac{3}{8}R(2) - \frac{19}{4} \right]. \end{aligned} \quad (4.18)$$

whilst $\delta^H(x)$ is given by [39]

$$\delta^H(x) = \delta_1^H(x) + \delta_2^H(x), \quad (4.19)$$

where

$$\delta_1^H(x) = \frac{\alpha}{\pi} (1+x)(L-1) \quad (4.20)$$

and

$$\delta_2^H(x) = \frac{1}{2} \left(\frac{\alpha}{\pi}\right)^2 (L-1)^2 [(1+x)(3\ln x - 4\ln(1-x)) - \frac{4}{1-x} \ln x - 5 - x]. \quad (4.21)$$

$R(2)$ and $R(3)$ are Riemann zeta functions [39].

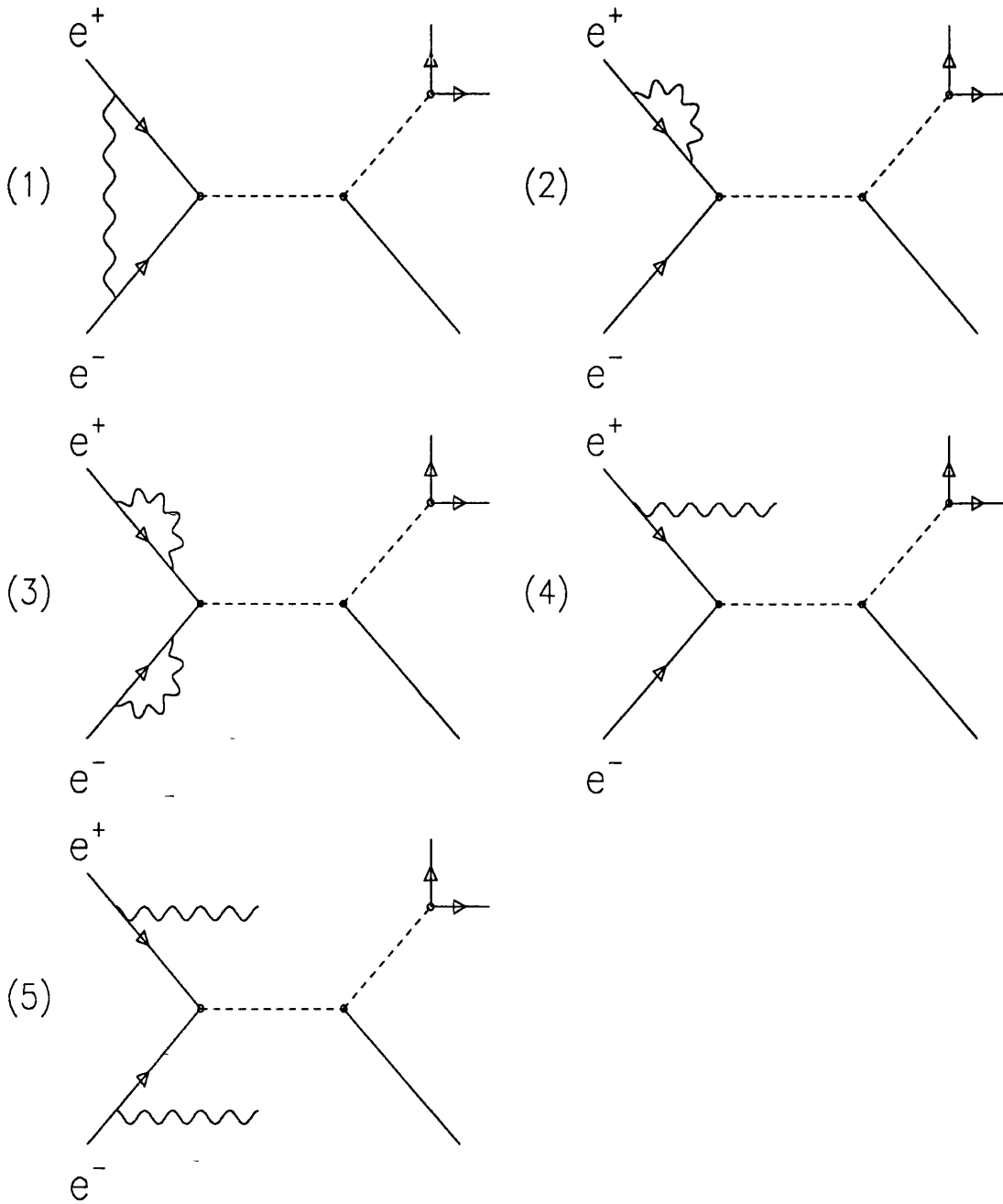


Figure 4.3: QED contributions to the Bjorken process. The intermediate Z boson and the final state particles are not labelled. The wavy lines are the photons. Figures (1), (2) and (3) are the virtual photon processes, (4) and (5) are the soft and hard photon radiation processes.

4.2 The Final Bjorken Cross Sections (Leptonic Channel)

Figure 4.4 shows the dependence of the Bjorken cross section (for $f\bar{f} \equiv e^+e^-, \mu^+\mu^-$) on the centre of mass energy \sqrt{s} for a selection of Higgs masses. The top quark mass was assumed to be 300 GeV in the cross section calculations. The cross sections have two maxima; the first at the centre of mass energy of about 91 GeV due to the peaking of the Z^0 propagator, and the second at an energy value when the production of a Higgs and a real Z^0 in the final state is possible. The cross sections for a Higgs of mass greater than about 60 GeV are greater at higher \sqrt{s} values than they are at 91 GeV; for this reason, the second phase of LEP (LEP-2, where the beam energy will be of the order 90 GeV) is an appropriate collider for the exploration of the higher mass ranges *i.e.* 60 GeV to ~ 91 GeV.

Figure 4.5 shows the dependence of the Bjorken cross section on the mass of the Higgs at $\sqrt{s} = 91$ GeV. It can be seen that the cross section falls as the Higgs mass increases; this is because the Z^* propagator and the phase space available for the decay products of the Z^* , become increasingly small as the Higgs mass increases.

The mass and momentum of Z^* can take on a range of values defined by the kinematic limits set by the masses of H^0 and Z^0 . Using Equation 4.10, it has been shown in [12] that the Z^* mass distribution and the average momentum of the Z^* for a selection of Higgs masses, are as shown in Figures 4.6 and 4.7 respectively.

4.3 Higgs Boson Decay Branching Ratios

The Higgs decay branching ratios were needed in order to calculate the probability of having a particular H^0 and Z^* decay combination. At the tree level, the decay rate of the Higgs to fermions is given by

$$\Gamma(H^0 \rightarrow f\bar{f}) = \frac{N_c G_F M_H M_f^2 \beta_f^3}{4\pi\sqrt{2}} \quad (4.22)$$

and the branching ratios are given by

$$B(H^0 \rightarrow f\bar{f}) = \frac{N_c M_f^2 \beta_f^3}{\sum_f N_c M_f^2 \beta_f^3}, \quad (4.23)$$

where all the variables have their usual meanings. These tree level branching ratios are subject to QCD corrections.

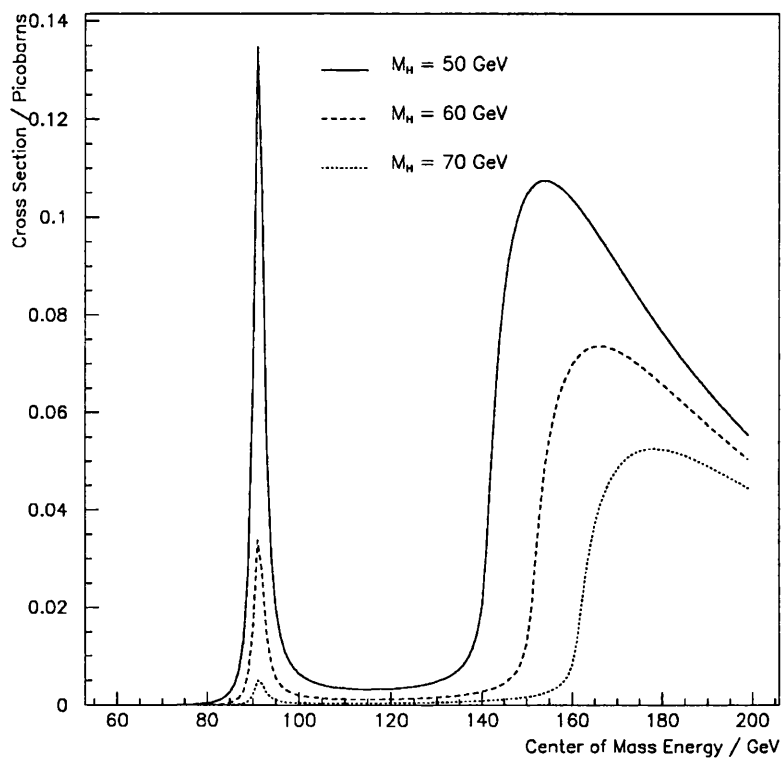


Figure 4.4: The Bjorken cross section (leptonic channel) vs the centre of mass energy for Higgs of mass 50, 60 and 70 GeV.

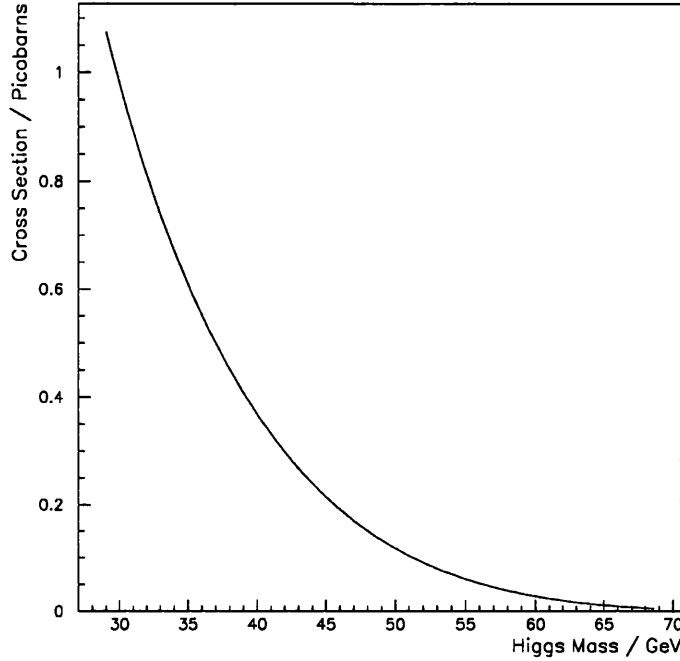


Figure 4.5: The Bjorken cross section (leptonic channel) at center of mass energy of 91 GeV, \forall the Higgs mass.

4.3.1 QCD Corrections

These corrections arise from the fact that quark masses $M_q(\mu)$ and the strong coupling constant $\alpha_s(\mu)$ depend on the energy scale μ . The QCD-corrected Higgs decay rates to quarks have been calculated in reference [40] and are given by

$$\begin{aligned} \Gamma(H^0 \rightarrow q\bar{q}) = & \frac{3G_F M_H M_q^2}{4\pi\sqrt{2}} \left[\left(1 - 4\frac{M_q^2}{M_H^2}\right)^{3/2} + \frac{\alpha_s}{\pi} \left(\frac{17}{3} - 40\frac{M_q^2}{M_H^2} + O\left(\frac{M_q^4}{M_H^4}\right)\right) \right. \\ & \left. + \left(\frac{\alpha_s}{\pi}\right)^2 \left(K_S + O\left(\frac{M_q^2}{M_H^2}\right)\right) + O\left(\left(\frac{\alpha_s}{\pi}\right)^3\right) \right], \end{aligned} \quad (4.24)$$

where $\alpha_s(\mu)$ and $M_q(\mu)$ were evaluated at $\mu = M_H$. $K_S \simeq 35.9399 - 1.3586n_f$ [40], where n_f is the number of quark flavours that the Higgs can kinematically decay into. The decay branching ratios of the Higgs to quarks as obtained from reference [40] are in Table 4.1.

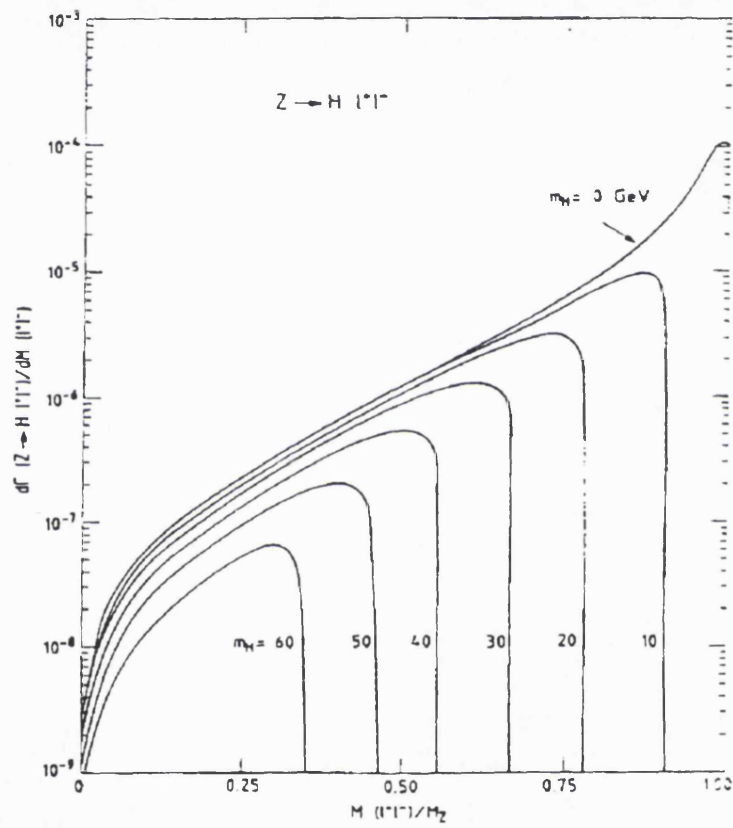


Figure 4.6: The Z^* mass ($M(l^+l^-)$) distribution for a selection of M_H values.

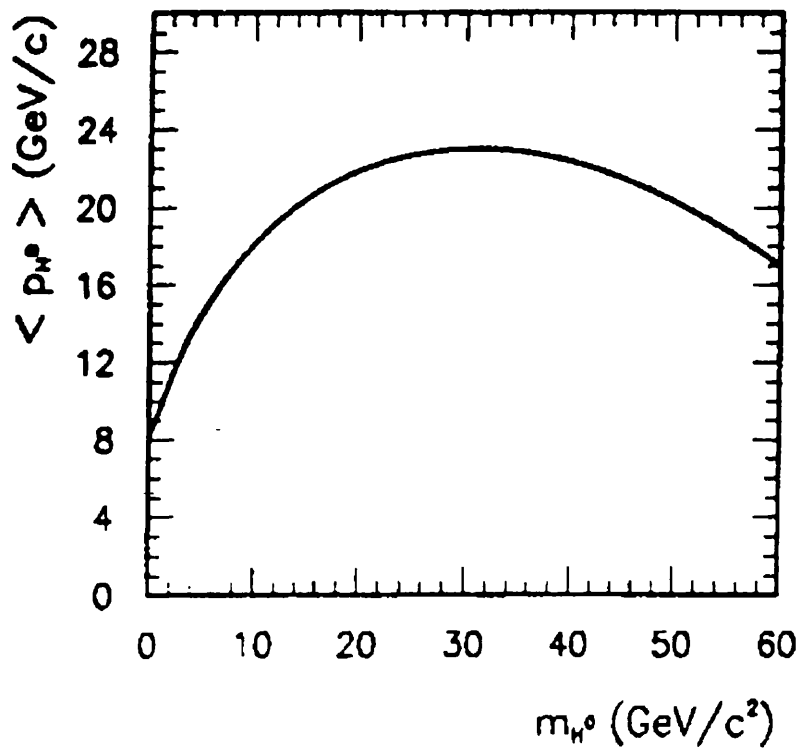


Figure 4.7: The average momentum of Z^* , for a range of Higgs masses.

4.4 Simulation of Higgs Events

The simulation of Higgs events took the form of an initial event generation followed by a detector response simulation. The generation of Higgs events was done using the H0Z0 program [41]. This program was designed to generate only single initial state radiative (ISR) events such as $e^+ e^- \rightarrow H^0 Z^* \gamma$ with $H^0 \rightarrow q \bar{q}$ and $Z^* \rightarrow f \bar{f}$.

[40]

Table 4.1: Decay branching ratios (in %) of the Higgs to fermions.

M_H	$\bar{b} b$	$\tau^+ \tau^-$	$\bar{c} c$	Other decays
50	88.3	8.7	2.8	0.2
60	87.9	9.0	2.8	0.3
70	87.6	9.2	2.8	0.4
80	87.1	9.5	2.8	0.6

4.4.1 The Generation Process

The first step in the generation process is the calculation and histogramming of the hard ISR energy spectrum $d\sigma_B/dk$. This spectrum is given by [38]

$$\frac{d\sigma_B}{dk} = \frac{\alpha}{\pi} \left(\ln \frac{s}{m_e^2} - 1 \right) \frac{1 + (1-k)^2}{K} \sigma_0(s(1-k)), \quad (4.25)$$

where σ_B is the Bjorken production cross section with ISR taken into account, σ_0 is the cross section of the non-radiative process evaluated at a the centre of mass energy after ISR has occurred, whilst k is the fractional energy of the ISR. The histogram of the energy spectrum is formed such that one has narrower histogram bins the higher the $d\sigma_B/dk$ values, so that all the bins have approximately the same number of entries thus enabling a fast generation of events. The histogram is formed for k values satisfying

$$\frac{2E_c}{\sqrt{s}} \leq k \leq 1 - \frac{(M_H + 2M_f)}{\sqrt{s}}. \quad (4.26)$$

E_c is the critical energy value above (below) which the ISR is considered as being hard (soft). E_c is given by [38]

$$E_c = \frac{1}{\sqrt{2}} \exp \left[- \frac{\pi/2\alpha + 3/4 \ln(s/M_e^2) + 1/6\pi^2 - 1}{\ln(s/M_e^2) - 1} \right]. \quad (4.27)$$

The second step involves generating the energy of an initial state photon from the ISR histogram, after which its directional variables are generated. The photon's azimuthal direction is generated uniformly whilst its polar angular direction is generated using a certain mapping and rejection criteria, details of which can be found in reference [41].

The third step in the generation process involves generating the four-vectors of the Higgs and those of the decay products of Z^* , for a fixed value of centre of mass energy corresponding to that after ISR has occurred. To do this, the directions of H^0 and Z^* are generated in the rest frame of the Z^0 (n.b. the Z^0 direction is opposite to that of the ISR) and are required to pass certain rejection criteria [41]; the ratio of the Higgs energy to the centre of mass energy $x = q_H^0/\sqrt{s}$ is then generated using the mapping (Equation (4.28)) and rejection criteria (Equation (4.29)) given below (see reference [41] for full details).

$$x = x_p + b \tan \left[\rho_1 \arctan \left(\frac{x_2 - x_p}{b} \right) + (1 - \rho_1) \arctan \left(\frac{x_1 - x_p}{b} \right), \right] \quad (4.28)$$

$$w_1 = \frac{[12 + 2a - 12x + x^2]\sqrt{x^2 - a}}{[12 + 2a - 12x_p + x_p^2]\sqrt{x^2 - a}} < N\rho_2, \quad (4.29)$$

where

$$a = \frac{4M_H^2}{s}, \quad b = \frac{M_Z\Gamma_Z}{s}, \quad x_p = 1 + \frac{M_H^2 - M_Z^2}{s}, \quad x_1 = \sqrt{a}, \quad x_2 = 1 + \frac{1}{4}a. \quad (4.30)$$

$N(= 3)$ is an empirically determined number, whilst ρ_1 and ρ_2 are uniformly generated random numbers between 0 and 1.

From the generated fractional energy of H^0 , the energy of Z^* is computed. The fermions f and \bar{f} are generated isotropically in the Z^* rest frame according to some rejection criteria [41]. The decay branching ratios of H^0 are used to decide on the specific decay product of the H^0 . The Higgs decay is then performed isotropically in its rest frame.

In the final stage of the generation process, all the four-vectors of the generated decay products are boosted into the laboratory frame and subsequently fed into the *JETSET* [58] Monte Carlo program which performs quark hadronisation using the LUND string model, if the decay particles are quarks.

[42]

Finally, the four-vectors of the final particles are fed into the OPAL detector simulation program GOPAL [43], for the final stage of the event simulation.

4.5 Simulation of Four Fermion Events

Four fermion final state events are potential backgrounds to Higgs searches since events of the type $e^+e^- \rightarrow q\bar{q} f\bar{f}$ can have a similar event topology to $e^+e^- \rightarrow Z^0 \rightarrow H f\bar{f}$ when the invariant mass of the $q\bar{q}$ system is very close to that of the Higgs. At the present LEP energies, there are eight possible processes that can result in four fermion final states (Figure 4.8). These processes can be classified into four groups namely, the annihilation, bremsstrahlung conversion and the multi-peripheral processes. These events were generated using the FERMISV program [44] and the generated four-vectors were fed into the LUND Monte Carlo program in order for the quarks to be fragmented and hadronized. The final four-vectors were then fed into the OPAL detector simulation program for the final event simulation. Figure 4.9 shows the comparison between the Bjorken cross section (leptonic channel) and the four fermion cross section as a function of the invariant mass of the $q\bar{q}$ system; the four-fermion cross section is comparable to the Bjorken cross section for hadronic mass greater than 55 GeV.

Multi-hadronic events were generated using the HERWIG program [47].

4.6 GOPAL – The OPAL Simulation Program

The simulation of the response of OPAL to the generated particles (four-vectors) was done using the GOPAL program [43]. GOPAL is based on a package of programs called GEANT [45]; GEANT allows its user to describe an experimental set-up and to control the transport of particles through the various devices of the set up. GOPAL records the simulated responses to the *traversal* of the particles. The responses to a generated event are then passed through the OPAL event reconstruction program ROPE [46] for event reconstruction.

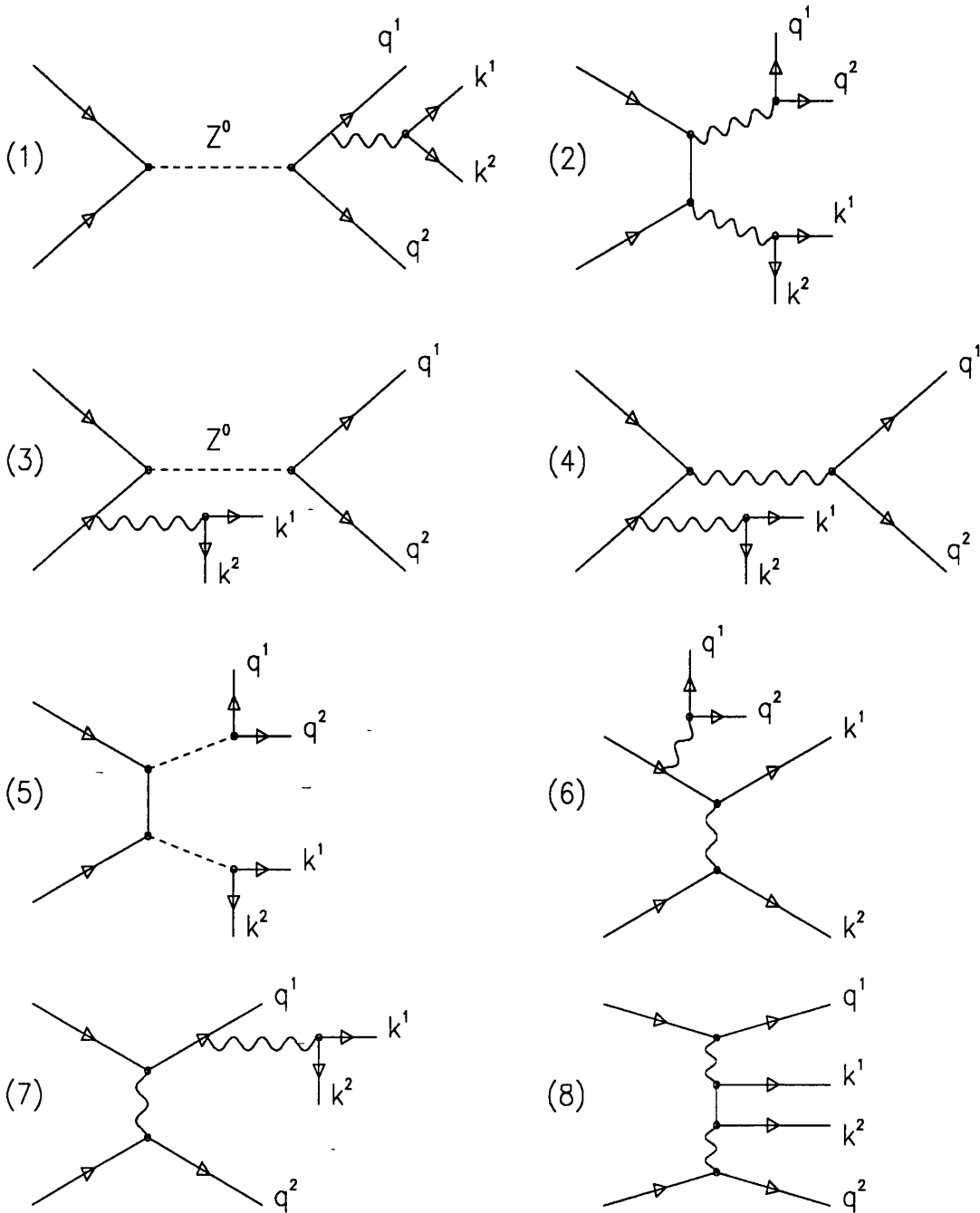


Figure 4.8: Four fermion final states. Only the final state four-vectors and the Z propagators are labelled. The wavy lines denote photon propagators. Figure (1) is the annihilation process, (2) (3) (4) and (5) are the conversion processes, (6) and (7) are the bremsstrahlung processes and (8) is the multi-peripheral process.

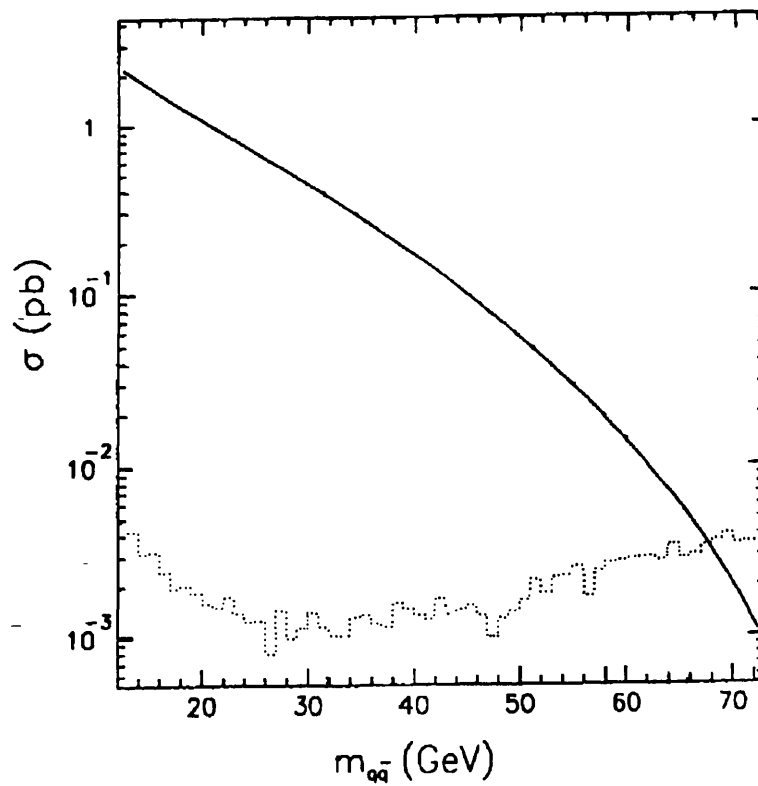


Figure 4.9: A plot of Bjorken cross section (leptonic channel) – solid curve – and the four-fermion cross section – dotted curve – versus the hadronic mass at centre of mass energy 91 GeV. A logarithmic scale is used for the cross section axis. The four fermion cross sections are for events of the type $l^+l^-q\bar{q}$ where l denotes electrons and muons.

Chapter 5

THE SEARCH ALGORITHM

In this chapter a detailed description of the search for the Higgs through the leptonic channel – one of the two decay channels exploited – is given. The search algorithm was based on that for previous OPAL searches [53], which involved looking for an energetic and isolated lepton pair (e^+e^- or $\mu^+\mu^-$) recoiling against a hadronic system (Figure 5.2). The backgrounds to the signal were expected to be from hadronic Z^0 decays, and four-fermion events.

The search algorithm (Figure 5.1) was divided into three stages namely:

- The event trigger, and data taking stage.
- The event filter stage.
- The main analysis.

The search through the neutrino channel will also be described briefly at the end of the chapter since the final Higgs mass limit depended on the results from both channels.

5.1 The Event Trigger

In this stage, all potential events originating from e^+e^- collisions were recorded whilst eliminating beam-gas, beam-wall, and cosmic ray events. The efficiency for the detection of multihadronic events by the event trigger has been estimated to be greater than 99.9% [32]. The event trigger was activated if any of the following conditions were satisfied:

- Electromagnetic energy in the barrel > 6 GeV.

- Electromagnetic energy in the barrel > 4 GeV and one track in barrel.
- Electromagnetic energy in the barrel > 4 GeV and one time-of-flight ϕ sector hit.
- Electromagnetic energy in either endcap > 10 GeV.
- Electromagnetic energy in one endcap > 6 GeV and at least one track on the other side.
- Electromagnetic energy in both left and right endcaps > 10 GeV.
- Electromagnetic energy in barrel > 4 GeV and > 6 GeV in one endcap.
- 2 barrel tracks.
- 3 tracks.
- ≥ 6 time-of-flight ϕ sector hits.
- 2 collinear time-of-flight ϕ sector hits.
- 2 collinear tracks.
- ≥ 1 track and θ - ϕ correlated time-of-flight hit.

5.2 The Event Filter

The event filter selected events containing at least 6 tracks originating from the interaction region, since Higgs events in the search region ($M_H > 50$ GeV) were expected to have high charged track multiplicities. A track was defined as being ‘good’ (*i.e* originating from the interaction region) if it satisfied the following conditions:

- The distance of closest approach to the interaction point in the r - ϕ plane (d_0) was at most 2.5 cm.
- The distance of closest approach to the interaction point along the beam direction (z_0) was at most 50.0 cm.
- The transverse momentum with respect to the beam axis (p_t) was greater than 0.10 GeV.
- The polar angle with respect to the beam axis (θ) satisfied $|\cos \theta| \leq 0.966$.
- The number of jet chamber wire hits was at least 20 and is more than half the maximum number of hits possible at its polar angle.

OUTLINE OF THE SEARCH ALGORITHM

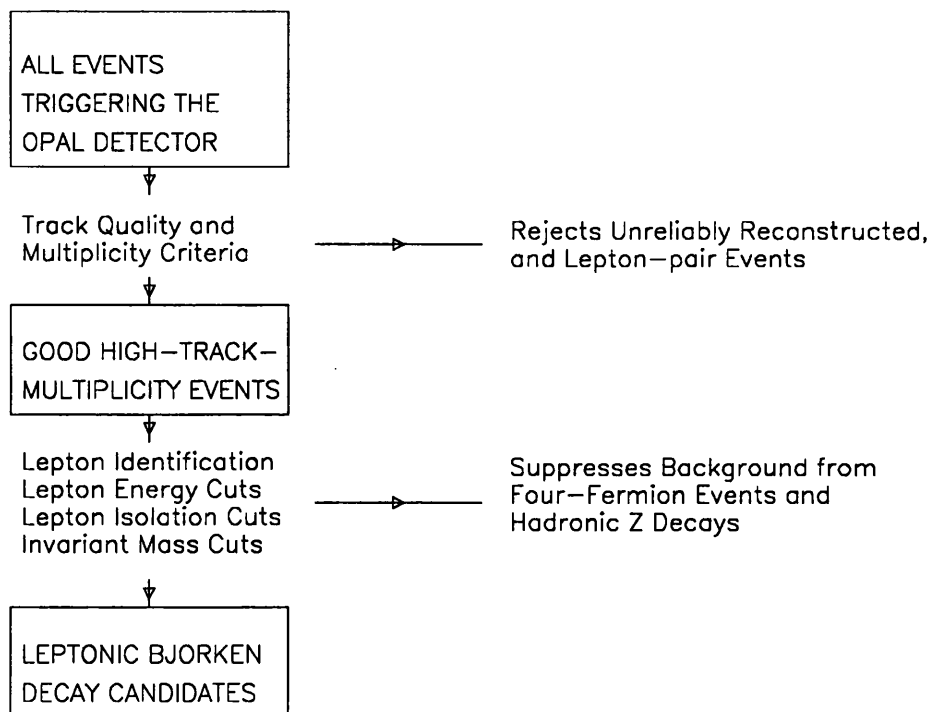


Figure 5.1: A flow chart of the search for the Bjorken signal through the leptonic channel, indicating in the boxes, the types of events remaining after successive group of cuts have been applied.

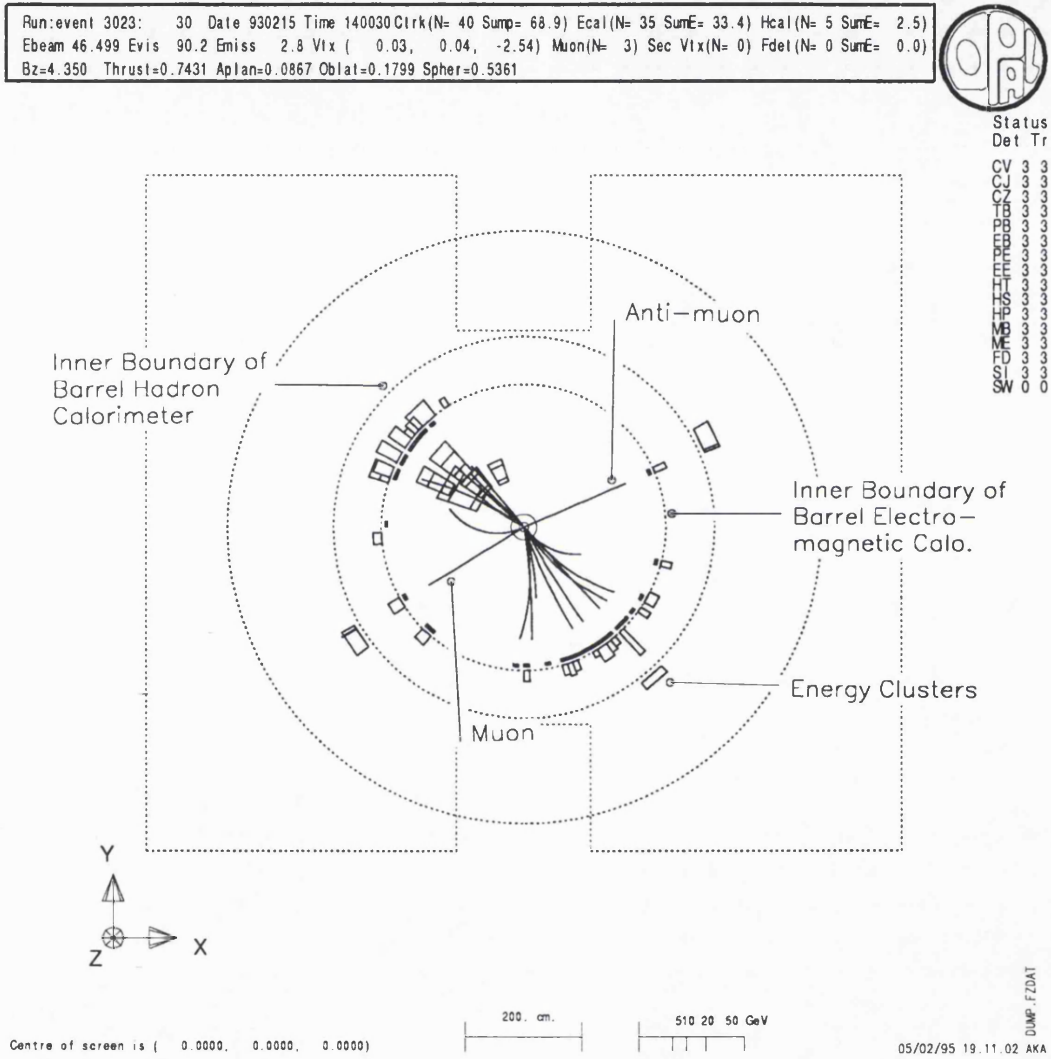


Figure 5.2: A labelled reconstruction of an expected Higgs signal of mass 52 GeV in the leptonic channel.

An electromagnetic cluster was labelled as being ‘good’ if it satisfied the following criteria:

- The cluster energy must be greater than 0.17 GeV if it was in the barrel region.
- The cluster energy must be greater than 0.25 GeV and must contain at least two lead-glass blocks if it was in the end-cap region.

The electromagnetic cluster quality cuts ensured that we were not sensitive to electromagnetic calorimeter noise [53]. The lower cut value in the barrel region is a reflection of the fact that the noise level was lower in the barrel region than in the end-cap. No quality cuts were imposed on the hadronic clusters because of the relatively poor energy resolution of the hadron calorimeter.

5.3 The Main Selection

The main analysis was performed using ‘good’ tracks and electromagnetic clusters. In the preliminary stage of this analysis, the lepton-pair candidates in an event were tagged. These lepton-pair candidates were required to pass very basic requirements namely: The tracks should

- have opposite charge.
- each have an associated electromagnetic cluster or at least two hits in the hadron calorimeter or the muon chamber.

If more than one lepton pair candidate was found in an event, the pair with the smallest sum of momenta (excluding the pair’s momenta) and electromagnetic cluster energies (excluding the clusters associated to the pair) in 30° cones centered on the tracks was chosen. The above preliminary stage was required for data monitoring purposes (see Section 6.1.1).

In the next stage of the analysis, the lepton pairs were identified; isolation and momentum requirements were imposed on them to suppress background from hadronic Z^0 decays and invariant mass cuts were applied in order to reduce the background from four-fermion events.

5.3.1 Lepton Pair Identification

The identification of electron pairs made use of their following properties: Electrons have a unique value of ionization per unit length at low momenta (Figure 5.3)

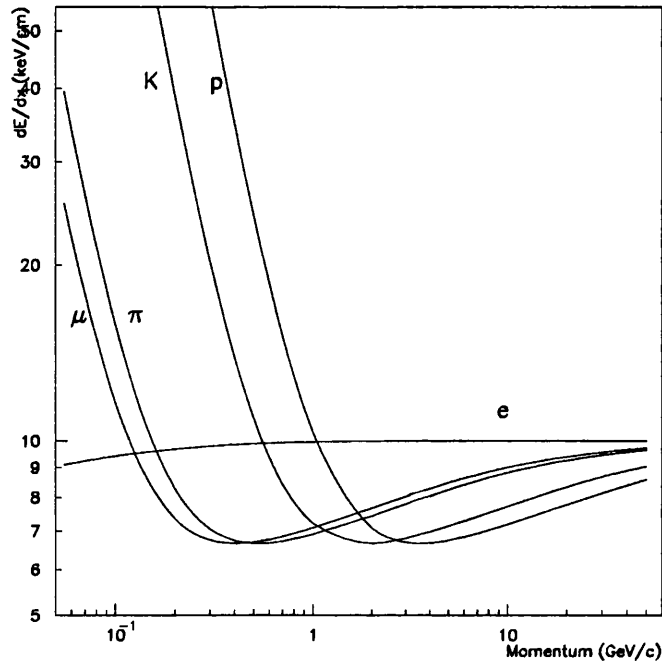


Figure 5.3: dE/dx curves for muons, charged pions, charged kaons, protons, and electrons in the OPAL jet chamber.

and typically deposit all their energy in narrow clusters since the thickness of the electromagnetic calorimeter is sufficient to contain the electromagnetic showers. A track pair were identified as an electron pair if

- the tracks had opposite charge.
- each track was associated to a cluster in the electromagnetic calorimeter to within 20 mrad.
- 90% of the energy in each of the two clusters, was contained in less than 5 lead-glass blocks.
- any cluster in the hadron calorimeter associated with each track, was less than 4 GeV.
- the rate of ionisation (dE/dx) for each of the tracks with momentum less than 15 GeV, was greater than 9.17 keV/cm.
- for each track satisfying $|\cos \theta| < 0.72$ or $|\cos \theta| > 0.84$, the ratio of cluster energy to track momentum (E/p) exceeded 0.7. The cut was not applied in the region $0.72 \leq |\cos \theta| \leq 0.84$ (*i.e.* the overlap region) where the presence of extra material degrades the energy measurement.

Muons deposit little energy in the electromagnetic calorimeter, and depending on their momentum, can travel as far as the last layers of the hadron calorimeter or the muon chambers. A track pair was identified as a muon pair if

- the tracks had opposite charge.
- at least one track had two or more hits in the last five layers of the hadron calorimeter, or two or more hits in the surrounding muon chambers.
- each track was identified as at least a ‘bronze hadron calorimeter’ muon by the inclusive muon identification procedure [49]. Briefly, in this procedure, a track is called a ‘bronze hadron calorimeter’ muon if its angles are fitted onto those of a hadron calorimeter track segment which has more than 5 hits, with the fit $\chi^2 < 20$. A track is called a ‘bronze muon chamber’ muon if its angles are fitted onto those of a muon chamber track segment with a fit $\chi^2 < 20$.
- the energy in the electromagnetic calorimeter associated to both tracks was less than 4 GeV.

The single lepton identification efficiencies obtained using the above procedure are presented and discussed in Section 5.4.

5.3.2 Common Cuts

The events were subjected to the following cuts common to the electron and muon channel analyses.

- Each lepton was required to have a momentum greater than 5.0 GeV and scalar sum of the momenta of the lepton pair, greater than 25.0 GeV. Since leptons produced by the semi-leptonic decay of hadrons are usually not very energetic, the above requirements suppressed hadronic Z^0 decay events. The cuts can be seen to have little effect on the signal leptons (Figure 5.4).
- Each lepton was required to have its polar angle, satisfying $|\cos \theta| \leq 0.92$. This requirement ensured that the track was not close to the beam pipe, thus enabling reliable isolation tests to be performed.
- The event was required to have more than four tracks excluding those within 15° of the lepton tracks.
- The event was required to have more than five clusters in the electromagnetic calorimeter. This requirement together with the preceding one, essentially removed all $Z^0 \rightarrow \tau^+ \tau^-$ events.

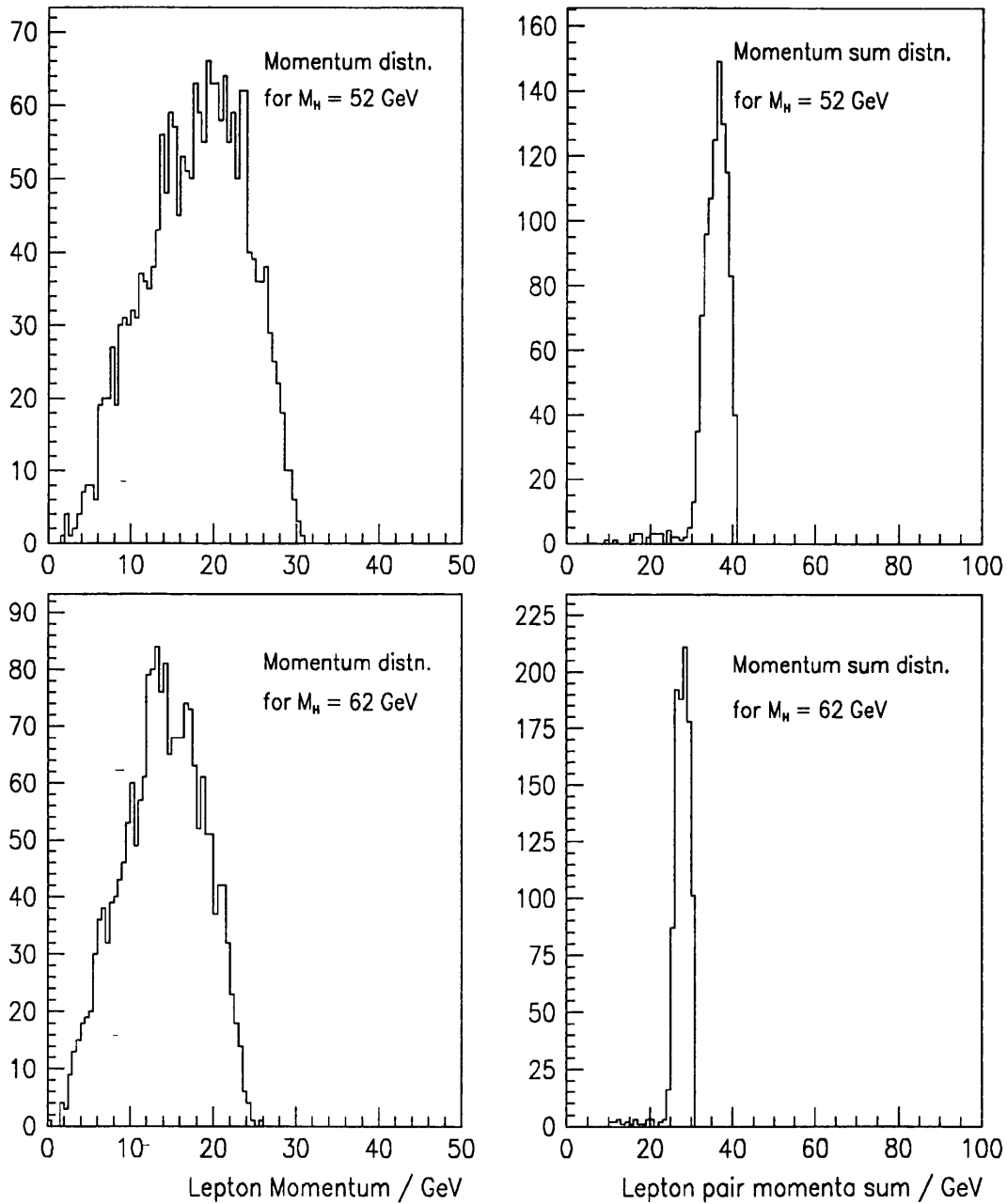


Figure 5.4: A comparison between the lepton momentum and momentum sum spectra for some Higgs events. The entries in the histograms, correspond to a luminosity of 12500 (40000) pb^{-1} for the 52 (62) GeV Higgs signal.

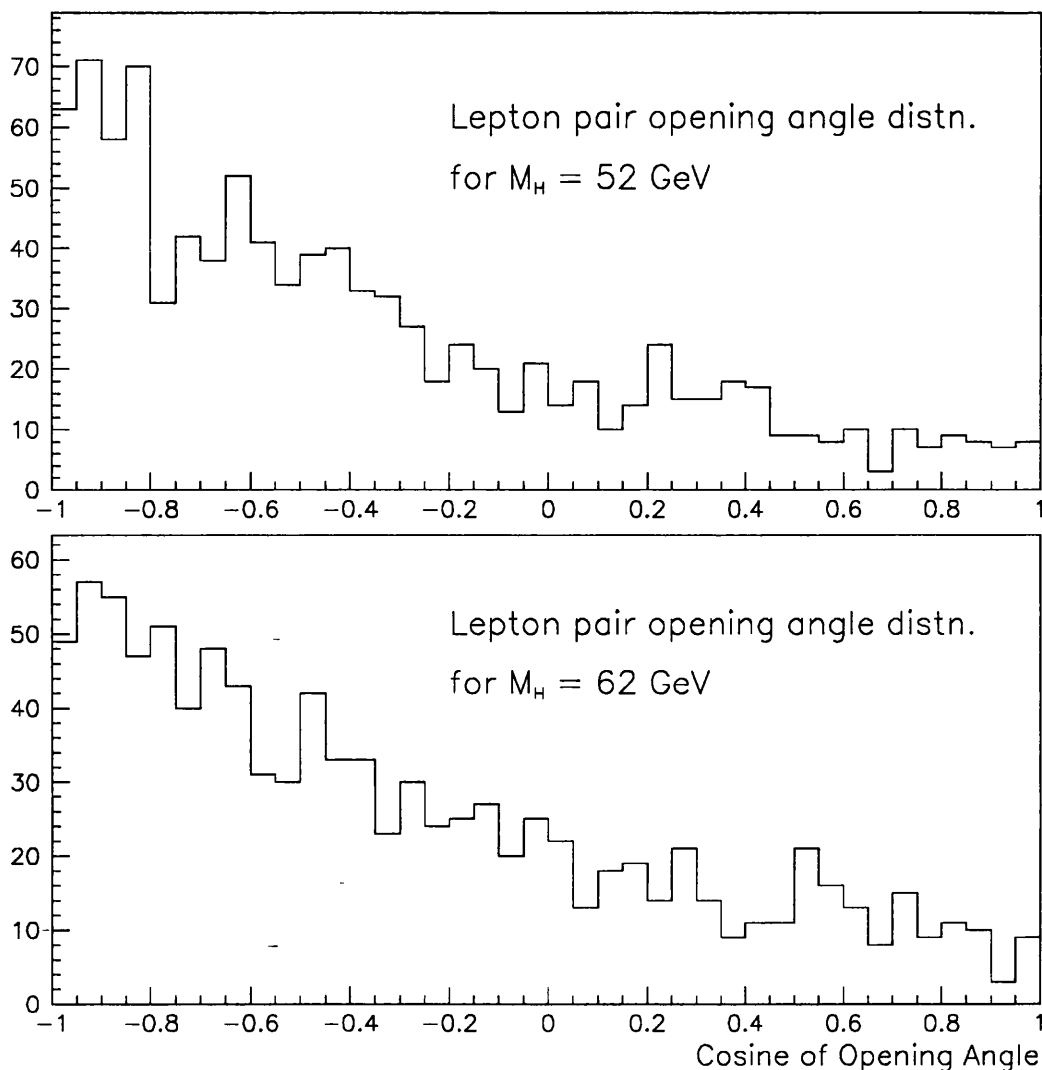


Figure 5.5: A comparison between the lepton pair opening angles for some Higgs events. The entries in the histograms, correspond to a luminosity of 12500 (40000) pb^{-1} for the 52 (62) GeV Higgs signal.

- The opening angle between the lepton pair must be greater than 30° . This requirement was designed to eliminate pair-produced leptons. The cut was expected to have a minimal effect on the lepton pairs from Higgs events (Figure 5.5).
- The event was required to have less than 2.0 GeV deposited in the forward detectors. This requirement rejected Higgs events in which a reliable estimate of the hadronic mass (see later) is unobtainable because of energy loss down the beam pipe. The requirement also rejected two-photon events.

5.3.3 Lepton Pair Isolation Cuts

The lepton pair isolation cuts were expected to remove all the background from $Z^0 \rightarrow q\bar{q}$ events which contained at least two oppositely charged leptons produced by semi-leptonic decays of heavy flavoured hadrons, since the leptons are embedded in the hadronic jets in these types of events. Three groups of isolation cuts were imposed.

In the first group of cuts, the fraction of the total sum of scalar momentum – excluding those of the lepton pair – in a cone of half-angle 30° centered on each lepton was required to be less than 0.2. The procedure was repeated using the electromagnetic clusters instead of the momenta of the charged tracks. These isolation cuts were called the P3030 and E3030 cuts respectively. These cuts had a high probability of selecting Higgs events for which the angle between the lepton pair and the Z^* flight direction in the Z^* rest frame was close to 90° (Figure 5.6).

If the highest momentum lepton track had momentum greater than 20 GeV, the P4515 and E4515 cuts were applied instead of the P3030 and E3030. Here, the previous isolation test was repeated using a cone of 45° centered on the higher momentum lepton track, and a cone of 15° centered on the lower momentum track. These tests had a high probability of identifying Higgs events for which the angle between the lepton pair and the Z^* flight direction in the Z^* rest frame was close to 0° (Figure 5.6).

In the third isolation cut (B2 cut), the sum of the scalar momenta of tracks within 15° of each lepton was required to be less than 1 GeV. This cut was intended to reject $Z^0 \rightarrow q\bar{q}$ events where the leptons were produced in the decays of isolated hadrons.

Higgs candidate events were required to pass the B2 cut, and P3030 and E3030 (or P4515 and E4515). The isolation fractions for the lepton pairs from $Z^0 \rightarrow q\bar{q}$ events, and simulated Higgs events are compared in Figure 5.7.

Hadronic and Lepton Pair Mass Calculations, and Cuts

The mass of the hadronic system was determined in two independent ways. The first method involved using energy and momentum conservation to calculate the mass of the hadronic system (M_{recoil}) recoiling against the lepton pair. Ignoring the masses of the leptons, the recoil mass is given by

$$M_{recoil}^2 = s - 2\sqrt{s}(E_1 + E_2) + 2E_1E_2(1 - \cos\theta) \quad (5.1)$$

where E_1 and E_2 are the momenta (cluster energies) of the muon (electron) pair, and θ is the opening angle between them. The cluster energies were used in computing

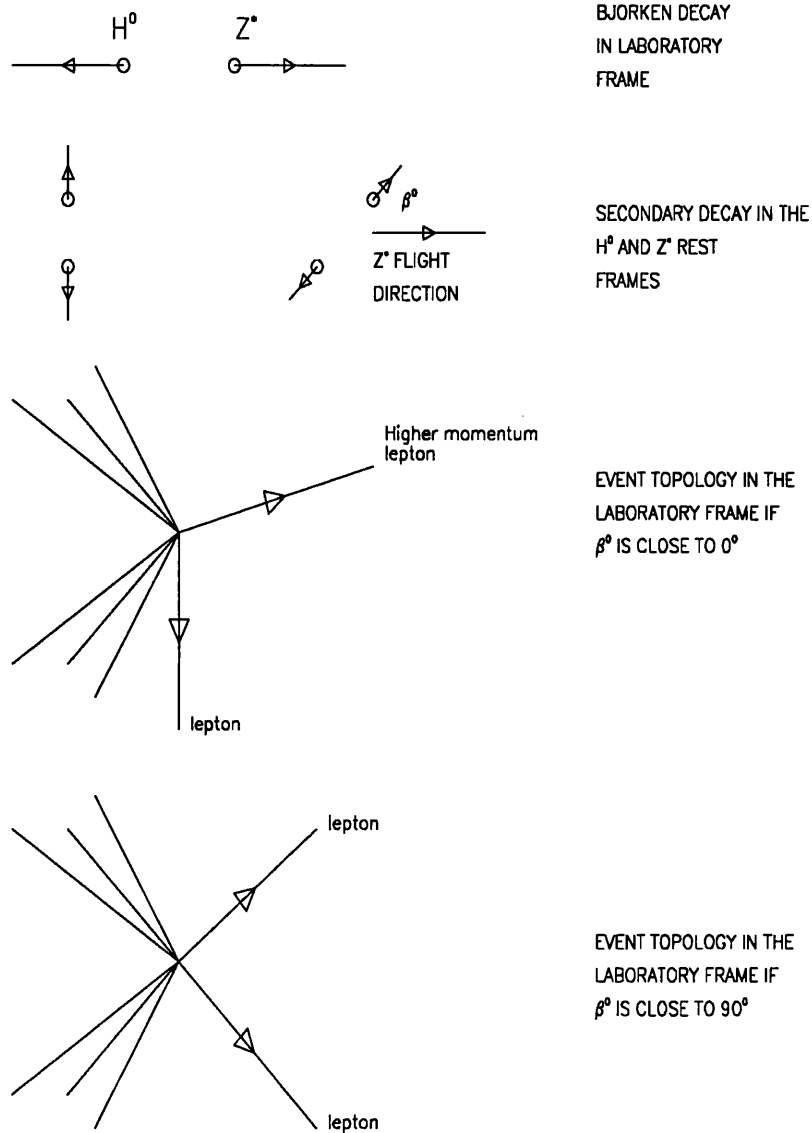


Figure 5.6: Schematic diagram showing a special case of the Bjorken process where the angle between the direction of the H^0 decay products and the H^0 flight direction is almost 90° . The diagram illustrates the reasons for the P3030, E3030 and the P4515, E4515 isolation cuts (see section on lepton isolation cuts).

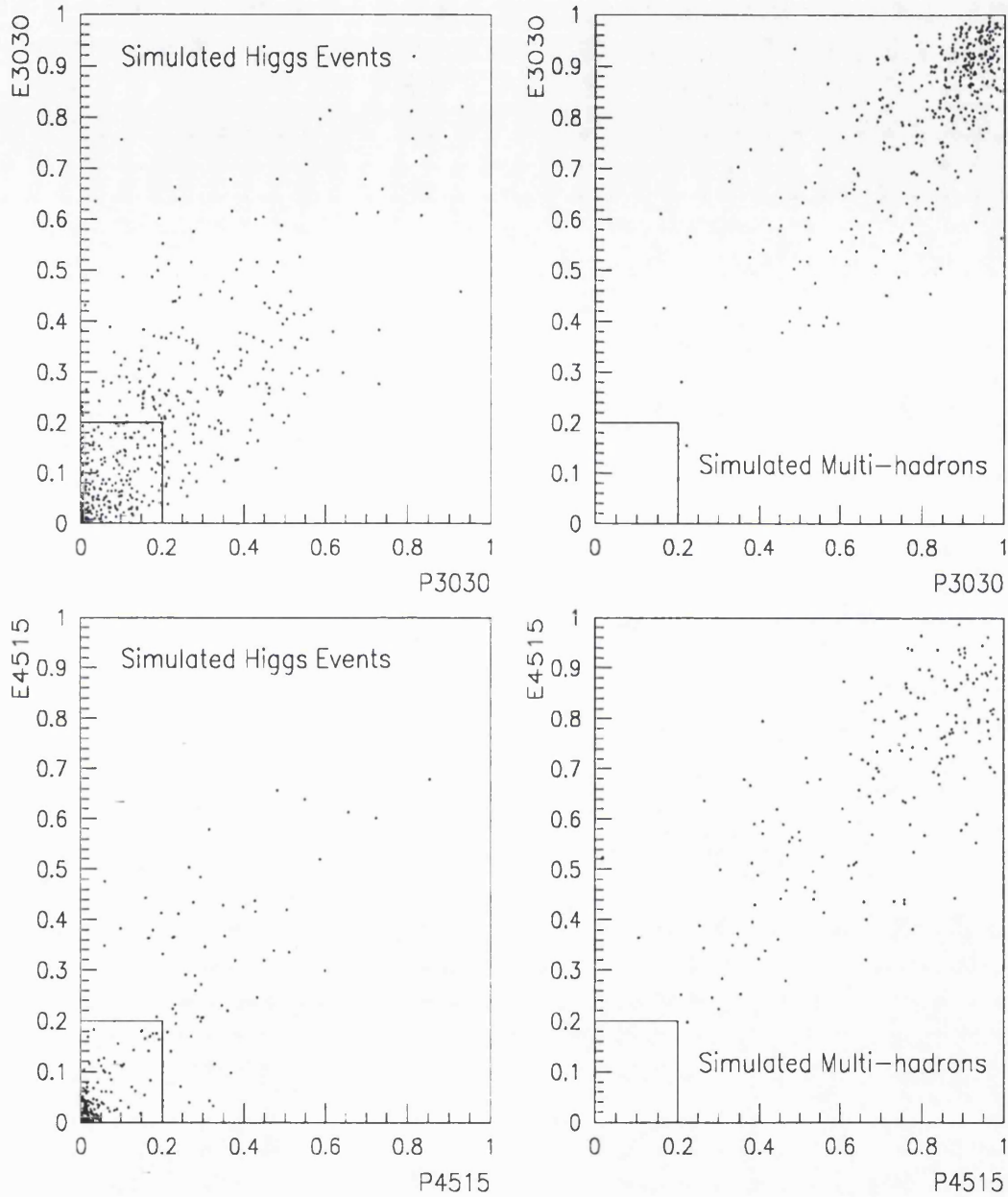


Figure 5.7: A comparison the isolation ratios for lepton tracks from samples of simulated multihadronic and Higgs ($M_H = 60$ GeV) events are shown. The number of Higgs (Multi-hadron) events analysed for these plots, corresponds to a luminosity of 12500 (78) pb^{-1} . The region of acceptance is indicated in the bottom left-hand corner of the plots.

the recoil mass in the electron channel because the cluster energy resolution was better than the track momentum resolution.

The second method, involved calculating the invariant mass of the charged and neutral particles of the hadronic system using the Globally Corrected Energy (GCE) algorithm [12] which assumes all tracks not identified as muons or electrons to be charged pions. The GCE mass (Figure 5.8) is given by

$$M_{GCE}^2 = E^2 - P_x^2 - P_y^2 - P_z^2 \quad (5.2)$$

where

$$E = \sum_{clusters} E^* + \sum_{tracks} (P^* - E_\pi^*), \quad (5.3)$$

$$P_i = \sum_{clusters} E_i^* + \sum_{tracks} (P_i^* - E_\pi^* \cdot P_i^* / P^*) \quad (5.4)$$

and $i = x, y$ and z denote the three cartesian components. E^* and P^* , are cluster energy and scalar track momentum respectively. E_π^* , which is the calorimetric (electromagnetic) energy deposited by a charged pion as a function of its momentum, is an energy subtraction made for each charged track in order to correct for double counting of energy resulting from adding a track's momentum to its associated cluster energy. The momentum dependence of E_π^* , has been determined from a study [12] of simulated charged pions to be given by

$$E_\pi^*(P) = -0.267025 + 0.611160 \cdot P + 0.000479 \cdot P^2 \quad (5.5)$$

For an electron track, E_π^* is its scalar track momentum. For a muon with momentum greater than or equal to 3 GeV, $E_\pi^* = 3$ GeV, whilst for a muon with momentum less than 3 GeV, $E_\pi^* = P/2$.

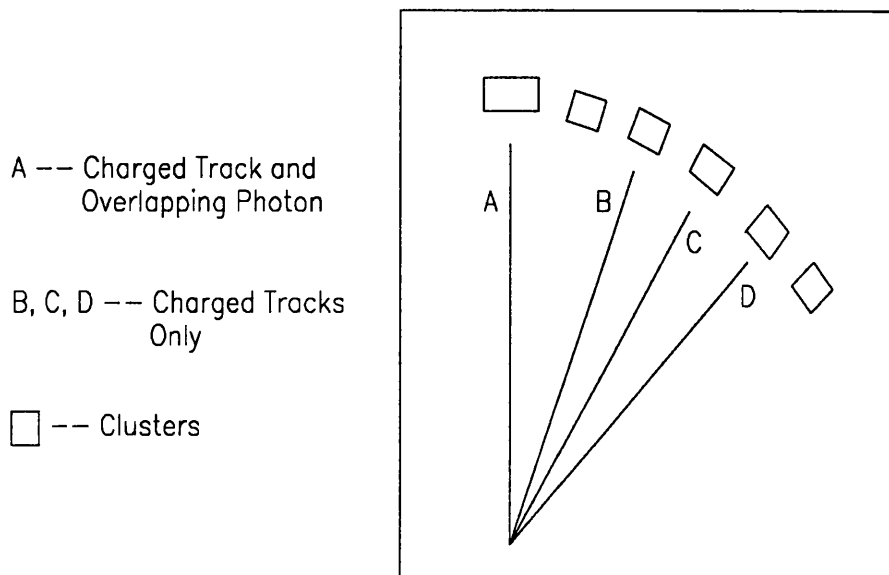
Figure 5.9 shows a comparison between the GCE mass distributions for samples of simulated and real $Z^0 \rightarrow q\bar{q}$ events. Since the two distributions compare well, the GCE mass results for simulated Higgs events were taken to be valid for real Higgs events. For simulated Higgs events, a comparison is made between the calculated hadronic mass and the true Higgs mass in Figure 5.10. The recoil and GCE mass resolutions, and scale factors ($M_{observed}/M_{true}$) are compared in Figure 5.11. The recoil mass calculation can be seen to have a superior mass resolution, and a scale factor close to 1.

The combined average (muon and electron channels) mass resolutions, and scale factors, are given respectively by

- 0.033 ± 0.008 and 1.011 ± 0.001 for the recoil mass calculation and,
- 0.225 ± 0.008 and 0.810 ± 0.009 for the GCE algorithm.

The invariant mass (M_{ll}) of the lepton pair was given by

$$M_{ll}^2 = 2E_1 E_2 (1 - \cos \theta) \quad (5.6)$$



ENERGY OF HADRONIC SYSTEM (INSET) IS GIVEN BY,

$$E = E^1 + E^2 + \dots + (P^1 - C^1) + (P^2 - C^2) + \dots$$

E^i = Energy of Clusters

P^n = Scalar Momentum of Tracks

C^n = Energy Deposited by Tracks

Figure 5.8: An illustration of the GCE algorithm. C^n is the calorimetric energy deposited by a charged pion as a function of its momentum. Note that $E > E^1 + E^2 + \dots$ since hadrons do not usually deposit all their energy in the electromagnetic calorimeter. Note also that by ignoring all clusters having associated tracks, we would be losing information about neutral particles such as the overlapping photon.

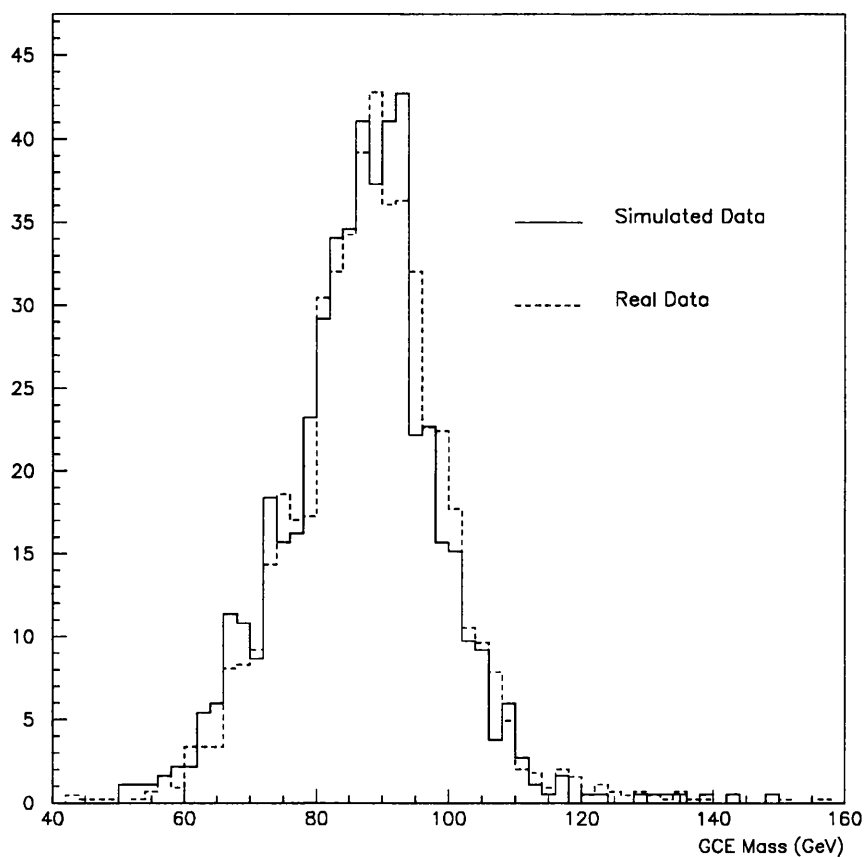


Figure 5.9: A comparison of the GCE mass distributions for samples of simulated and real hadronic Z^0 decay events.

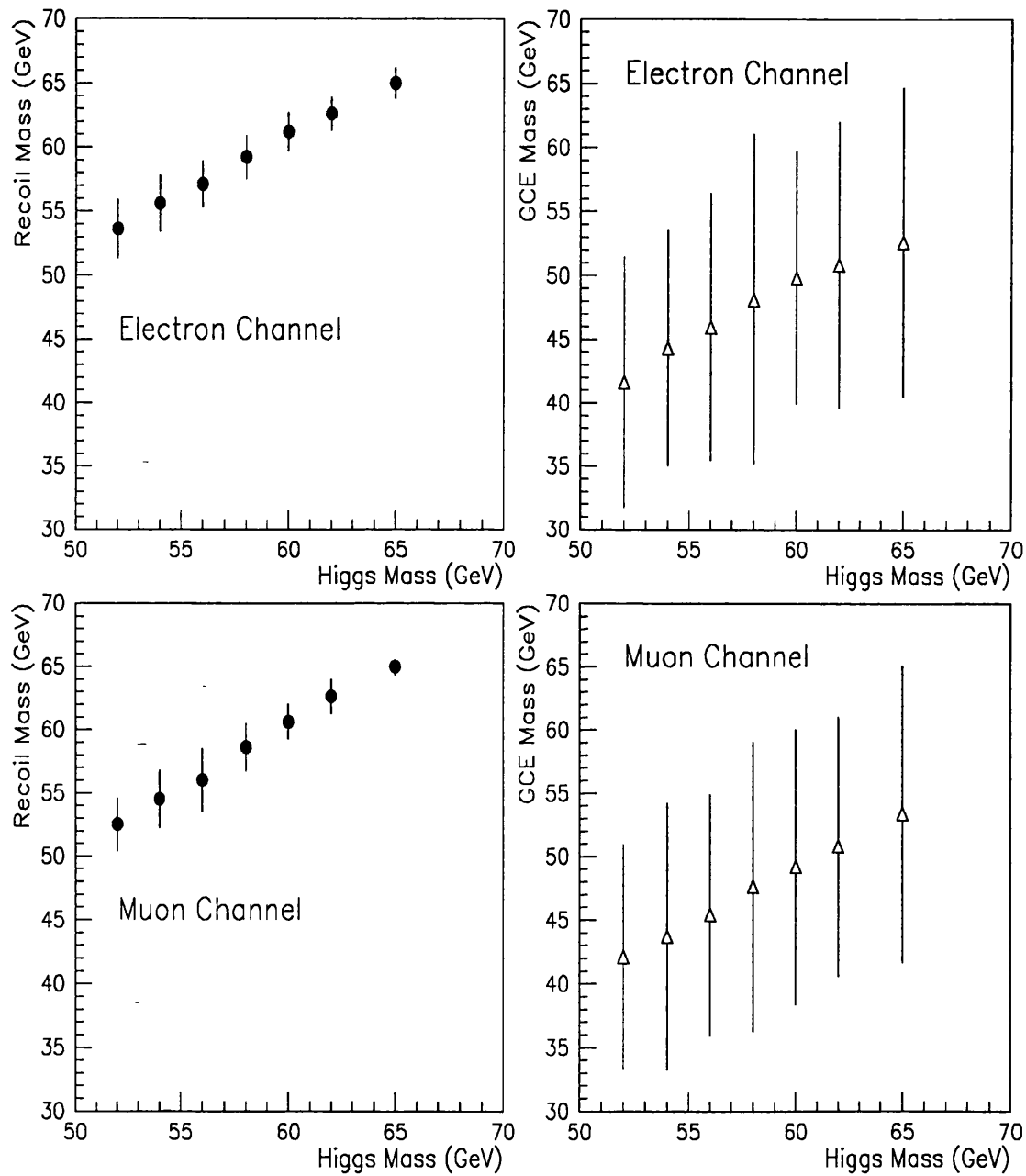


Figure 5.10: A comparison between the estimated hadronic masses and the true Higgs mass, for the electron and muon channels.

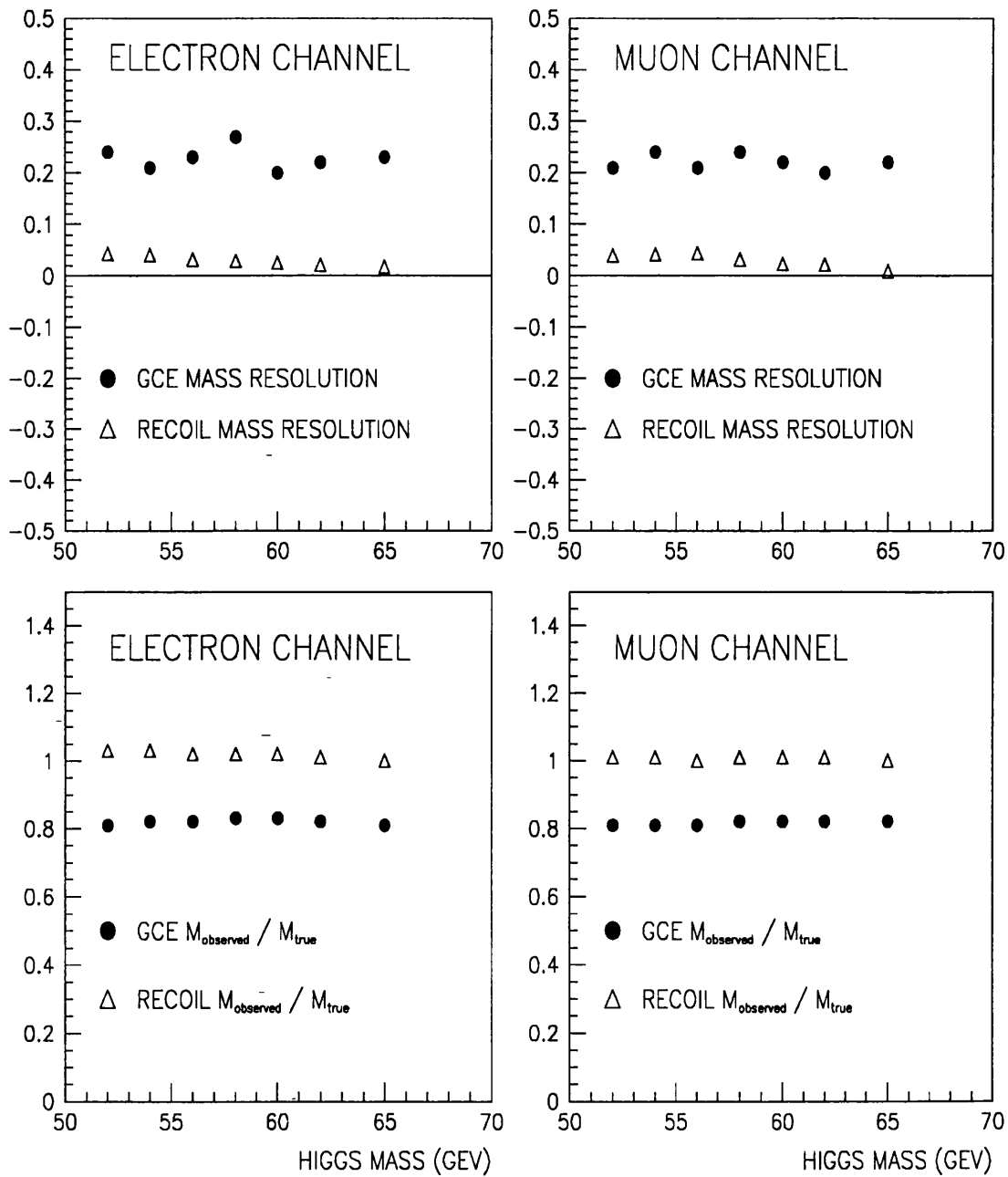


Figure 5.11: The GCE and recoil mass resolutions, and scale factors for the electron and muon channels.

where all the variables are defined as in Equation (5.1).

Four-fermion events were further suppressed by mass cuts since in most four-fermion events, one fermion pair originates from the decay of the Z^0 and so has large mass, while the other pair originates from a virtual photon, and so is characterized by a low mass (Figures 4.6(1) and 5.12). It was therefore required that,

- the invariant mass of the lepton pair be greater than 15 GeV.
- the GCE mass of all tracks and clusters lying outside 15° cones about the lepton tracks be greater than 25 GeV.

The GCE algorithm was used in the previous searches for a Higgs of mass below 40 GeV since it had a better resolution than the recoil mass. In the interest of maintaining a stable analysis, the GCE algorithm has been used in the present analysis where it no longer gives the desired mass resolutions; this is because the poor resolutions have no effect on the derivation of the mass limits.

5.4 Event Selection Efficiencies

The search algorithm was used in analysing a selection of simulated Higgs event samples, and simulated $Z^0 \rightarrow \bar{q}q$ events which contained at least two oppositely charged leptons originating from semi-leptonic decays of heavy hadrons.

The number of simulated Higgs events successively passing the electron and muon analyses cuts are contained in Tables 5.1 and 5.2. The decrease in the signal identification efficiency versus M_H was mainly due to the decrease in the average lepton pair mass and momenta as M_H increased.

Table 5.1: Number of simulated Higgs events remaining after successive cuts in the muon channel.

Higgs mass (GeV)	52	54	56	58	60	62	65
Number processed	1000	1000	1000	1000	1000	1000	1000
Event filter	818	773	806	807	808	812	760
Common Cuts	791	748	779	778	784	783	731
μ -pair identification	688	654	661	664	648	653	472
Isolation Cuts	557	519	525	525	494	497	345
Di-lepton Mass Cut	512	461	467	470	411	404	335
Hadronic Mass Cut	505	455	460	465	407	402	330

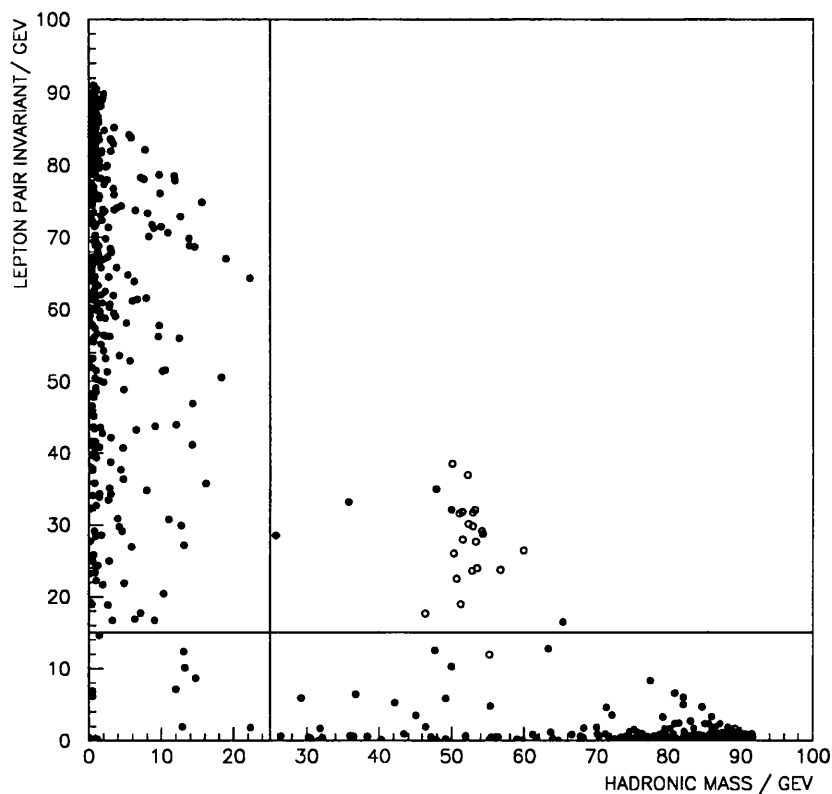


Figure 5.12: The hadronic mass *vs* the lepton pair mass for four-fermion events (black circles) and a 52 GeV Higgs signal (open circles). The number of Higgs events and four-fermion events have been normalised to the same luminosity (78 pb^{-1}).

Table 5.2: Number of simulated Higgs events remaining after successive cuts in the electron channel.

Higgs mass (GeV)	52	54	56	58	60	62	65
Number processed	1000	1000	1000	1000	1000	1000	1000
Event filter	796	778	802	778	770	786	740
Common Cuts	771	749	772	746	739	764	709
e-pair identification	601	572	562	540	520	494	297
Isolation Cuts	486	476	458	436	409	390	229
Di-lepton Mass Cut	448	426	406	389	348	333	220
Hadronic Mass Cut	445	420	402	386	347	333	220

The number of simulated $Z^0 \rightarrow \bar{q}q$ events successively passing the electron and muon analyses cuts are contained in Table 5.3. No events passed all the cuts.

During the time of this study, the generated four-vector data for four-fermion events had not been fed into GOPAL, the OPAL detector simulation program, to enable full event simulation. The search algorithm was thus adapted to analyse the four-fermion events at the four-vector level. The adapted analyses consisted only of lepton momentum, lepton isolation, lepton pair mass and recoil mass cuts. The four-vectors were generated for the events of the type $l^+l^-q\bar{q}$ where l denotes a muon or an electron, and q denotes all the known quark types. Table 5.4 contains the number of four-fermion events successively passing the cuts of the adapted electron and muon channel analyses.

At a luminosity corresponding to that of the OPAL data (*i.e.* 78 pb^{-1}), 4.21 (1) events with hadronic mass greater than 25 (50) GeV passed all the cuts.

Table 5.3: Number of Monte Carlo $Z^0 \rightarrow \bar{q}q$ events remaining after successive cuts in the electron and muon channels. The number of processed events corresponds to a luminosity equal to that of the OPAL data (78 pb^{-1}).

Cuts	electron channel	muon channel
Number processed	1900000	1900000
Event filter	149129	149129
Common Cuts	74523	74523
lepton-pair identification	502	2187
Isolation Cuts	0	0
Di-lepton Mass Cut	0	0
Hadronic Mass Cut	0	0

Table 5.4: Number of four-fermion events remaining after successive cuts in the electron and muon channels. The numbers in the ‘Mass Cuts’ column, are the number of events with hadronic mass greater than 50 GeV. The entries in the last column have been scaled to the luminosity of the OPAL data (78 pb^{-1}).

Four Fermion Process	Number Processed	Cross Section (pb)	Isolation Cuts	Momentum Cuts	Mass Cuts	Expected Number
$eeuu$	1405	0.05	1223	1144	86	0.24
$eedd$	1405	0.01	1223	1144	86	0.05
$eecc$	1415	0.05	1230	1142	90	0.25
$eess$	1408	0.01	1226	1143	85	0.05
$eebb$	1407	0.01	1243	1144	93	0.04
$\mu\mu uu$	1440	0.03	1243	1114	87	0.14
$\mu\mu dd$	1440	0.01	1243	1114	87	0.03
$\mu\mu cc$	1455	0.03	1258	1128	97	0.14
$\mu\mu ss$	1447	0.01	1248	1118	88	0.03
$\mu\mu bb$	1474	0.01	1299	1157	114	0.03

5.5 The Lepton Identification Efficiencies and Systematic Errors

To obtain an estimate of the signal selection efficiency ($\bar{\epsilon}$) for real Higgs events, the signal selection efficiency for the simulated events was corrected using a certain factor. In previous OPAL searches, this correction factor (F) was taken to be the difference in the lepton identification efficiencies of single beam energy lepton tracks taken from simulated, and real lepton pair events. The corrected Higgs signal selection efficiency ($\bar{\epsilon}$) then becomes

$$\bar{\epsilon} = (1 - F) \cdot \epsilon \quad (5.7)$$

The statistical error in this correction factor was taken to be the systematic error in the lepton identification procedure of the search.

The results of a study of the momentum dependence of the lepton identification efficiencies and the correction factor as a function of polar angle θ , and the determination of the probability of isolated hadrons to be identified as leptons are presented in this section. The momentum bins for which the study was performed were: 0 to 25 GeV, 25 to 40 GeV, and 40 to 45 GeV. The bin boundaries were chosen such that we had an adequate number of tracks in each bin from the track selection process (see below). The polar angular regions were defined by the

- end cap regions, $0.96 > |\cos\theta| \geq 0.84$, referred to as regions ‘A’.
- overlap regions, $0.84 > |\cos\theta| \geq 0.70$, referred to as regions ‘B’.
- barrel region, $0.72 > |\cos\theta| \geq 0.00$, referred to as region ‘C’.

The study was possible for the first time due to the present size of the OPAL data which gives a large sample of low momentum isolated leptons.

5.5.1 Selection of Lepton Tracks for the Study

Real and simulated electron/muon tracks, were selected from the real and simulated lepton pair events. Lepton pair events are flagged as such by ROPE [46], the OPAL event reconstruction program, where a 99.8 (99.9) % [48] event selection efficiency at a 99.2 (99.9) % [48] purity level are claimed for electron (muon) pairs. To obtain beam energy lepton tracks from the lepton pair events, these tracks were taken from

- the electron pair events with only two tracks with the opening angle between them greater than 170 degrees, and each with momentum and associated cluster energy greater than 40 GeV.
- the muon pair events with only two tracks with the opening angle between them greater than 170 degrees, and each with momentum greater than 40 GeV.

In selecting low momentum leptons (defined as leptons with momentum less than 40 GeV), final state radiative electron and muon pair events were used. In the electron (muon) pair events, it was required that an event had only three good electromagnetic clusters and two tracks. The most energetic of the two tracks was required to have a momentum greater than 40 GeV, and associated cluster energy greater (less) than 40 (3) GeV. It was also demanded that one of the two other clusters had no associated tracks, and was completely isolated within a cone of half angle 10° . Finally, it was demanded that the momentum of the most energetic track, and the sum of the energy of the unassociated cluster and the momentum of other track were equal to within 5 GeV. The other track which was required to be associated to the last cluster, was taken as the low momentum lepton track. The entire OPAL lepton pair data was analysed in order to obtain a sufficient number of low momentum lepton tracks. Table 5.5 contains the number of real and simulated electron/muon tracks studied.

In order to determine the probability that isolated hadron tracks were identified as leptons a sample of isolated hadron tracks was taken from tau pair events. It was required that only one of the taus underwent a 1-prong decay. The isolated hadron

Table 5.5: Number of electron and muon tracks chosen from the real and simulated (MC) data.

Energy range (GeV)	MC electrons	Data electrons	MC muons	Data muons
0 to 25	670	933	756	262
25 to 40	1028	1111	1345	457
40 to 45	50000	10000	50000	10000

tracks were selected from the decay products of the other tau which was required to have undergone a 3-prong decay. A hadron track was defined as being isolated if it was completely isolated within a cone of half angle 10° . 1198 (251) such isolated tracks were selected from the simulated (real) data.

5.5.2 The Lepton Identification Efficiencies

The lepton identification efficiencies are shown as a function of polar angle in Figures 5.13 to 5.16. A characteristic of the plots is the lower efficiency in the end cap regions. This was mainly due to tracks failing the ‘minimum number of CJ hits of 20’ cut (see Section 5.2). It was also noticed that the electron identification efficiencies for tracks with momentum between 25 to 40 GeV, and 40 to 45 GeV, were higher than those for tracks with momentum less than 25 GeV. This was because an additional cut (dE/dx cut) was applied in the latter momentum range (see section on Lepton Identification).

The identification of isolated hadrons as muons (electrons) was not expected to exceed 5 (2) % (Table 5.7) in the momentum range below 25 GeV where most of the Higgs signal leptons were expected to be.

5.5.3 Determination of the Correction Factors (and Systematic Errors) and their Momentum Dependence

Before merging all the efficiency differences from the whole four years of data when computing the correction factors for the beam energy leptons, the data consistency was checked. No systematic differences in the lepton identification efficiencies between the years were noticed. Table 5.6 contains all the differences between the simulated and real data identification efficiencies for the three momentum bins.

In computing the correction factors and their statistical errors for each of the three momentum bins, the difference between the simulated and real data efficiency and its corresponding error were computed in each of the detector regions (see second

columns of Figures 5.15 and 5.16). The correction factor and its error were taken to be the weighted mean and error of all the efficiency differences in the detector regions.

To determine the momentum dependence of the correction factor, each factor was plotted on a graph as an ordinate, and the mean of the track momenta in its corresponding momentum bin as the abscissa. A selection of curves were fitted through the three coordinates (Figures 5.17), the curve having the smallest chi-squared was chosen.

For the beam energy leptons, the values 0.50% and 0.10% were obtained for the correction factor and systematic error respectively. Compared to the previously quoted values of 7.0% and 0.8% [26], a significant improvement was seen. The improvement in the systematic error was due to the larger amount of data used in the present study whilst the improvement in the correction factor was due to better simulations for beam energy leptons.

The relatively larger correction factors for the low energy electrons (momentum less than 40 GeV) were due to differences between the real and simulated data arising from better electron track and cluster matchings in the simulated data.

For the low energy muons, the differences between the real and simulated data were mainly due to more simulated tracks passing the inclusive muon identification procedure.

Table 5.8 contains the summary of the results obtained for the correction factors and the systematic errors, whilst the same information is shown as plots in Figures 5.17.

5.6 The Neutrino Channel Search

The author did not undertake a major part in the neutrino channel search, but a brief presentation is given for completeness. This channel accounted for almost 75% of the total search sensitivity because the decay rate of Z^* to neutrinos is about 3 times its decay to muons and electrons. The experimental signature of events containing Higgs bosons was expected to be a non back-to-back pair of jets (Figure 5.18). To identify events with this topology, the analysed events were split into two hemispheres using the plane normal to the thrust axis (the thrust axis is the direction which minimizes the sum of all the transverse momenta relative to it). The missing energy vector and the momentum vectors of the hemispheres were calculated, then the acolinearity angle (θ_{acol} , the complement of the 3-dimensional angle between the two momentum vectors) and the acoplanarity angle (θ_{acop} , the complement of the angle between the projections of the momentum vectors onto the plane

Table 5.6: The MC efficiency minus the data efficiencies and their corresponding errors, in parentheses, are expressed in % for each of the detector regions for the three momentum ranges.

End Cap	Overlap	Barrel	Overlap	End Cap
Beam energy electrons				
8.11(1.47)	4.92(0.92)	0.45(0.11)	2.60(0.75)	4.94(1.41)
Electrons with momentum < 40 GeV and > 25 GeV				
7.03(5.61)	5.12(4.04)	0.46(0.53)	5.48(3.25)	0.43(5.51)
Electrons with momentum < 25 GeV				
0.87(4.04)	7.22(10.16)	-0.11(3.21)	17.64(9.88)	2.05(4.41)
Beam energy muons				
-1.21(2.19)	0.53(1.27)	-0.04(0.23)	-0.00(1.24)	2.43(2.17)
Muons with momentum < 40 GeV and > 25 GeV				
15.00(11.50)	5.66(7.95)	-1.66(0.87)	5.26(6.62)	-8.37(9.61)
Muons with momentum < 25 GeV				
24.60(11.40)	16.70(9.24)	0.06(1.34)	8.00(8.38)	-2.46(15.00)

Table 5.7: The number of hadron tracks (from taus) studied, and the number identified as electrons and muons in parentheses.

Data Type	Number identified as Muons	Number identified as Electrons
momentum < 25 GeV		
Simulated data	1164 (28)	1164 (42)
Real data	238 (12)	238 (4)
momentum > 25 GeV		
Simulated data	34 (2)	34 (4)
Real data	13 (1)	13 (2)

Table 5.8: Summary of the correction factor F and systematic error on F (in parentheses), are expressed in % for the three momentum ranges.

Range /GeV	Muons	Electrons	Combined
0 to 25	1.34(1.30)	11.35(3.82)	2.38(1.23)
25 to 40	-1.42(0.85)	3.03(1.38)	-0.19(0.73)
Beam energy	-0.01(0.22)	0.62(0.11)	0.50(0.10)

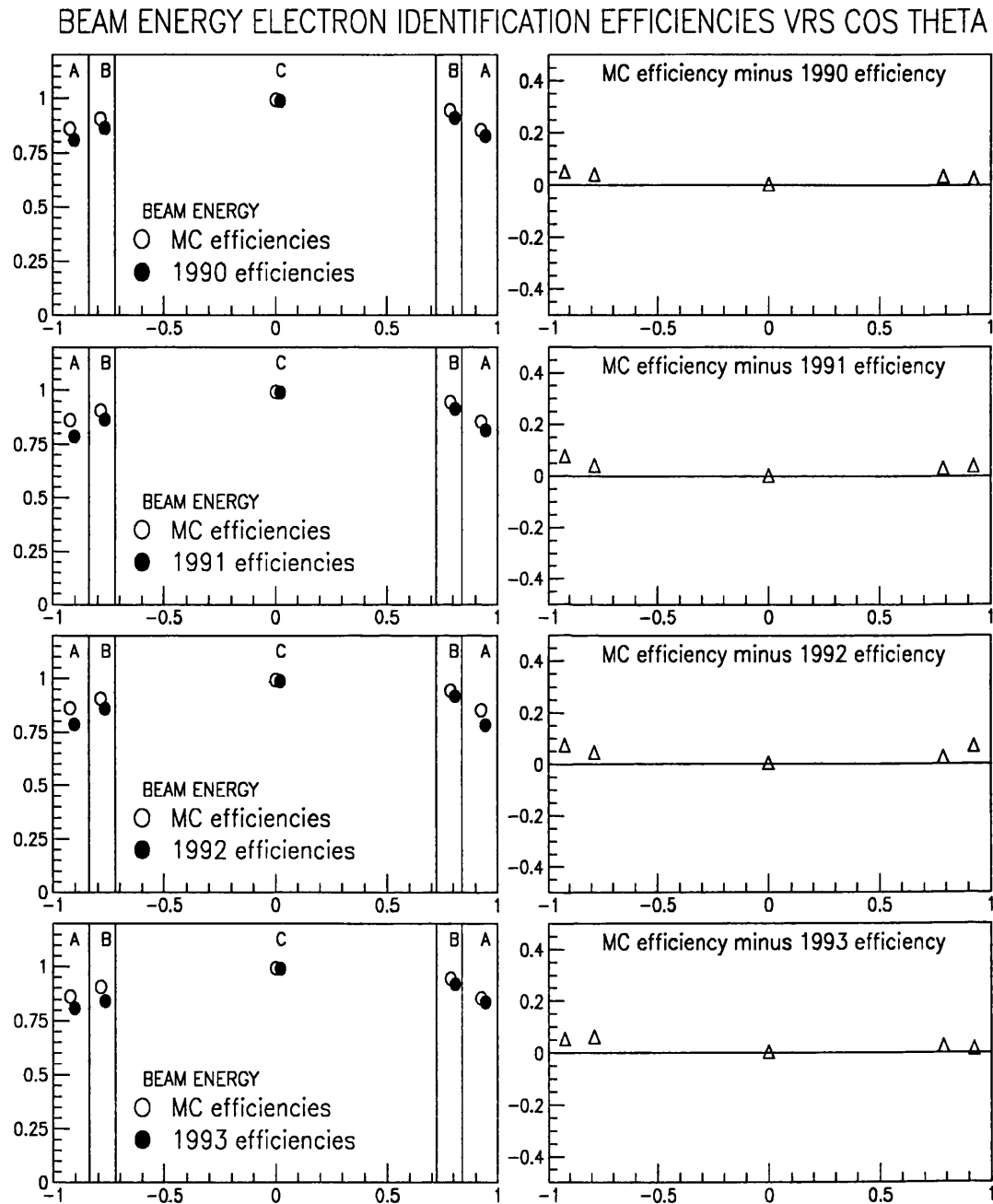


Figure 5.13: These plots show the efficiencies and efficiency differences in the five detector regions for beam energy electrons. The error bars are present but are too small to be visible. ‘A’(‘B’) denotes the end cap (overlap) regions, ‘C’ denotes the barrel region.

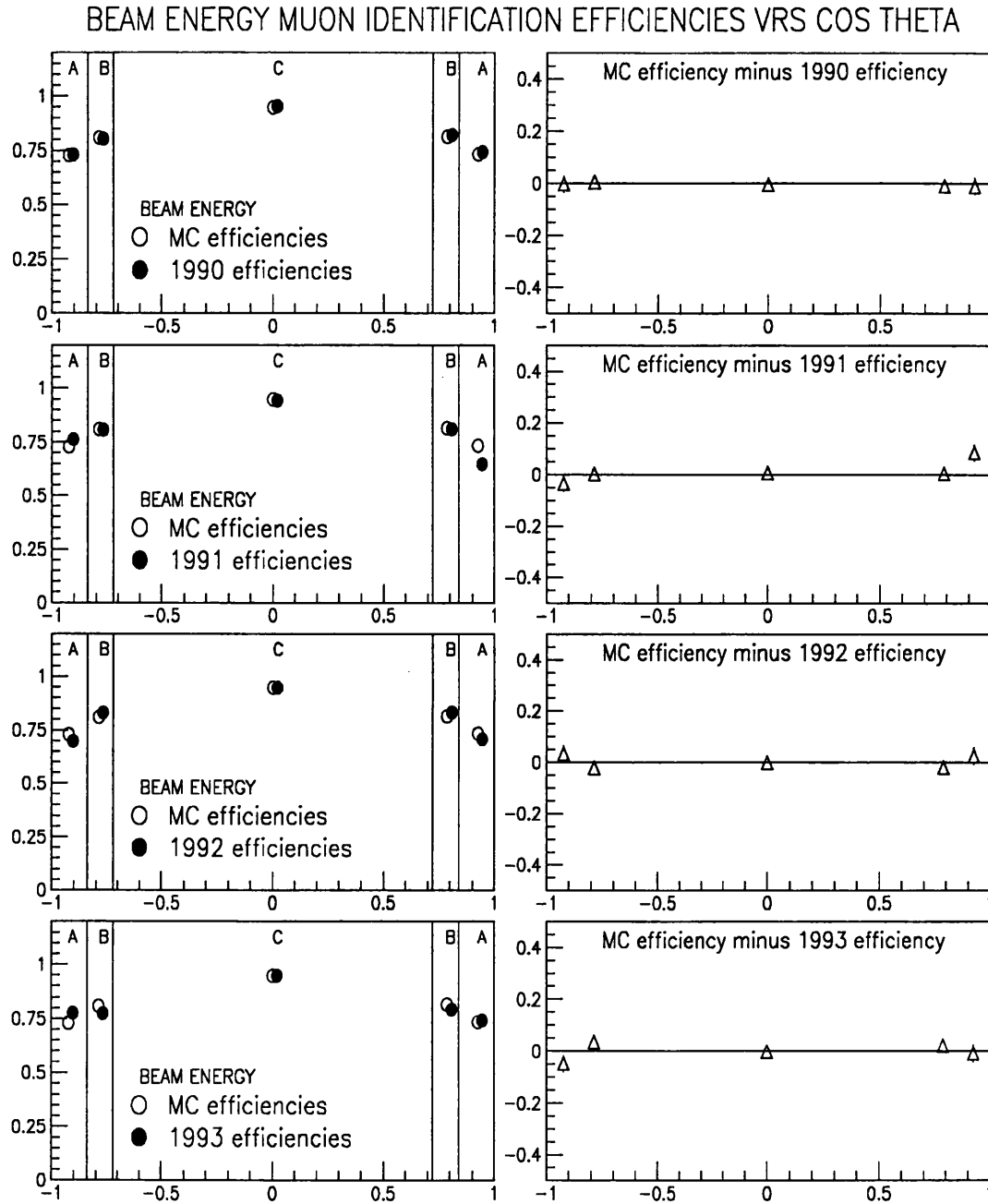


Figure 5.14: These plots show the efficiencies and efficiency differences in the five detector regions for beam energy muons. The error bars are present but are too small to be visible. 'A'('B') denotes the end cap (overlap) regions, 'C' denotes the barrel region.

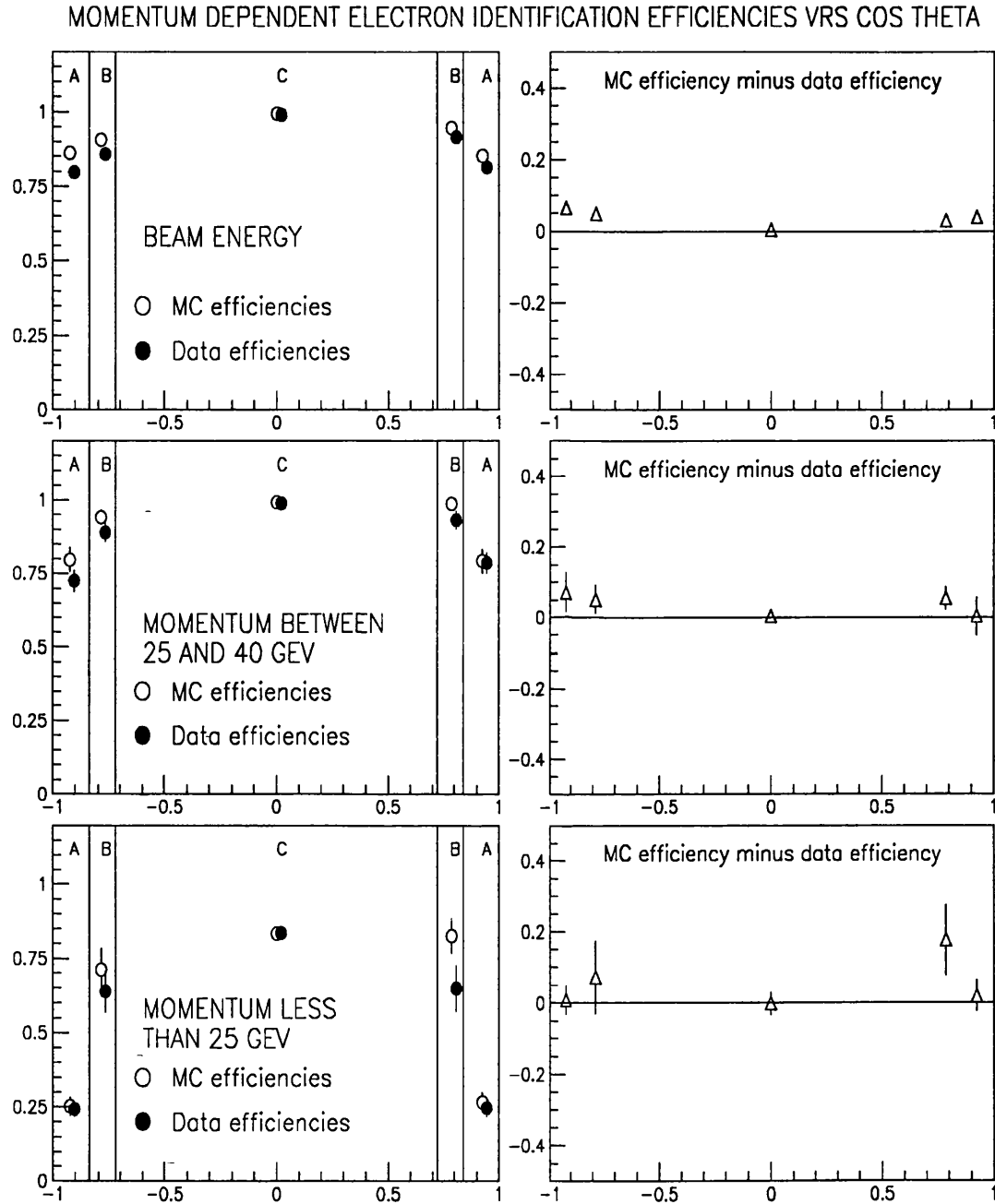


Figure 5.15: These plots show the electron efficiencies and efficiency differences in the five detector regions for the three momentum bins. The non-existent error bars for the lower momentum electrons are due to 100% efficiencies.

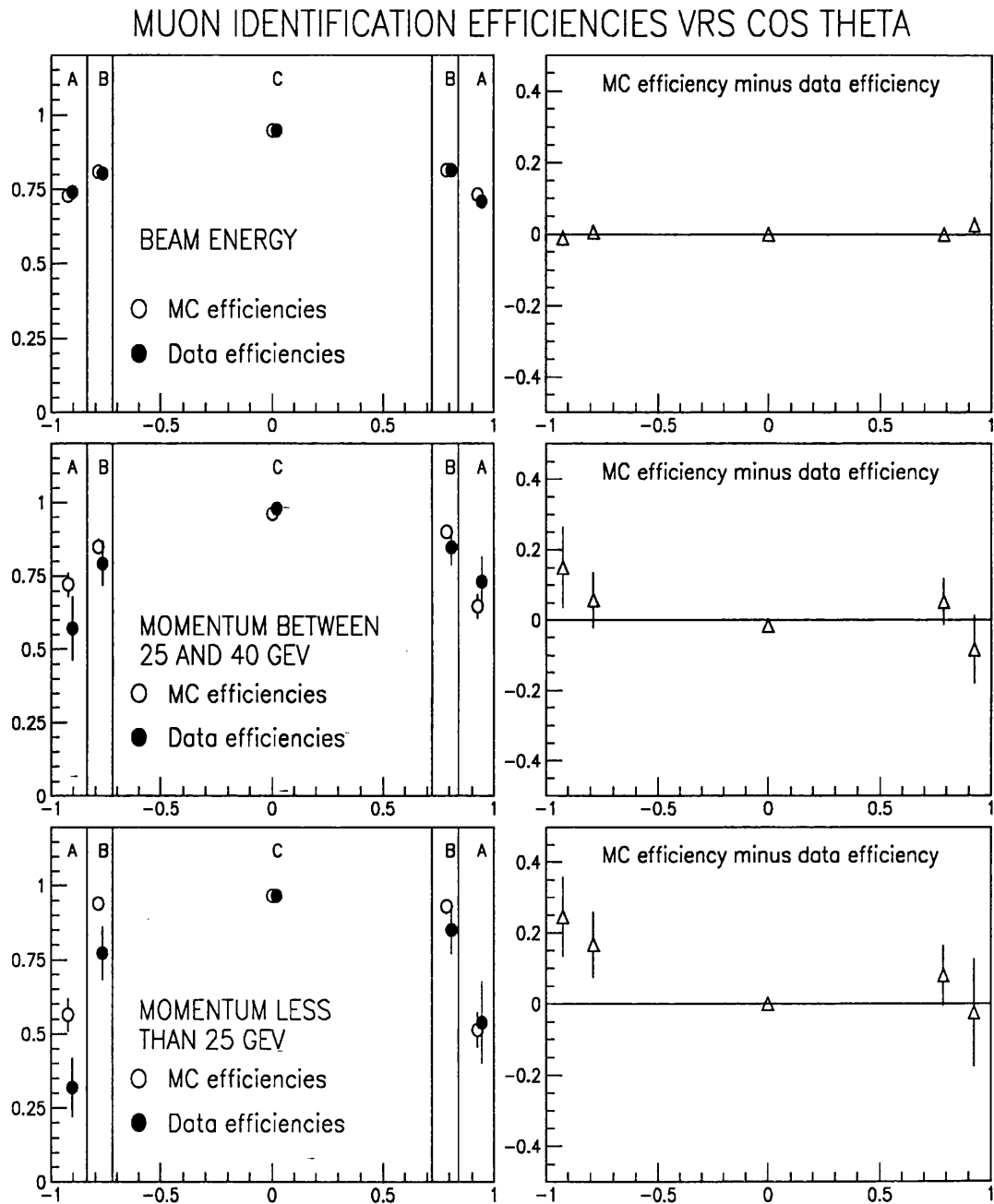


Figure 5.16: These plots show the muon efficiencies and efficiency differences in the five detector regions for the three momentum bins. The non-existent error bars for the lower momentum muons are due to 100% efficiencies.

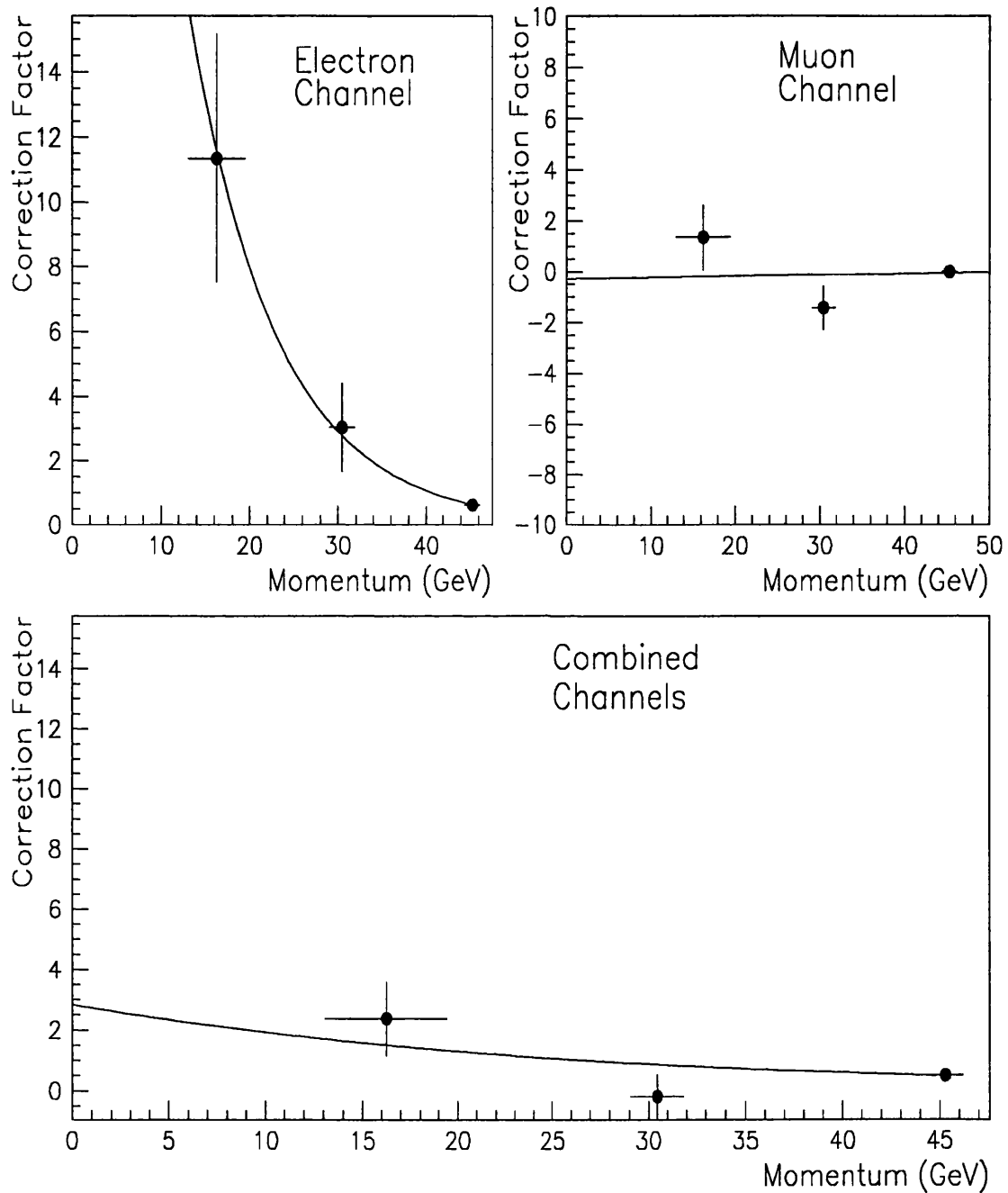


Figure 5.17: Plots of the correction factors (in %) for the three momentum bins. The factors are plotted at the momentum points corresponding to the mean of the momenta of the tracks used in the study, in the momentum bins. The horizontal error bars are a measure of the spread of momenta about these means. For the electron (muon) channel, an exponential (linear) fit was found to be the most suitable fit.

perpendicular to the beam direction) were computed. Since momentum conservation in hadronic Z^0 decays keeps the observed hemisphere momentum vectors back-to-back, an event displaying a significant deviation from a back-to-back topology and having a large and isolated missing momentum/energy vector is possibly due to the process $Z^0 \rightarrow H^0 \nu \bar{\nu}$.

The search in this channel, proceeded via an initial data reduction by selecting only events having $\cos \theta_{acol} < 0.98$. A requirement that the track and cluster multiplicities were each greater than seven was also imposed to eliminate virtually all leptonic Z^0 decays including $\tau^+ \tau^-$ events with a converting photon.

To ensure a reliable measurement of the acolinearity and acoplanarity angles, the missing energy of an event needed to be accurately measured and its direction well contained. Events with large energy flow near the beam pipe were eliminated by requiring that

- the energy deposited in the forward calorimeters was less than 2 GeV.
- the missing momentum vector was limited to polar angular range defined by $|\cos \theta| < 0.94$.
- the forward energy flow, defined by $(E_F^2 + E_B^2)/E_{tot}^2$, was less than 10. E_{tot} is the total energy of the event, E_F and E_B are the total weighted energies observed in the forward and backward cones defined by $|\cos \theta| < 0.80$. The momenta of the charged tracks and the energies of the electromagnetic clusters with polar angle θ , were weighted by $\sin^{-2} \theta$, thus giving more importance to the energy of tracks and clusters near the beam pipe.
- the z-component of the total event momentum was less than 20 GeV.

A reliable measurement of the acolinearity and acoplanarity angles is also dependent on the event shape since the angles are better measured for two-jet events than

for spherical events. Spherical events were rejected by demanding that the event thrust was greater than 0.70.

Two photon events of the type shown in Figure 4.6(8) – where the fermions q^1 and q^2 are lost down the beam pipe and k^1 and k^2 are quarks – were potential background events. These events were suppressed by requiring that the GCE mass of the event was greater than 25 GeV, and the total transverse momentum relative to the beam axis was less than 10 GeV.

Hadronic Z^0 decays having the presence of high energy neutrinos from heavy quark decays, or energetic and poorly detected neutral hadrons, are also backgrounds to the signal. To suppress these events, it was demanded that the missing energy vector satisfied the following isolation criterion:

- The sum of the charged track energy and the cluster energy in the electromagnetic and hadron calorimeters must be less than 2.0 GeV in a cone of half-angle 45° centered on the missing energy vector.

The full details of the analysis in the neutrino channel can be found in reference [12].

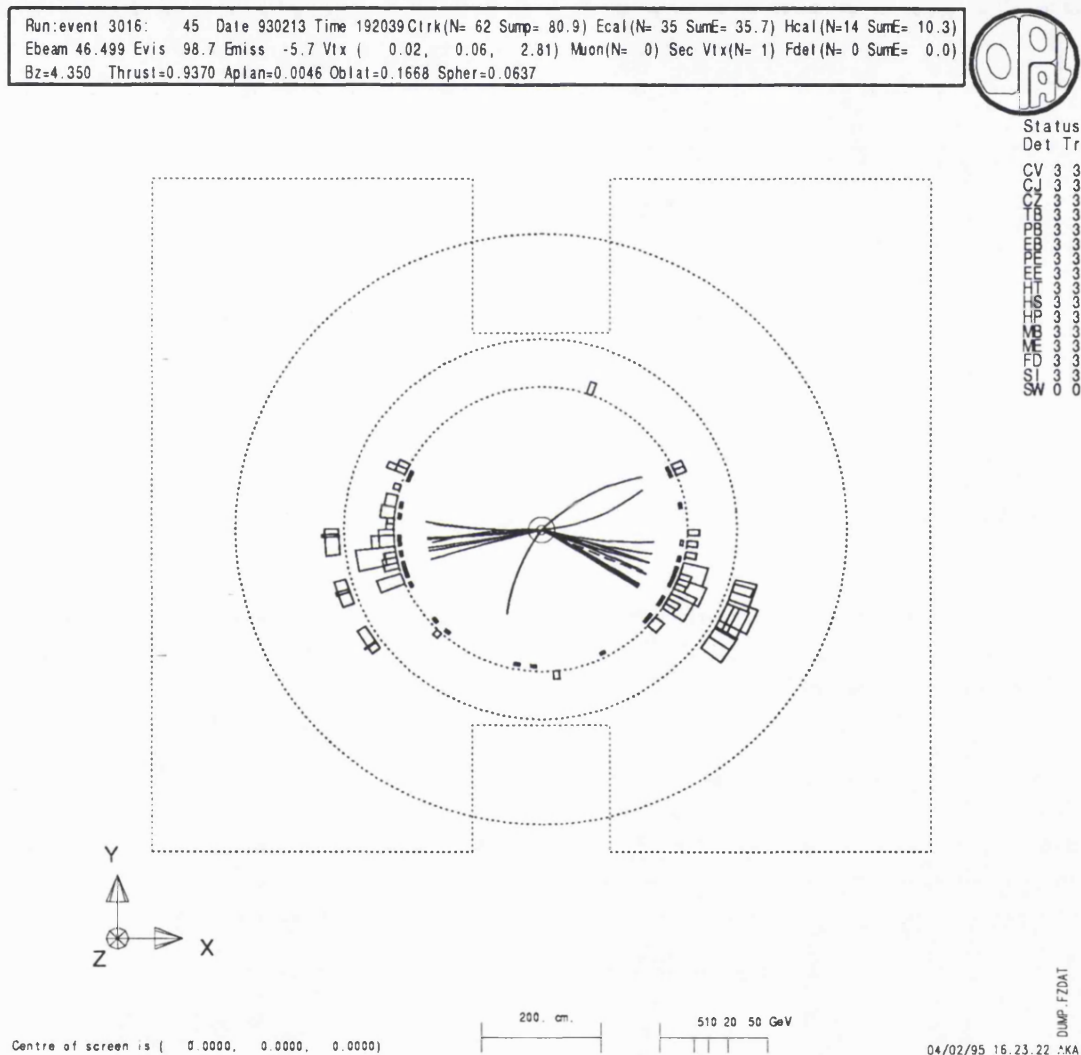


Figure 5.18: A computer reconstruction of a simulated Higgs signal in the neutrino channel.

Chapter 6

THE RESULTS OF THE SEARCH

1,992,586 hadronic Z^0 decay events, corresponding to an integrated luminosity of 78 pb^{-1} were recorded by the OPAL detector in the period 1990 to 1993. To ensure the reliability of the event reconstruction, only events recorded when all the major components of OPAL were operational were considered for analysis. The major detector components were the central jet chamber, the electromagnetic calorimeter, the hadronic calorimeter, the muon chamber, and the forward detector.

The Higgs mass limit obtained using the 1990 and 1991 data has already been published in reference [53]. No Higgs candidate events were found in that study. This chapter reports on the extension of the analysis onto the 1992 and 1993 data, and on the combination of the results from all the four years' data to produce a new lower limit on the Higgs mass at 56.9 GeV, at 95% confidence level.

6.1 The Leptonic Channel Search

6.1.1 Data Consistency Checks

In order to combine data from the years 1992 and 1993, the consistency of the two data sets was checked. Distributions were compared between each year for the lepton-candidate track and cluster parameters on which cuts were applied during the search. The results of the consistency checks are summarised in Figures 6.1 to 6.4. No significant differences between the data sets of each year were observed.

During some data-taking periods in 1993, the gamma-catchers of the forward detector developed a problem resulting in the forward detector registering spuriously.

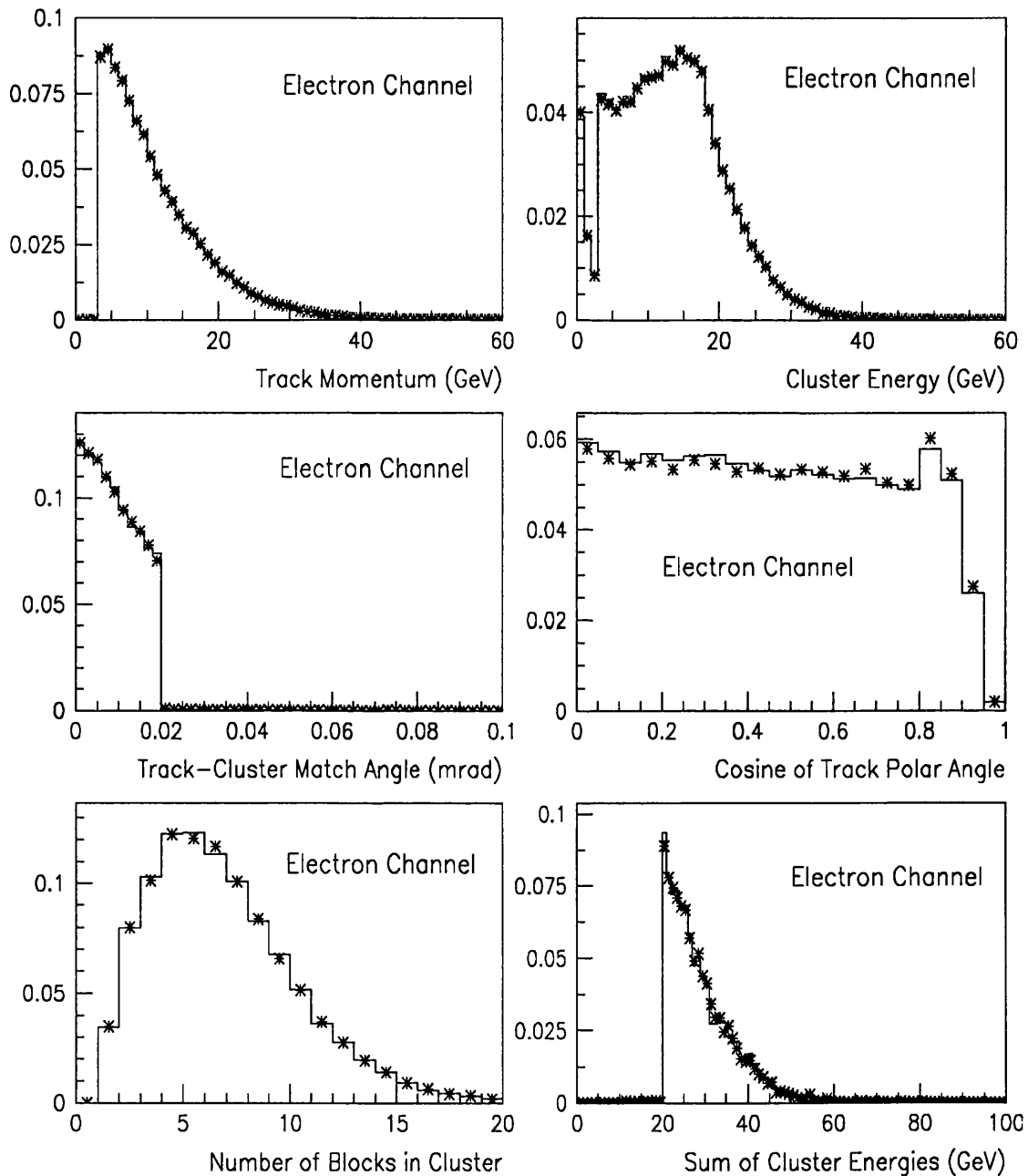


Figure 6.1: Comparisons between the 1992 (stars) and the 1993 (histogram) distributions for the electron-candidate track and cluster parameters on which cuts were applied. The number of entries in the distributions have been normalised to one.

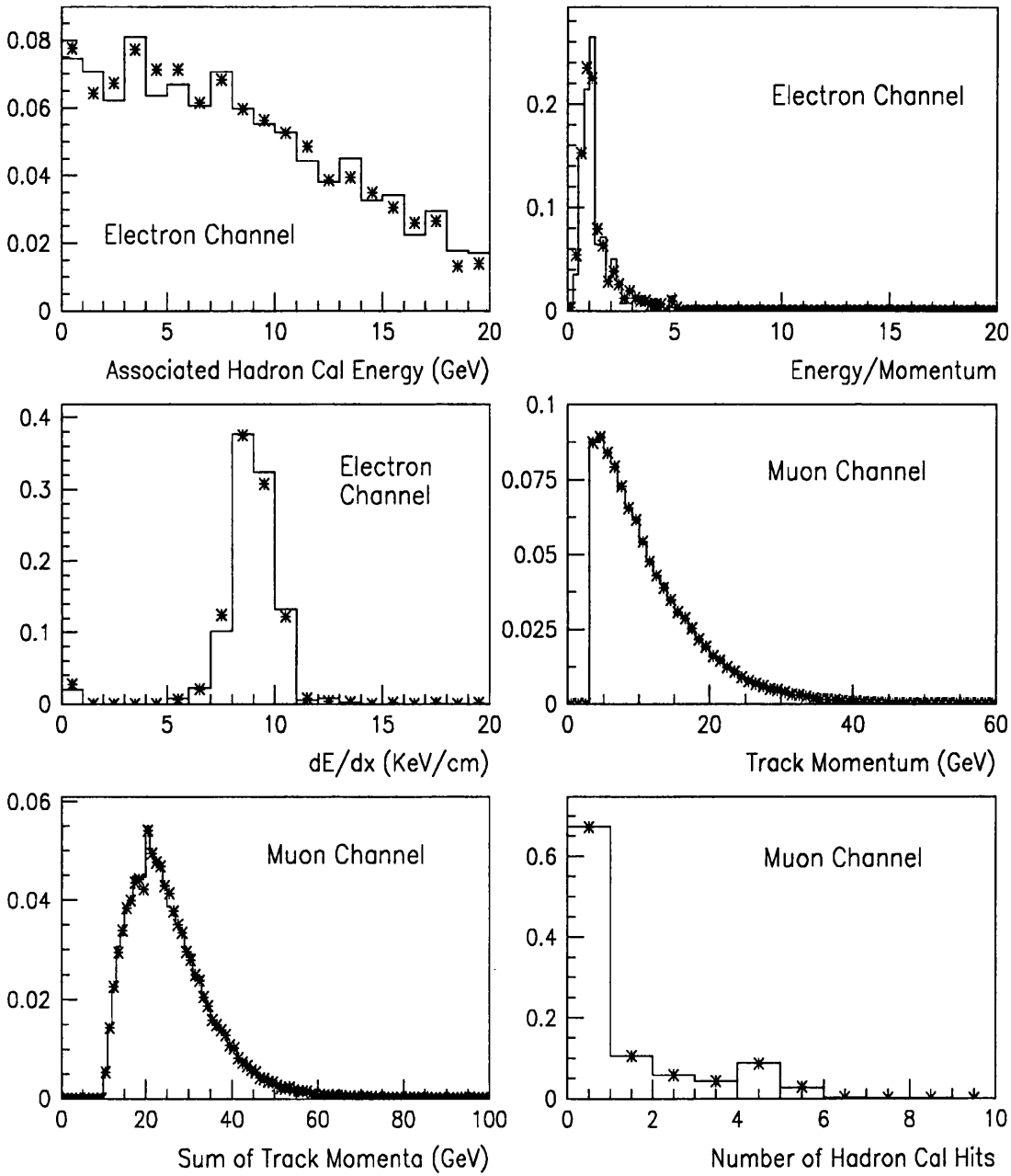


Figure 6.2: Comparisons between the 1992 (stars) and the 1993 (histogram) distributions for the electron and muon-candidate track parameters on which cuts were applied. The number of entries in the distributions have been normalised to one.

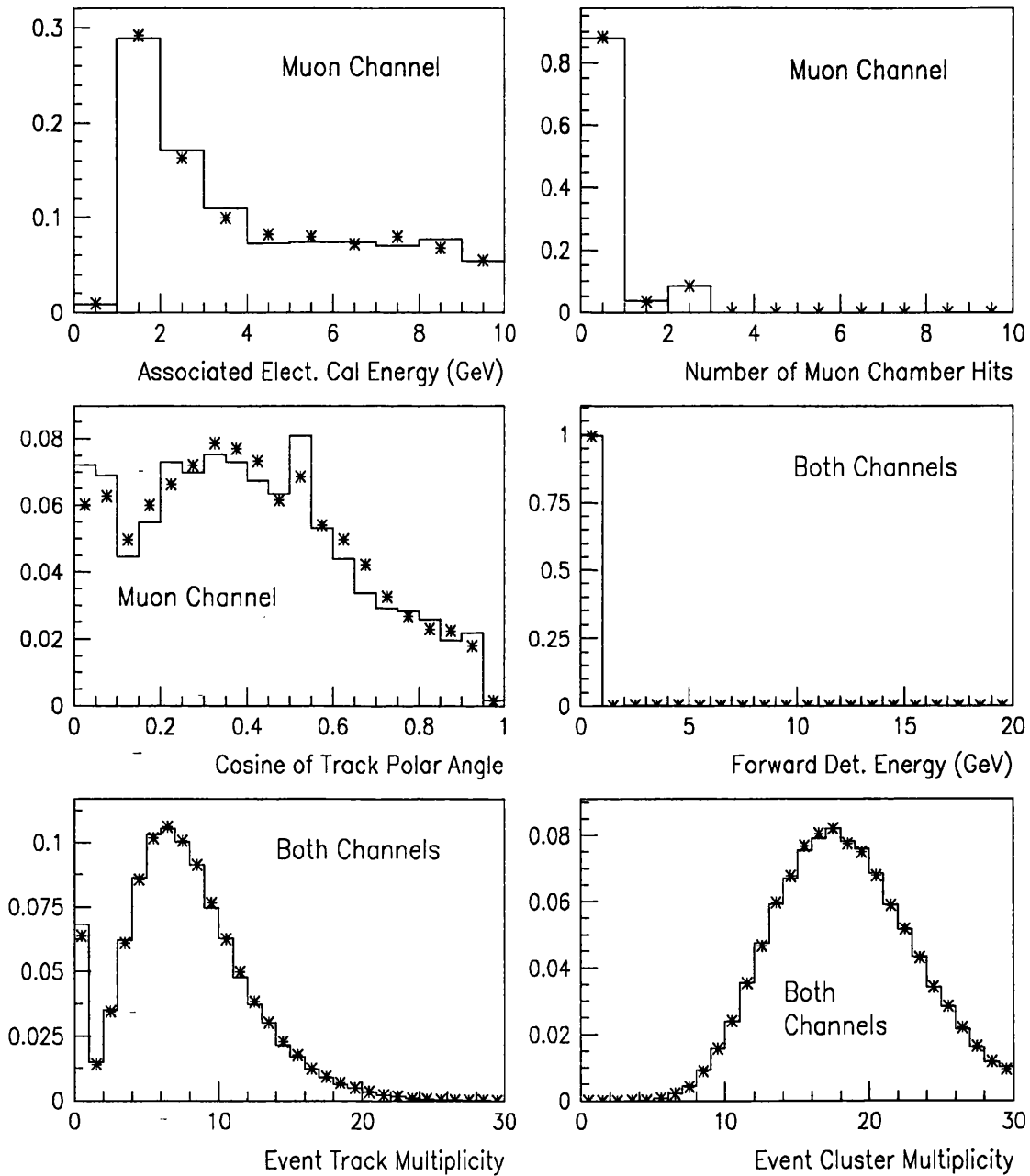


Figure 6.3: Comparisons between the 1992 (stars) and the 1993 (histogram) distributions for the muon-candidate track and event parameters on which cuts were applied. The number of entries in the distributions have been normalised to one.

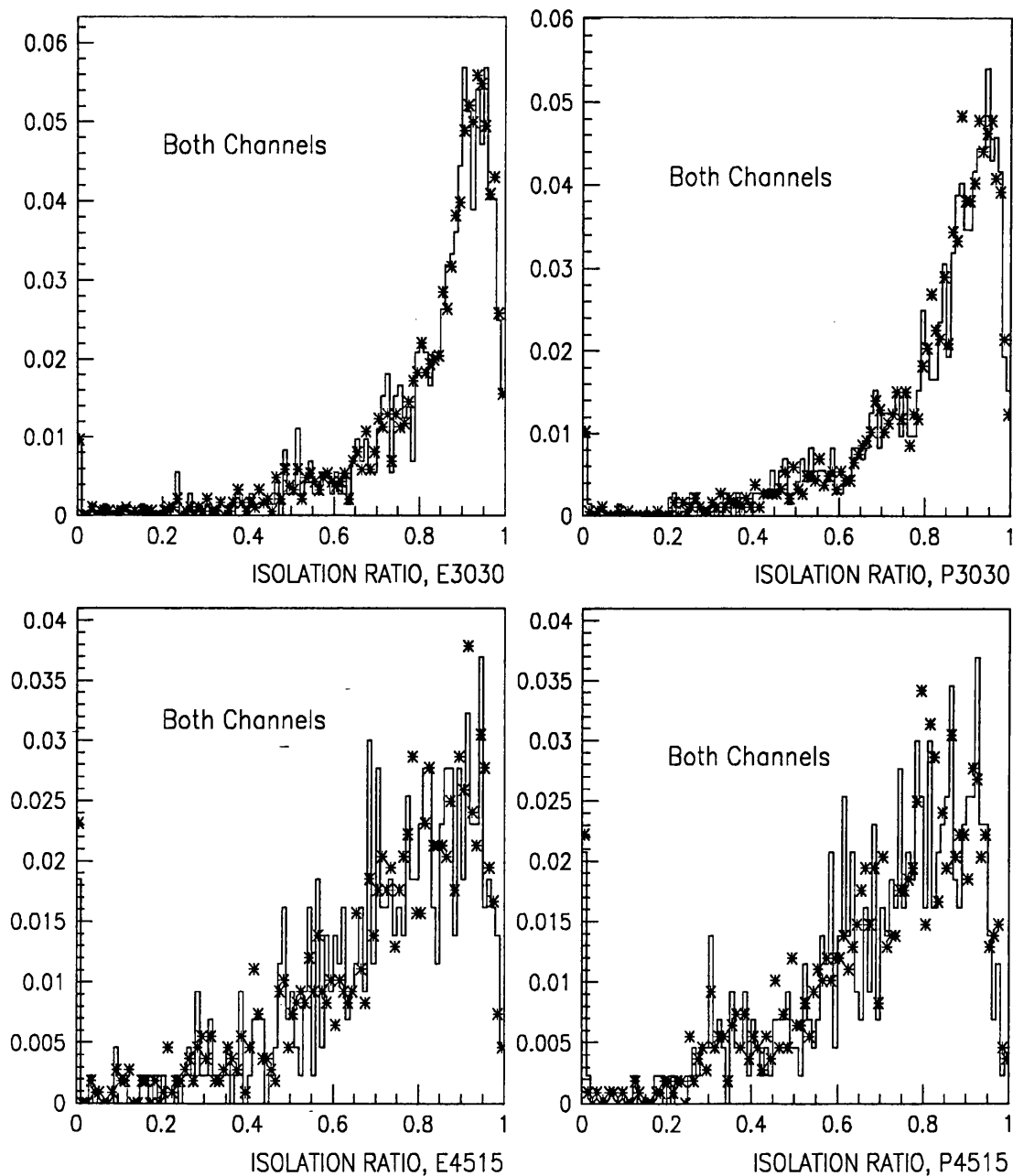


Figure 6.4: Comparisons between the 1992 (stars) and the 1993 (histogram) distributions for the isolation ratios for the muon and electron candidates. The number of entries in the distributions have been normalised to one.

high energies. The gamma-catcher energy was thus removed from the total forward detector energy when analysing the data for those periods.

6.1.2 The Leptonic Channel Results

The distributions of the lepton-candidate isolation ratios (cf Figure 5.7) for the 1992 and 1993 events selected by the event filter, are shown in Figure 6.5. The lepton pair mass versus GCE mass distribution for the events passing all but the mass cuts is shown in Figure 6.6. In both Figures, the cut positions are indicated.

The number of the 1990 to 1993 real events, simulated hadronic Z^0 decay events, and simulated Higgs ($M_H = 60$ GeV) events after the successive cuts in the electron and muon channel analyses are summarised in Tables 6.1 and 6.2. One event – event 15048, run 4353 – from the 1993 data, was accepted in the muon channel. This was consistent with the expected number of background events with hadronic mass greater than 50 GeV (see later).

Table 6.1: Number of events after successive cuts in the muon channel for the data, for simulated hadronic Z^0 decay events, and for simulated Higgs ($M_H = 60$ GeV) events. The number of events have been scaled so that the real and simulated data samples have a luminosity of 78 pb^{-1} . The numbers between parentheses give efficiencies.

Cuts	Data	$Z^0 \rightarrow qq$	$\mu\mu H^0$
Event filter	139481 (7.00%)	149129 (7.49%)	0.82 (81%)
Common	64754 (3.25%)	74523 (3.74%)	0.74 (74%)
μ -pair identification	1658 (0.08%)	2187 (0.11%)	0.65 (65%)
Isolation	15 (0.00%)	0 (0.00%)	0.50 (49%)
Di-lepton Mass	15 (0.00%)	0 (0.00%)	0.41 (41%)
Hadronic Mass	1 (0.00%)	0 (0.00%)	0.41 (41%)

6.1.3 The Surviving Event

The surviving event (Figure 6.7) had two energetic and isolated muons of momenta 19.3 ± 0.7 GeV and 7.3 ± 0.2 GeV, and a three-jet hadronic system. The muons were clearly identified by both the muon chambers and the hadronic calorimeter, and satisfied all the track isolation criteria.

The lepton pair mass, the recoil mass and the GCE mass (after correction for the mass shift using $M_{observed}/M_{true}$) were calculated to be 16.6 ± 0.3 GeV, 61.2 ± 1.0

GeV and 57.11 ± 7 GeV respectively. The recoil and GCE masses were consistent with each other.

Table 6.2: Number of events after successive cuts in the electron channel for the data, for simulated hadronic Z^0 decay events, and for simulated Higgs ($M_H = 60$ GeV) events. The number of events have been scaled so that the real and simulated data samples have a luminosity of 78 pb^{-1} . The numbers between parentheses give efficiencies.

Cuts	Data	$Z^0 \rightarrow qq$	eeH^0
Event filter	139957 (7.03%)	149129 (7.49%)	0.78 (77%)
Common	64978 (3.26%)	74523 (3.74%)	0.68 (68%)
e -pair identification	312 (0.02%)	502 (0.03%)	0.53 (52%)
Isolation	14 (0.00%)	0 (0.00%)	0.41 (41%)
Di-lepton Mass	14 (0.00%)	0 (0.00%)	0.35 (35%)
Hadronic Mass	0 (0.00%)	0 (0.00%)	0.35 (35%)

The most energetic jet contained a secondary vertex with a statistical significance of 4.4. This vertex contained four charged tracks, one of which was a 1.5 GeV electron; these were indications that the jet contained a heavy flavoured hadron, as expected from a Higgs event. There were no indications of the presence of secondary vertices in the other two jets. The event properties are summarised in Table 6.3. The jet reconstruction and beauty tagging algorithms used are described below.

Jet Finding in the Event

The Durham jet finding algorithm [50] was used. The jet finding was performed by associating tracks to a direction of maximum energy flow. The number of jets successfully reconstructed by the algorithm depended on a user-defined minimum value y_m for the quantity y_{ij} for any pair of tracks i and j , defined by

$$y_{ij} = \frac{m_{ij}^2}{E_{cm}^2} \quad (6.1)$$

where E_{cm} is the center of mass energy, and

$$m_{ij}^2 = \text{Max}(E_i, E_j)(1 - \cos \theta_{ij}). \quad (6.2)$$

E_i is the energy of the i th track and θ_{ij} is the opening angle between the track pair.

The value y_{ij} was calculated for all possible track pairs; the four-vectors of the track pair with the lowest y_{ij} were added to form a pseudo-track if $y_{ij} < y_m$ and the original tracks were not included in the subsequent y_{ij} calculations. The calculations

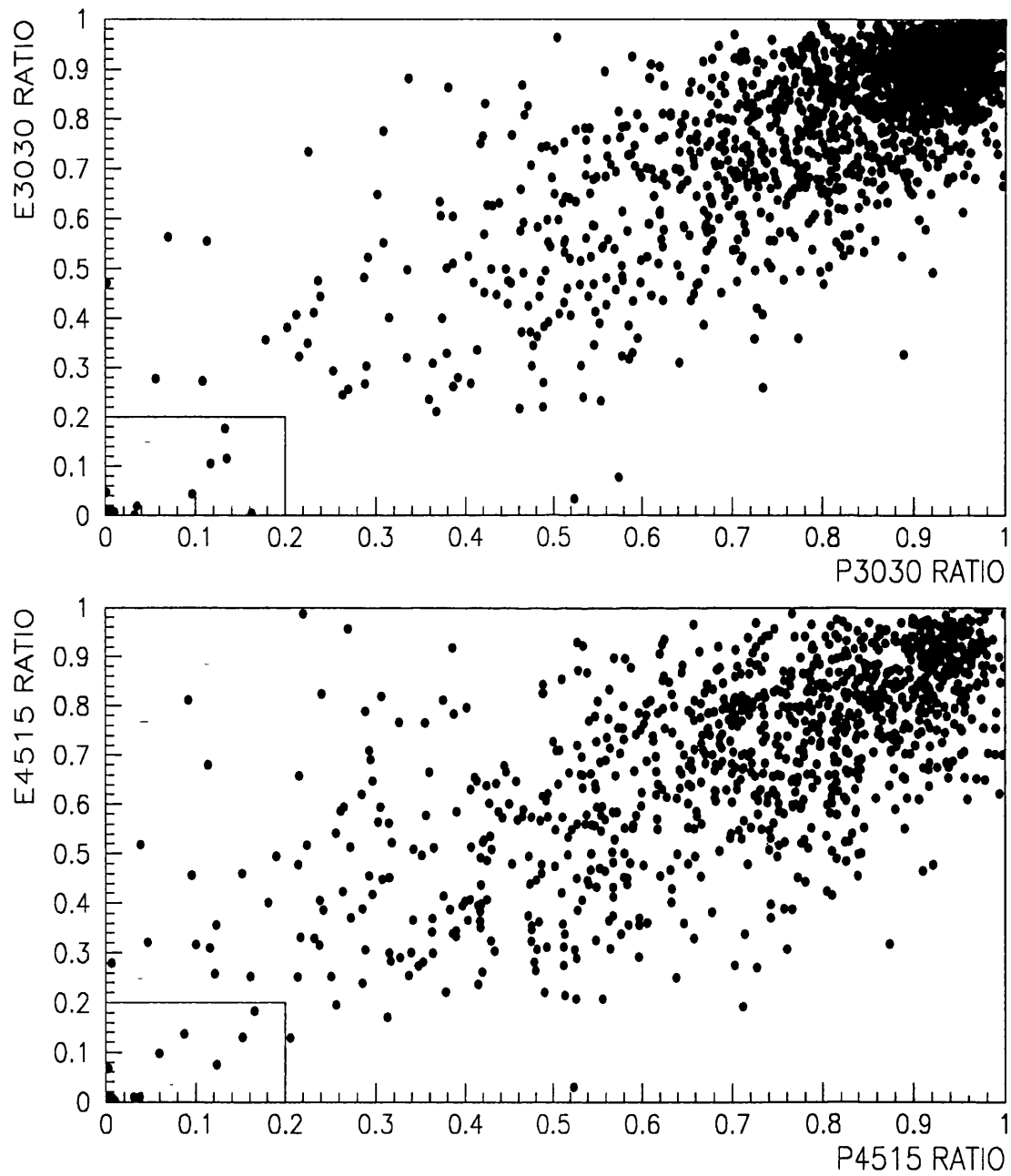


Figure 6.5: The isolation ratios for the lepton candidates in the 1992 and 1993 data.

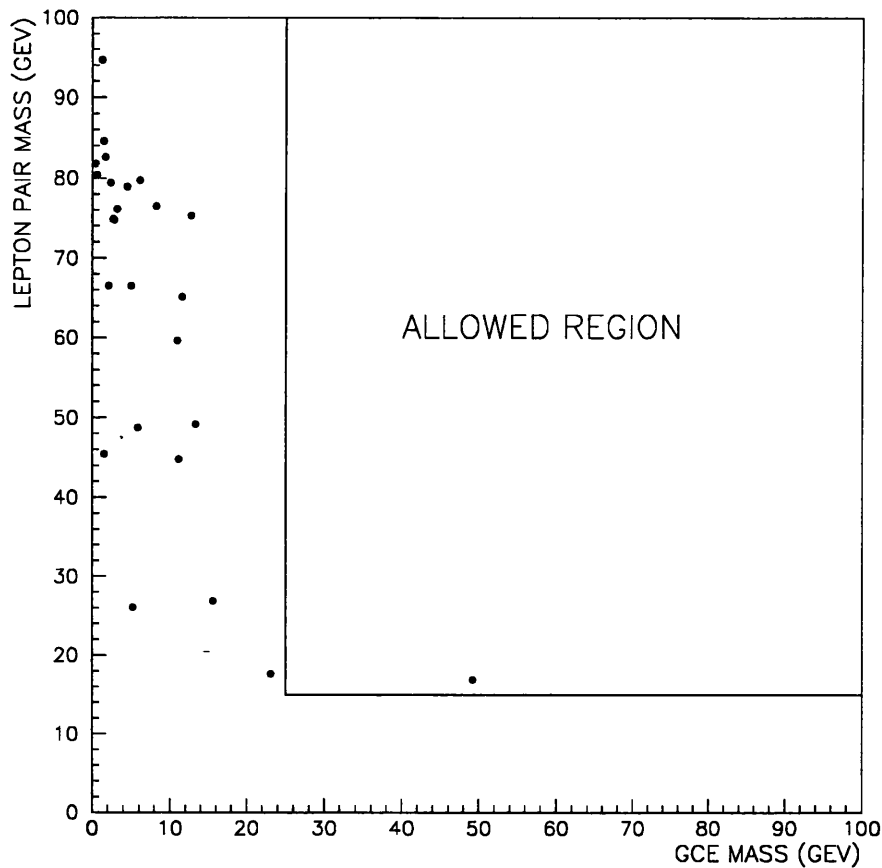


Figure 6.6: The lepton pair mass VS the GCE mass for the events, from the 1992 and 1993 data, passing all cuts except the mass cuts.

were iterated until the lowest y_{ij} exceeded y_m . The number of jets was the number of surviving single and pseudo-tracks. The actual jets were the the surviving single tracks, and the collection of tracks making up the pseudo-tracks.

Beauty Tagging

The ‘Tear-Down Vertex Finder’ [51] was used in tagging jets containing heavy hadrons. It exploited the decay vertices produced by heavy hadrons resulting from their typical decay times. This vertex finder worked by fitting all the tracks in a jet to a single vertex in the r - ϕ plane. If any track contributed more than a certain user-defined value χ_m^2 to the vertex χ^2 , it was discarded and the remaining tracks fitted to a new vertex. This procedure was iterated until no tracks contributed more than χ_m^2 to the vertex χ^2 , or until there were fewer than 3 tracks remaining, in which case the secondary vertex search was deemed to have failed. A secondary vertex with a significance (radius of vertex divided by error on radius) greater than 4.0 was considered to be produced by a heavy-flavoured hadron.

Table 6.3: Properties of the event that passed all the cuts. Momenta, masses and energies are expressed in GeV, angles in degrees, and distances in millimeters.

Property	Cut Values	Muon Values	Anti-Muon Values	Other Values
Momentum, p^μ	> 5	7.3 ± 0.2	19.3 ± 0.7	
Cluster Energy, e^μ	—	0.65 ± 0.2	0.70 ± 0.7	
Isolation, P3030	< 0.2	0.0	0.0	
Isolation, E3030	< 0.2	0.0	0.0	
Isolation, B2	< 1.0	0.0	0.0	
$\mu^+ \mu^-$ opening angle	> 30			89.0
$p^{\mu^+} + p^{\mu^-}$	> 25.0			26.6 ± 0.7
$e^{\mu^+} + e^{\mu^-}$	< 4.0			1.35 ± 0.7
Muon pair mass, $M_{\mu\mu}$	> 15.0			16.6 ± 0.3
Mass of the hadronic system	> 25			57.11 ± 7
Recoil mass	—			61.2 ± 1.0
Radius of displaced vertex	—			1.6 ± 0.4
Significance of vertex	> 4.0			4.4
Number of tracks in vertex	> 3			4
Centre-of-mass energy	—			91.17

6.1.4 Leptonic Channel Background and Total Systematic Error Estimation

The number of expected Higgs events (N_{exp}) versus the Higgs mass (M_H) is given by $N_{exp} = \bar{\epsilon} \bar{\sigma} L$, where $\bar{\epsilon}$ is the signal detection efficiency, $\bar{\sigma}$ is the Higgs production cross section, and L is the integrated luminosity. The contributions to the total uncertainty in N_{exp} for the leptonic channel were;

- 1.3% [2], for the luminosity (L).
- 2.0% [12], for the cross section ($\bar{\sigma}$). This uncertainty is due to the non-inclusion of higher order processes such as final state radiative processes in the calculation of the Bjorken cross section.
- 1.23% for the lepton identification procedure of the signal selection. This uncertainty was taken to be the uncertainty in the correction factor (F) for the momentum range, 0 to 25 GeV, as discussed in Section 5.4.

When added in quadrature, the above uncertainties give an overall uncertainty of 2.7%.

6.2 Results For the Neutrino Channel

One event with hadronic mass 28.9 ± 3.5 GeV was selected in the neutrino channel. The number of events after successive cuts are summarised in Table 6.4.

6.2.1 Neutrino Channel Background and Total Systematic Error Estimation

The dominant background was expected to be from hadronic Z^0 decays with final states containing either very energetic neutrinos, or very energetic long-lived neutral hadrons mis-measured in the hadron calorimeter. The expected number of events from this source, with mass greater than 50 GeV, was estimated to be 0.15 events.

The contributions to the total systematic error in the neutrino channel were;

- Luminosity: 1.3% [2].
- Higgs production cross section: 1.0% [2].
- Higgs signal selection efficiency: 1.8% [2].

When added in quadrature, ^{this} gives an overall uncertainty of 2.4%.

Table 6.4: Number of events after successive cuts in the neutrino channel for the 1990 to 1993 data, for simulated Z^0 decay events, and for simulated Higgs ($M_H = 60$ GeV) events. The number of events have been scaled so that the luminosities of the real and simulated data samples are the same. The numbers between parentheses give efficiencies.

Cuts	Data	$Z^0 \rightarrow qq$	$\nu\nu H^0$
Event filter	63776 (3.30%)	29830 (1.55%)	4.8 (83%)
Tau rejection	33909 (1.76%)	29163 (1.51%)	4.7 (82%)
Forward energy	17947 (0.93%)	17716 (0.92%)	4.1 (71%)
Two photon rejection	17265 (0.89%)	17714 (0.91%)	4.1 (71%)
Thrust and Missing momentum	1984 (0.10%)	2128 (0.11%)	2.6 (45%)
Acolinearity/Acoplanarity	1 (0.00%)	1.4 (0.00%)	1.9 (33%)

6.3 The Higgs Mass Limit

The total number of Higgs expected events (N_{exp}) versus the Higgs mass (M_H) for the leptonic and neutrino channels using the luminosity of the four years' data are summarised in Table 6.5. To avoid an over-estimation of N_{exp} due to systematic effects, it was reduced by one standard deviation of the total systematic uncertainty.

To obtain a conservative lower mass limit at 95% confidence level, we assumed that no background events were expected. The surviving leptonic channel event which had its mass consistent with the range 50 GeV to 70 GeV, was considered to be a Higgs event because of its proximity to the sensitivity limit of 59.5 GeV, where 3 events were predicted. The choice of the above mass range was to account for mass resolution and shift effects. The neutrino channel candidate did not affect the determination of the mass limit.

The mass limit in the presence of the candidate event, was determined by finding the value of M_H (Figure 6.8) for which $N_{exp} = 4.7^1$. We arrived at a new mass limit of **56.9 GeV** (Figure 6.8). Note that if background events had been taken in account, the total number of expected events at each mass increases; the mass limit then changes to a higher value. We give the lower limit as the conservative choice. As at July 1994, just after our (OPAL) new mass limit was published, the DELPHI collaboration also published their new mass limit as 55.7 GeV [52].

Table 6.5: Efficiencies and expected events in the neutrino and charged lepton channels. - The number of events have been reduced by one standard deviation of the systematic error.

M_H (GeV)	$\epsilon^{\nu\nu}$ (%)	$N_{exp}^{\nu\nu}$	ϵ^{ll} (%)	N_{exp}^{ll}	N_{exp}^{Total}
30	43	75.8	27	16.7	92.6
40	53	35.1	49	11.7	46.8
50	45	10.0	49	3.9	13.9
55	41	4.7	43	1.9	6.5
60	33	1.9	38	0.8	2.6
65	23	0.6	27	0.2	0.8

¹The mean of a Poisson distribution for which observing zero or one events occurs 5% of the time.

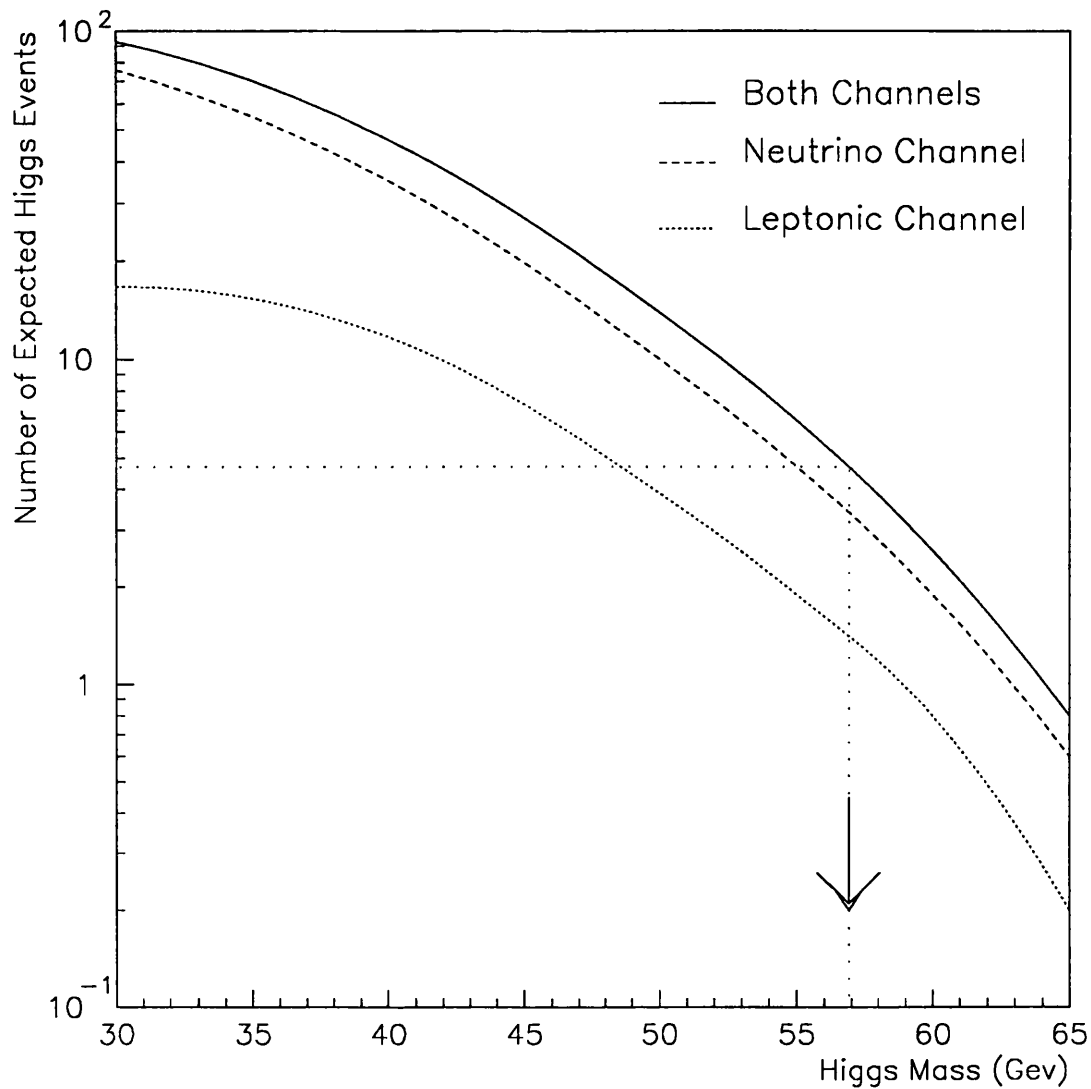


Figure 6.8: The new OPAL lower limit (arrow) on the Higgs mass of 56.9 GeV.

6.4 Conclusions and Outlook

A search has been made for the Higgs using the combined results from the previous and the present study. The search looked for reactions of the type $e^+ + e^- \rightarrow Z^* H^0$ with

$$H^0 \rightarrow \text{Hadrons, and}$$

$$Z^* \rightarrow \nu\nu \text{ or } e^+e^- \text{ or } \mu\mu.$$

The search was sensitive to a Higgs signal in the mass range 25 to 65 GeV. One

event with mass 28.9 ± 3.5 GeV passed the neutrino channel selection, and one event with recoil mass 61.2 ± 1.0 GeV passed the leptonic channel selection. Since the candidate with mass 28.9 GeV has a negligible effect on the final mass limit, the limit was determined using the event observed in the leptonic channel as a Higgs candidate. A new lower mass limit for the Standard Model Higgs boson was then established at **56.9 GeV** at 95% confidence level.

By the time the second phase of LEP (LEP-2), where beam energies of up to 90 GeV are envisaged, becomes operational, OPAL would have recorded an additional amount of data which will only enable the mass limit to be extended to at most 65 GeV – provided the Higgs is not discovered.

At LEP-2, the Bjorken cross sections for $M_H > 60$ GeV are expected to be orders of magnitude higher than they are at the present LEP energies (Figure 4.4). An H^0 and a real Z^0 are expected to be produced in the final state at LEP-2 energies (see Section 4.2). The neutrino channel search algorithm will be similar to that at LEP-1. The leptonic channel search will be altered slightly, in that it will be demanded that the mass of the lepton pair is consistent with that of a Z^0 .

The exploitation of the decay mode $H^0 \rightarrow \bar{q}q$, $Z^0 \rightarrow \bar{q}q$ will also become feasible because of its distinctive signature – four hadronic jets, two of which have an invariant mass consistent with that of a Z^0 . The OPAL collaboration has conducted simulation studies [54] to determine the Higgs discovery potential using the new LEP machine. The indications are that the mass region 60 GeV to ~ 90 GeV will be explored efficiently.

Bibliography

- [1] *A First Course in General Relativity*, Schutz (1985), Cambridge University Press.
- [2] OPAL collaboration, Physics Letters B327 (1994) 397.
- [3] t' Hooft, Nuclear Physics B33 (1971) 173.
- [4] *Quarks and Leptons*, Chapters 13, 14, 15. Haltzen and Martin (1984), Wiley Inc.
- [5] Aitchison, Physics World (July 1989) 'The Unbearable Heaviness of Being'.
- [6] Higgs, Physics Letters 12 (1964) 132.
- [7] Van der Bij and Veltman, Nuclear Physics B231 (1984) 205.
- [8] Lee, Quigg and Thacker, Physics Review Letters 38 (1977) 883.
- [9] *Z Physics at LEP1: Volume 2*, Compiled by Altarelli and Verzegnassi (1989), CERN/PPE 89-08.
- [10] Coleman and Weinberg, Physics Review 73 (1973) 1888.
- [11] CDF collaboration, Fermilab publication 097-E (1994).
- [12] Ph.D Thesis, ^{E.}Gross (1990), Weizmann Institute of Science, Israel.
- [13] Lindener, Sher and Zaglauer, Fermilab publication 206-T (1988).
- [14] Beltrami et al, Nuclear Physics A451 (1986) 679.
- [15] Adler, Dashen and Trieman, Physics Review D10 (1974) 3728.
- [16] CUSB collaboration, Physics Review D26 (1982) 717.
- [17] Crystal Ball collaboration, Physics Letters 48 (1982) 903.
- [18] SINDRUM collaboration, Physics Review 89 (1989) 2.
- [19] ALEPH collaboration, Physics Letters B245 (1990) 289.
- [20] OPAL collaboration, Physics Letters B251 (1990) 211.
- [21] ALEPH collaboration, Physics Letters B236 (1990) 233.
- [22] OPAL collaboration, Physics Letters B268 (1991) 122.

- [23] ALEPH collaboration, Physics Letters B246 (1990) 306.
- [24] DELPHI collaboration, Nuclear Physics B342 (1990) 1.
- [25] L3 collaboration, Physics Letters B252 (1990) 518.
- [26] OPAL collaboration, Physics Letters B253 (1991) 511.
- [27] ALEPH collaboration, Physics Letters B313 (1993) 299.
- [28] L3 collaboration, Physics Letters B283 (1992) 454.
- [29] DELPHI collaboration, Nuclear Physics B373 (1992) 3.
- [30] Large Electron-Positron Storage Ring Technical Notebook, CERN publication (Nov 1989).
- [31] *Detectors for Particle Radiation*, Kleinknecht (1986), Cambridge University Press.
- [32] OPAL collaboration, Nuclear Instruments and Methods A305 (1990) 275.
- [33] *Compact drift-chambers for the OPAL Forward detectors*, Anderson et al (1989), University College HEP Group Library.
- [34] Schaile et al, Nuclear Instruments and Methods A242 (1986) 247.
- [35] Dr. B. Struck. D-2000 Tangstedt/Hamburg.
- [36] MPhil Report, Ametewee (1993), University College London.
- [37] Bjorken, SLAC Report 198 (1977).
- [38] Berends and Kleiss, Nuclear Physics B260 (1984) 32.
- [39] Nicosini and Trentadue, Physics Letters B196 (1987) 551.
- [40] *Production and Decay of the Standard Model Higgs boson at LEP*, Gross et al (1994), Weizmann Institute of Science, Israel.
- [41] Gross et al, OPAL Physics Note 0012 (1988).
- [42] Sjöstrand and Bengtsson, Nuclear Physics B289 (1987) 810.
- [43] Allison, CERN-PPE/91-234 (1991).
- [44] Hilgart et al, CERN-PPE/92-115 (1992).
- [45] Brun et al, CERN DD/EE/84-1 (1987).

- [46] OPAL/ROPE408; Weisz et al (1994).
- [47] Marchesini and Webber, Nuclear Physics B238 (1984) 1.
- [48] The OPAL Primer, Lloyd (1994).
- [49] Charlton, OPAL Technical Note 012 (1991).
- [50] Del Pozo, OPAL Technical Note 170 (1992).
- [51] Kowalewski, OPAL Technical Note 181 (1993).
- [52] DELPHI collaboration, CERN-PPE/94-46 (1994).
- [53] Ph.D Thesis, Nguyen (1992), University of Chicago.
- [54] Duchovni, Igo-Kemenes, Sherwood, Wlodek, OPAL Technical Note to be published soon.
- [55] 1992 Drift-Chamber data quality plots presented by Bruce Kennedy at a UCL OPAL meeting in November 1992.
- [56] Review of Particle Properties, Physics Review D50 1173 (1994).
- [57] *Quantum Field Theory*, Pages 247 248, Mandl and Shaw (1984), Wiley Inc.
- [58] Sjöstrand and Bengtsson, Computer Physics Commun. 43 (1987) 367.
- [59] Böhm, Denner, Hollik and Sommer, Physics Letters 144B (1984) 414.